

12

Effect of Microstructure on 7XXX Aluminum Alloy Fatigue Crack Growth Behavior Down to Near-Threshold Rates

104112.21

P.E. Bretz
A.K. Vasudevan
R.J. Bucci
R.C. Malcolm
Aluminum Company of America



Final Report
79 July 1 to 81 June 30
Contract N00019-79-C-0258
Department of the Navy
Naval Air Systems Command
Washington, D.C. 20360

Approved for public release
Distribution unlimited

1981 October 30

DTIC FILE COPY

DTIC
ELECT
MAR 31 1982

UNCLASSIFIED

SECURITY CLASSIFICATION OF THIS PAGE (When Data Entered)

REPORT DOCUMENTATION PAGE		READ INSTRUCTIONS BEFORE COMPLETING FORM
1. REPORT NUMBER	2. GOVT ACCESSION NO.	3. RECIPIENT'S CATALOG NUMBER
	AD-A112721	
4. TITLE (and Subtitle) Effect of Microstructure on 7XXX Aluminum Alloy Fatigue Crack Growth Behavior Down to Near-Threshold Rates		5. TYPE OF REPORT & PERIOD COVERED Final 79 July 1 to 81 June 30
		6. PERFORMING ORG. REPORT NUMBER
7. AUTHOR(s) P. E. Bretz, A. K. Vasudevan, R. J. Bucci, R. C. Malcolm		8. CONTRACT OR GRANT NUMBER(s) N00019-79-C-0258
9. PERFORMING ORGANIZATION NAME AND ADDRESS Aluminum Company of America Alcoa Laboratories Alcoa Center, PA 15069		10. PROGRAM ELEMENT, PROJECT, TASK AREA & WORK UNIT NUMBERS
11. CONTROLLING OFFICE NAME AND ADDRESS Department of the Navy Naval Air Systems Command Washington, DC 20361		12. REPORT DATE 1981 October 9
		13. NUMBER OF PAGES
14. MONITORING AGENCY NAME & ADDRESS (if different from Controlling Office)		15. SECURITY CLASS. (of this report) Unclassified
		15a. DECLASSIFICATION/DOWNGRADING SCHEDULE
16. DISTRIBUTION STATEMENT (of this Report) Approved for public release Distribution unlimited		
17. DISTRIBUTION STATEMENT (of the abstract entered in Block 20, if different from Report)		
18. SUPPLEMENTARY NOTES		
19. KEY WORDS (Continue on reverse side if necessary and identify by block number)		
Metal Fatigue	Fracture Mechanics	Retardation
Crack Propagation	Aluminum Alloy	High Strength
Threshold	7XXX	Constant Amplitude
Fractography	Microstructure	Variable Amplitude
Stress Intensity	Heat Treatment	Spectrum Loading
20. ABSTRACT (Continue on reverse side if necessary and identify by block number)		
<p>This investigation was undertaken to clarify the role of microstructure on steady state (constant load amplitude) and transient (single periodic overload) fatigue crack growth behavior in 7XXX aluminum alloys at low stress intensity factor ranges (AK). These results were consolidated with data in the literature to obtain an understanding of microstructural effects on crack growth response over a broad AK range.</p> <p style="text-align: center;">DELTA IS</p>		

DD FORM 1 JAN 73 1473

EDITION OF 1 NOV 65 IS OBSOLETE.

UNCLASSIFIED

SECURITY CLASSIFICATION OF THIS PAGE (When Data Entered)

UNCLASSIFIED

SECURITY CLASSIFICATION OF THIS PAGE(When Data Entered)

DELTA K

→ Constant load amplitude data show that there are significant differences in near-threshold FCG resistance among 7XXX alloys. Overaging to a T7 temper reduces low ΔK FCG resistance greatly, whereas intermediate and high ΔK FCG resistance is increased by overaging. In the presence of moisture at intermediate ΔK levels, increasing Cu content from 1.0 to 2.3% increases crack growth resistance. However, there is no consistent effect of Cu content on near-threshold fatigue performance. Similarly, no clear influence of dispersoid type (Cr vs. Zr) on low ΔK FCG resistance was detected. Increasing alloy purity (lowering Fe, Si content) enhances crack growth resistance at high ΔK , but has no effect at near-threshold stress intensities.

DELTA K

The influence of temper and purity on fatigue behavior under a single periodic overload spectrum at low ΔK was examined. FCG resistance for alloys in the T6 temper was significantly greater than for overaged alloys, while increasing alloy purity decreased crack growth resistance. These results, in combination with other information in the literature, are discussed in the context of a two-stage model for spectrum fatigue performance. This model separately considers the load history/microstructure interactions which control both crack retardation and crack growth behaviors. A series of general statements are made regarding specific microstructural characteristics which enhance FCG resistance for various types of load spectra.

← The importance of near-threshold FCG performance to alloy design and materials selection for fatigue resistance is discussed. Potential tradeoffs between design philosophies which emphasize damage tolerance characteristics vs. those which focus on improved life cycle economics are examined. ←

UNCLASSIFIED

SECURITY CLASSIFICATION OF THIS PAGE(When Data Entered)

FOREWORD

This final technical report covers activities performed during the period 1979 July 1 to 1981 June 30 for the Naval Air Systems Command under Navy Contract N00019-79-C-0258. This report is published for information only and does not necessarily represent the recommendations, conclusions, or approval of the Navy.

The contract is with Alcoa Laboratories, Aluminum Company of America, Alcoa Center, Pennsylvania. Mr. M. D. Valentine is the Navy contract monitor. This report has been prepared by R. J. Bucci, Alcoa Project Manager, P. E. Bretz, A. K. Vasudevan, and R. C. Malcolm, Alcoa principal engineer/scientists for the program.



Accession For	
NTIS GRA&I	<input checked="checked" type="checkbox"/>
DTIC TAB	<input type="checkbox"/>
Unannounced	<input type="checkbox"/>
Justification	
By _____	
Distribution/	
Availability Codes	
Dist	Avail and/or Special
A	

TABLE OF CONTENTS

	<u>Page No.</u>
DD Form 1473	i
FOREWORD	iii
LIST OF TABLES	v
LIST OF FIGURES	vi-viii
I. INTRODUCTION	1
II. OBJECTIVES	3
III. PROGRAM PLAN	
3.1 Materials	3-6
3.2 Constant Load-Amplitude FCG Tests - Phase 1	6-7
3.3 Simple Overload Tests - Phase 2	7-8
3.4 Fractographic Examination	8
IV. RESULTS AND DISCUSSION - PHASE 1	
4.1 Constant Load-Amplitude FCG Tests	8-11
4.2 Fractography	11-16
4.3 Discussion of Phase 1 Results	16-20
4.4 Summary of Phase 1 Results	21-23
V. RESULTS AND DISCUSSION - PHASE 2	
5.1 Simple Overload FCG Tests	23-30
5.2 Fractography	30-33
5.3 Discussion of Phase 2 Results	33-37
5.4 Summary of Phase 2 Results	37-41
VI. CONCLUDING REMARKS AND RECOMMENDED FUTURE WORK.	41-43
REFERENCES	44-46

LIST OF TABLES

<u>Table No.</u>		<u>Page No.</u>
1.	Remelt Chemical Analyses of Lab Fabricated Alloys	47
2.	Heat Treatments	48
3.	Constituent and Dispersoid Phases Identified by Guinier-deWolff X-Ray Diffraction	49
4.	Longitudinal Mechanical Properties of 6.35 mm (0.25 in.) Thickness 7XXX Aluminum Plate	50
5.	Calculated Volume % of Constituents and Dispersoids	51
6.	Effect of Microstructural Variants on Constant Amplitude FCG Resistance of 7075 and 7050-Type High Strength Aluminum Alloys Tested in the Presence of Moisture at $R = 1/3$	52
7.	Comparison of Experimental and Predicted FCG Lives for an OLR = 1.8, OCR = 1:8000 Simple Overload Spectrum from an Initial Crack Length of 8.9 mm	53
8.	Comparison of Experimental and Predicted FCG lives for an OLR = 1.8, OCR = 1:8000 Simple Overload Spectrum from an Initial Crack Length of 12.7 mm	54
9.	Influence of Microstructural Variables on Simple Overload Spectrum FCG in 7XXX Aluminum Alloys	55

LIST OF FIGURES

<u>Figure No.</u>	<u>Page No.</u>
1. Relationship of Incremental Crack Advance Per Cycle to Size of Microstructural Features and Estimated Plastic Zone Size Ahead of Crack Tip in Subject Laboratory Fabricated 7XXX Aluminum Alloys	56
2. Description of Periodic Single Spike Overload Tests	57
3. Cyclic Stress Intensity Range, ΔK , Versus Cyclic Fatigue Crack Growth Rate, $\Delta a/\Delta N$, of 7075-T7 Plate (6.35 mm thick)	58
4. Cyclic Stress Intensity Range, ΔK , Versus Cyclic Fatigue Crack Growth Rate, $\Delta a/\Delta N$, of 7475-T7 Plate (6.35 mm thick)	59
5. Cyclic Stress Intensity Range, ΔK , Versus Cyclic Fatigue Crack Growth Rate, $\Delta a/\Delta N$, of 7075 (High Cu)-T7 Plate (6.35 mm thick).	60
6. Cyclic Stress Intensity Range, ΔK , Versus Cyclic Fatigue Crack Growth Rate, $\Delta a/\Delta N$, of 7475 (High Cu)-T7 Plate (6.35 mm thick).	61
7. Cyclic Stress Intensity Range, ΔK , Versus Cyclic Fatigue Crack Growth Rate, $\Delta a/\Delta N$, of 7010-T7 Plate (6.35 mm thick).	62
8. Cyclic Stress Intensity Range, ΔK , Versus Cyclic Fatigue Crack Growth Rate, $\Delta a/\Delta N$, of 7010 (High Purity)-T7 Plate (6.35 mm thick).	63
9. Cyclic Stress Intensity Range, ΔK , Versus Cyclic Fatigue Crack Growth Rate, $\Delta a/\Delta N$, of 7050 (Low Purity)-T7 Plate (6.35 mm thick).	64
10. Cyclic Stress Intensity Range, ΔK , Versus Cyclic Fatigue Crack Growth Rate, $\Delta a/\Delta N$, of 7050-T7 Plate (6.35 mm thick).	65
11. Cyclic Stress Intensity Range, ΔK , Versus Cyclic Fatigue Crack Growth Rate, $\Delta a/\Delta N$, of 7075-T6 Plate (6.35 mm thick).	66
12. Cyclic Stress Intensity Range, ΔK , Versus Cyclic Fatigue Crack Growth Rate, $\Delta a/\Delta N$, of 7050-T6 Plate (6.35 mm thick).	67
13. Effect of Temper on Constant-Amplitude Fatigue Crack Growth Resistance of Aluminum Alloys 7050 and 7075 in High Humidity (> 90% R.H.) Air at Room Temperature at an R-Ratio of 0.33. . .	68
14. Effect of Purity on Constant-Amplitude Fatigue Crack Growth Resistance of 7XXX-T7 Aluminum Alloys in High Humidity (> 90% R.H.) Air at Room Temperature at an R-Ratio of 0.33. . .	69

LIST OF FIGURES (continued)

<u>Figure No.</u>		<u>Page No.</u>
15.	Effect of Copper Content on Constant-Amplitude Fatigue Crack Growth Resistance of 7XXX-T7 Aluminum Alloys in High Humidity (> 90% R.H.) Air at Room Temperature at an R-Ratio of 0.33. . .	70
16.	Effect of Chromium (Cr) and Zirconium (Zr) Dispersoids on Constant-Amplitude Fatigue Crack Growth of 7XXX-T7 Aluminum Alloys in High Humidity (> 90% R.H.) Air at Room Temperature at an R-Ratio of 0.33	71
17.	Typical Fracture Surface Appearance of Alloys 7075-T6 and 7075-T7 at $\Delta K = 2.2 \text{ MPa}\sqrt{\text{m}}$ (2 ksi $\sqrt{\text{in.}}$)	72
18.	Typical Fracture Surface Appearance of Alloy 7075-T7 at a Growth Rate of $3.5 \times 10^{-10} \text{ m/cycle}$ ($1.4 \times 10^{-8} \text{ in/cycle}$). . . .	73
19.	Typical Fracture Surface Appearance of Alloys 7075-T6 and 7075-T7 at $\Delta K = 3.3 \text{ MPa}\sqrt{\text{m}}$ (3 ksi $\sqrt{\text{in.}}$)	74
20.	Typical Fracture Surface Appearance of Alloys 7075-T6 and 7075-T7 at $\Delta K = 5.5 \text{ MPa}\sqrt{\text{m}}$ (5 ksi $\sqrt{\text{in.}}$)	75
21.	Typical Fracture Surface Appearance of Alloys 7075-T6 and 7075-T7 at $\Delta K = 6.6 \text{ MPa}\sqrt{\text{m}}$ (6 ksi $\sqrt{\text{in.}}$)	76
22.	Typical Fracture Surface Appearance of Alloys 7075-T6 and 7075-T7 at $\Delta K = 11 \text{ MPa}\sqrt{\text{m}}$ (10 ksi $\sqrt{\text{in.}}$)	77
23.	Typical Fracture Surface Appearance of High Cu 7075-T7 Alloy at $\Delta K = 2.2$ and $3.3 \text{ MPa}\sqrt{\text{m}}$ (2 and 3 ksi $\sqrt{\text{in.}}$)	78
24.	Typical Fracture Surface Appearance of Alloy 7475-T7 at $\Delta K = 2.2$ and $11 \text{ MPa}\sqrt{\text{m}}$ (2 and 10 ksi $\sqrt{\text{in.}}$).	79
25.	Typical Fracture Surface Appearance of Alloys 7050-T7 and Low Purity 7050-T7 at $\Delta K = 2.2 \text{ MPa}\sqrt{\text{m}}$ (2 ksi $\sqrt{\text{in.}}$).	80
26.	Typical Fracture Surface Appearance of Alloys 7050-T7 and Low Purity 7050-T7 at $\Delta K = 5.5 \text{ MPa}\sqrt{\text{m}}$ (5 ksi $\sqrt{\text{in.}}$).	81
27.	Typical Fracture Surface Appearance of Alloys 7050-T7 and Low Purity 7050-T7 at $\Delta K = 11 \text{ MPa}\sqrt{\text{m}}$ (10 ksi $\sqrt{\text{in.}}$).	82
28.	Typical Fracture Surface Appearance of Low Purity 7010-T7 Alloy at $\Delta K = 2.2$ and $11 \text{ MPa}\sqrt{\text{m}}$ (2 and 10 ksi $\sqrt{\text{in.}}$)	83

LIST OF FIGURES (continued)

<u>Figure No.</u>		<u>Page No.</u>
29.	Crack Length Versus Number of Cycles for Four 7XXX Aluminum Alloys, Using an OLR = 1.8, OCR = 1:8000 Simple Overload Spectrum	84
30.	Comparison of Predicted and Experimental FCG Lives for an OLR = 1.8, OCR = 1:8000 Simple Overload Spectrum	85
31.	Cyclic Stress Intensity Range, ΔK , Versus Cyclic Fatigue Crack Growth Rate, $\Delta a/\Delta N$, of 7075-T6 Plate for an OLR = 1.8, OCR = 1:8000 Overload Spectrum.	86
32.	Cyclic Stress Intensity Range, ΔK , Versus Cyclic Fatigue Crack Growth Rate, $\Delta a/\Delta N$, of 7075-T7 Plate for an OLR = 1.8, OCR = 1:8000 Overload Spectrum	87
33.	Cyclic Stress Intensity Range, ΔK , Versus Cyclic Fatigue Crack Growth Rate, $\Delta a/\Delta N$, of 7050-T6 Plate for an OLR = 1.8, OCR = 1:8000 Overload Spectrum.	88
34.	Cyclic Stress Intensity Range, ΔK , Versus Cyclic Fatigue Crack Growth Rate, $\Delta a/\Delta N$, of 7050-T7 Plate for an OLR = 1.8, OCR = 1:8000 Overload Spectrum.	89
35.	Retardation Ratio, RR, Versus Cyclic Stress Intensity Factor, ΔK , for Four 7XXX Aluminum Alloys.	90
36.	Fracture Surface Appearance of 7050-T7 in the Transition Region from CA to a Simple OL Spectrum.	91
37.	Fracture Surface Appearance of 7075-T7 in the Transition Region from CA to a Simple OL Spectrum.	92
38.	Variation in Simple OL Fracture Surface Lineage Spacing with ΔK in 7075-T6.	93-94
39.	Variation in Simple OL Fracture Surface Lineage Spacing with ΔK in 7050-T7.	95-96
40.	Correlation Between Macroscopic and Microscopic FCG Rates for 7XXX Aluminum Alloys	97-100
41.	Fracture Surface Appearance of 7075-T7 for a Simple OL Spectrum	101
42.	Schematic Diagram Showing the Influence of Metallurgical Variants on Both Retardation and Fatigue Crack Growth During Spectrum Fatigue Loading.	102

I. INTRODUCTION

Slow growing fatigue cracks subjected to very low stress intensity factor ranges (ΔK) comprise a major component of fatigue life in notched structural members. These near-threshold growth rates represent early stages of crack formation and propagation where remedial measures can be instituted. To implement aircraft durability life requirements, fatigue crack growth (FCG) rate information in the low ΔK regime is needed, and yet this is the regime where little aluminum alloy data are available. This shortcoming is attributed to the complexity and expense of near-threshold FCG rate data acquisition.(1)

Test results obtained at intermediate and high FCG rates on aluminum alloys (2-7) show that coarse intermetallic constituent particles, intermediate size dispersoids, and fine precipitates influence crack propagation resistance and fracture toughness. Recent work on Fe-base and Ti-base alloy systems (8-10) suggests that microstructure has a stronger influence on FCG resistance at near-threshold ΔK levels than at moderate to high ΔK values. Should a parallel observation apply to aluminum alloys, opportunity would exist for significant gains in the economic life of aircraft through improved alloy selection.

Utilization of FCG-resistant materials to obtain an optimum balance between durability and damage tolerance needs requires better understanding of how microstructure influences behavior at all ΔK levels. This understanding includes a knowledge of crack growth mechanisms, which vary with stress intensity range (11, 12). Changing fracture processes reflect competition among various mechanisms, and the dominance of a particular mechanism is dependent on both the magnitude of ΔK (5-7) and alloy microstructure. Since the predominant fracture mechanism is not a unique function of ΔK , potential "crossovers" in

alloy performance ranking may develop as one compares FCG resistance established at various levels of ΔK . The first phase of this program characterizes the effect of 7XXX aluminum alloy microstructure, as influenced by composition and temper, on propagation rates established under constant-amplitude cyclic loading conditions. Behavior at intermediate to low ΔK established in this investigation is compared to known behavior at higher ΔK magnitudes.

Constant load amplitude fatigue behavior can be regarded as the "steady-state" response of a material to cyclic loading. However, cyclic loading in service is seldom constant load amplitude, but rather is comprised of a spectrum of variable-amplitude load excursions. FCG behavior under variable-amplitude loading conditions includes transient response characteristics not addressed in constant amplitude tests. In particular, the ability of a material to retard crack growth following overloads is not characterized by a constant load amplitude test. Thus, the relative rankings of alloy FCG resistance under spectrum loading can be opposite to rankings obtained from constant load amplitude tests.(13, 14)

The second phase of this study evaluates the effect of 7XXX aluminum alloy microstructure on transient FCG response to simple tensile overloads, and is intended to link the understanding of steady state and transient FCG response at relatively low ΔK . This phase complements earlier work (5-7) which evaluated overload-microstructure interaction of 7XXX alloys tested at moderate to high stress intensity factor levels. Since FCG performance depends upon details of the loading history, the clarification of transient alloy response to elements of variable cyclic load histories represents an additional step toward knowing

which alloy, component design or test procedure is optimum for a particular class of application; e.g., fighters as opposed to transport aircraft.

II. OBJECTIVES

The role of high strength aluminum alloy microstructure on steady state and overload-related transient FCG resistance at low applied stress intensity factors is not well established. Consequently, the objectives of this investigation are:

(1) Clarify the role of 7XXX aluminum aircraft alloy microstructure, as influenced by composition and temper, on (a) near-threshold constant load amplitude FCG rates, and (b) crack growth retardation characteristics for single periodic overloads superimposed on low ΔK constant load amplitude cycles.

(2) Consolidate results of this investigation with previous work on identical alloys and tempers (5-7) to clarify the role of microstructure on steady state and transient FCG response over a broad range of applied stress intensity factors.

III. PROGRAM PLAN

3.1 Materials

The alloys chosen for study are laboratory-fabricated variants of 7075 and 7050-type high strength aluminum aircraft alloys. These precipitation hardening alloys contain three types of second-phase particles which influence properties such as strength, toughness, and resistance to FCG at moderate to high ΔK (2-7):

(a) large (~ 1 to $30\ \mu\text{m}$) insoluble constituent particles formed during solidification by the combination of the impurity elements Fe and Si with Al and solute elements; (b) smaller (0.02 to $0.3\ \mu\text{m}$) dispersoid particles formed by solid state precipitation of Cr or Zr at temperatures above about 425°C ; and (c) fine (0.002 to $0.01\ \mu\text{m}$) precipitates containing Zn, Mg, and Cu formed during quenching and aging. Relative to alloy 7075, alloy 7050 contains: (a) a lower volume fraction of $\text{Al}_7\text{Cu}_2\text{Fe}$ and Mg_2Si constituent particles because of restricted Fe and Si contents; (b) a lower volume fraction of dispersoids (Al_3Zr in 7050, $\text{Al}_{12}\text{Mg}_2\text{Cr}$ in 7075); and (c) a different composition and higher volume fraction of η' , Mg (Zn, Cu, Al) precipitate because of the higher Cu content. Figure 1 compares the observed range of crack growth rates for constant-amplitude loading with the size* of microstructural features in these alloys. Growth rate measurements established under Phase I of this program primarily correspond to those where the average crack extension per cycle is assumed to be on the order of precipitate size or less.

Materials selected for study in this investigation are identical to those fabricated to study FCG resistance of 7XXX microstructures at intermediate and high ΔK in a previous Navy contract (5). The alloys (Table 1) have the same Zn and Mg contents with variation in Si, Fe, Cu, Cr, and Zr contents, and were selected to examine the effect on FCG behavior of two levels of Mg_2Si and $\text{Al}_7\text{Cu}_2\text{Fe}$ constituents, $\text{Al}_{12}\text{Mg}_2\text{Cr}$ vs. Al_3Zr dispersoids, and high and low Cu variants of η' precipitate. The Zn content averages near maximum for alloy 7075 and near nominal for alloy 7050, while Mg content is within the allowable range for both

* It would be more metallurgically accurate to use interparticle spacing normalized by particle size (i.e., λ/R) rather than solely particle size for this comparison. In the absence of this information, however, the size of the particles is used as qualitative indicator of the scale of these features.

alloys. The nominal compositions of the eight alloys were selected to approximate bounds of commercial high strength 7XXX aircraft alloys. For descriptive purposes, the alloys are labeled and coded as shown in Table 1. The composition of one of the alloys falls within the limits for the European alloy 7010.

All of the alloys were hot rolled from 15 cm thick laboratory-cast ingots to 6.35 mm (0.25 in.) thickness plate. For the materials aged to a T7-type (overaged) temper, the target yield strength was 455 MPa (66 ksi). This is typical for 7050-T73651 plate up to 51 mm (2 in.) thick. In addition, portions of alloys 7050 and 7075 plate were aged to a T6-type (peak strength) temper. Heat treatment practices for all alloys are shown in Table 2. Subsequent to solution heat-treatment and quenching, and prior to aging, all alloys received a 1.5% permanent stretch in the longitudinal direction (i.e., parallel to the rolling direction) for residual stress relief. Extensive metallurgical examination was conducted to characterize the morphology of grain structure and identify the relative size and distribution of insoluble particles in the subject alloys. This characterization is reported in Ref. 5 and includes results from complimentary techniques of electron microprobe analysis, Guinier-DeWolff X-ray diffraction, optical metallography, and transmission electron microscopy. Table 3 shows the secondary phases identified and their computed relative amounts.

A summary of mechanical properties for the subject alloys and tempers is shown in Table 4. Unit propagation energy values from Kahn tear tests provide a relative index for alloy fracture toughness (higher index values denote higher toughness) (15). Smooth-specimen fatigue properties and characterization of

constant amplitude and simple overload FCG resistance at intermediate to high ΔK levels for these alloys are contained in Ref. 5.

3.2 Constant Load Amplitude FCG Tests - Phase 1

Constant load amplitude crack growth rate data were obtained using a standard ASTM E647 compact tension (CT) specimen ($B = 6.35$ mm, $W = 63.5$ mm) in the L-T orientation. Testing was performed on 1 kip capacity MTS servo-hydraulic equipment at a stress ratio ($R = K_{min}/K_{max}$) equal to 1/3 and a frequency of 25 Hz. The test environment was high humidity (relative humidity > 90%), room temperature laboratory air; this was provided by bubbling air through a series of beakers containing water, and then into an air tight chamber surrounding the specimen. The R value and environmental conditions are identical to those used in previous FCG tests of the same materials at high ΔK , Ref. 5. The 25 Hz frequency represents about a three-fold increase over that used in previous work, (5) and was selected as the optimum balance between reduction of test time and stable machine control, thereby requiring minimum operator surveillance. The absence of an observed frequency effect in the range 10 to 150 Hz on near-threshold rates in room temperature air for aluminum alloy 2219-T851 (16) suggests that the three-fold difference in applied frequency will cause a negligible difference in FCG rate measurements for each of the subject alloys.

Specimen precracking was conducted by a schedule of stepped load reductions with increasing crack extension. Upon attaining the desired value of da/dN , the precrack phase was terminated and then FCG rate measurements made as ΔK increased with crack extension under fixed amplitude loading. Crack length was measured visually using photo-etched grids applied to both sides of each CT specimen. Test procedures strictly adhered to the proposed ASTM Standard test practice (1)

for measurement of very low growth rates ($da/dN < 10^{-8}$ m/cycle). For the T6 and T7-type tempers of alloys 7075 and 7050, replicate FCG tests were conducted, while all other alloys were subjected to single tests.

3.3 Simple Overload Tests - Phase 2

For this phase of the program, specimens of the four key microstructures (7075-T6 and T7, 7050-T6 and T7) were tested in a loading sequence consisting of a periodic overload spike occurring once every 8000 constant-amplitude cycles (OCR = 1:8000). The magnitude of the overload spike was 1.8 times the maximum peak load of the constant load amplitude cycles (OLR = 1.8). The nomenclature for overload tests is shown in Figure 2. The stress ratio, R, for the constant amplitude cycles was 1/3, and the applied frequency 20 Hz. All testing was conducted in high humidity air (> 90% R.H.). The targeted crack growth rates correspond to about a 1.5 to 2 orders of magnitude decrease over those rates obtained in Ref. 5 under comparable loading conditions (OLR = 1.8, OCR = 1:8000) at a higher baseline ΔK .

Center-crack-tension (CCT) specimens of identical width (102 mm), thickness (6.35 mm), and orientation (L-T) to those of Ref. 5 were used in the overload tests. Precracking was accomplished without load-shedding, using the same load range as that for the constant load amplitude portion of the simple overload spectrum. Programmed loads were provided by an MTS load profiler interfaced with the electrohydraulic test system.

Crack growth in the overload tests was monitored electronically using crack propagation gages, as described in Ref. 5. In addition, crack length was measured visually using grids applied to one side of each CCT specimen. Test data were

in the form of crack length vs. cycles (a vs. N) curves. A description of data analysis procedures and their precision is included in Ref. 5.

3.4 Fractographic Examination

The scanning electron microscope (SEM) was selected as the primary tool for characterization of fracture appearance, with the objective of identifying variations in fracture topography which correspond to observed differences in mechanical behavior of the subject alloys.

IV. RESULTS AND DISCUSSION - PHASE 1

4.1 Constant Load Amplitude FCG Tests

Constant-amplitude FCG rate (da/dN vs. ΔK) data for the eight laboratory-fabricated 7XXX alloy compositions in the T7 temper are shown in Figures 3 to 10. Results for alloys 7075-T6 and 7050-T6 are compared, respectively, to their T7 temper counterparts in Figures 11 and 12. In Figures 3-12, circles represent the data established in the current investigation, and squares represent data established on the identical materials from prior work (5). Where crack growth rates of the current and previous investigation overlap, the agreement is excellent, as shown in Figures 8 through 12. Replicate tests conducted at low ΔK on alloys 7075-T7, 7050-T7, 7075-T6 and 7050-T6 are also in good agreement, as shown in Figures 3, 10, 11 and 12, respectively.

The FCG rate data band for all subject materials, Figure 1, illustrates that the traditional smooth transition with ΔK decrease from the linear (power-law) regime (da/dN > 2×10^{-8} m/cycle) to the near-threshold regime as reported for steel (2, 16, 17), titanium (18), and 2219-T851 aluminum plate (14, 16) alloys

is not typical of the 7XXX-type plate alloys investigated herein. A similar observation is made by Mackay (19) for 2024-T3 and Alclad 7075-T6 aluminum sheet alloys. The indicated shape of the FCG rate relationship for high strength aluminum aircraft alloys suggests that extrapolation to rates below about 10^{-8} m/cycle (4×10^{-7} in/cycle) based solely on data obtained at higher growth rates should be avoided. Extrapolation may lead to nonconservative approximations of low growth rate performance and likely contributes to the variance of threshold ΔK values reported in the literature for high strength aluminum alloys.

The effect of metallurgical variants on FCG resistance covering four decades of growth rate in high humidity room temperature air is summarized in Figures 13 through 16. Data in Figure 13 indicate the ΔK level required to sustain crack growth at a specified rate. Increased FCG resistance is indicated by a higher ΔK required to sustain growth at the prescribed rate. Since stress intensity factor (K) is directly proportional to applied stress, and approximately proportional to the square root of crack size, the indicated improvements in FCG resistance can be directly correlated to increases in load-carrying capability and tolerable flaw size, or to a decrease in cross-sectional area (which correlates to weight saving in a structural member).

The effect of alloy type (7075 vs. 7050) and temper (T6 vs. T7) on FCG resistance is summarized in Figure 13. At ΔK greater than about $5.5 \text{ MPa}\sqrt{\text{m}}$ ($5 \text{ ksi}\sqrt{\text{in.}}$) alloy 7050 performance is superior to that of alloy 7075, and the overaged T7 temper performance is superior to that of the peak strength T6 temper. These observations are consistent with reported (3-7, 20, 21) and unpublished Alcoa constant-amplitude FCG data generated on comparable materials at rates

greater than about 10^{-8} m/cycle (4×10^{-7} in/cycle). At intermediate ΔK , an increase in resistance to degradation of FCG performance by moisture is the major reason cited for advantages of alloy 7050 over alloy 7075 and for overaged T7-type tempers over the peak strength (T6) and underaged tempers (3-7). Higher toughness with an acceptable reduction in strength from that of the T6 temper also improves high ΔK FCG resistance in a T7-type temper (3, 4, 14).

In contrast, at near-threshold growth rates ($< 10^{-9}$ m/cycle) the T6 temper exhibits greater resistance to crack growth than does the T7 temper for both alloys 7075 and 7050. Other near-threshold data from commercially produced 7075-T651 and 7075 -T7351 plate, established in separate investigations at Alcoa and by Kirby and Beevers (11), likewise confirm the superiority of the peak strength temper to overaged tempers at extremely low growth rates. Knott and Pickard (21) investigated the effect of degree of aging on FCG resistance of an experimental Al-Zn-Mg ternary alloy. They found that progressive aging from underaged, to peak aged, to overaged conditions decreased near-threshold FCG resistance; conversely, at moderate to high ΔK levels greater aging time increased FCG resistance.

Figure 14 partitions the performance of these alloys by purity (Fe, Si) level. The effect of alloy purity is assessed by comparing the band which encompasses all FCG data for low purity alloys to the data band for high purity alloys. At high crack growth rates, a modest improvement in FCG resistance with increased purity is evident; this observation agrees with findings in prior work (3-7). However, no effect of purity on FCG resistance at intermediate and low rates is apparent (Figure 14).

A comparison of the response of high (2.2%) Cu alloys to low (1.5%) Cu alloys in Figure 15 shows that increasing Cu content reduced FCG rates modestly in the range of 10^{-7} to 10^{-6} m/cycle. This observation was made previously by Sanders and Staley (6). In contrast, near-threshold FCG performance of these 7XXX-type alloys appears to be insensitive to an increase in Cu content from 1.5% to 2.2%.

The comparison of responses of alloys containing Cr vs. Zr, shown in Figure 16, shows no evidence of a main effect of dispersoid type at any level of growth rate. This is consistent with results of Selines and Pelloux (22), who observed that substituting Zr for Cr in alloy 7075 did not influence FCG rates.

4.2 Fractography

The changing relationship between crack growth rates and the size of microstructural features (Figure 1) suggests that fatigue mechanisms and fracture surface appearances will vary with constant-amplitude FCG rate. In fact, this has been well-documented in 7XXX alloys for crack growth rates exceeding 10^{-9} m/cycle (3). It is observed that, at high FCG rates, fatigue fracture occurs by initiation and growth of voids from the larger second phase particles (primarily constituents). Intermediate growth rate crack extension in Al alloys usually takes place through fatigue striation formation, while crack growth at low FCG rates appears to be a complex crystallographic mechanism. More detailed discussions of these various fatigue fracture mechanisms will follow. To facilitate this discussion, details of the 7075-T6 and T7 test specimen fracture surfaces will be described first. The fracture topography of the remaining alloys will then be examined in the context of observations made on alloy 7075.

7075-Type Alloys

In the present work, the lowest crack growth rates measured are more than an order of magnitude smaller than those reported in Ref. 5 for the same alloys. At these very low FCG rates, concurrent fracture modes are observed on specimens of both alloys 7075-T6 and 7075-T7 - one mechanism which appears flat and featureless, the other having a crystallographic (i.e., faceted) texture. These details are marked as A and B, respectively, in Figures 17(a) and (b). The step-like markings of faceted (crystallographic) regions indicate variation in local crack propagation direction from one faceted region to the next, and have been attributed to slip plane decohesion (12, 23). As will be discussed in the next section, strain localization in the crack tip plastic zone is believed to promote this slip plane fracture mechanism. Unlike faceted growth, however, the nature of non-crystallographic fracture is not well understood. At present, this mechanism is believed to be a manifestation of some environmental interaction with the crack growth process at very slow FCG rates (23, 24).

An additional feature occasionally observed, predominantly at low growth rates, is oxide contamination, denoted as detail C in Figure 17(b). This debris can be a result of either general corrosion or repeated rubbing of the mating fracture surfaces. In addition, a general oxide layer covers the entire surface. Using secondary ion mass spectrometry (SIMS), oxide thickness was measured as a function of crack growth rate for 7075-T6 and T7. A uniform oxide depth of 5-10 nm covers the fracture surface of 7075-T6 at all FCG rates. In contrast, oxide thickness on the fracture surface of 7075-T7 rises to 100 nm as da/dn decreases to near-threshold rates, while a layer only 5-10 nm thick covers the fracture surface for $da/dn > 1 \times 10^{-9}$ m/cycle (4×10^{-8} in/cycle). These oxide layers,

particularly the ten-fold increase in thickness for 7075-T7, indicate some environmental interaction with the FCG process. At this time, however, the nature of this interaction is not known.

Stereographic observation was performed to establish other subtle differences in topography which may exist on fracture surfaces of constant-amplitude FCG specimens. In particular, the low ΔK fracture surface of 7075-T6 seems to be rougher than that of 7075-T7. Figures 17(a) and 18 compare, respectively, the fracture appearance of 7075-T6 and 7075-T7 at the same near-threshold growth rate of 3.5×10^{-10} m/cycle (1.4×10^{-8} in/cycle). The flat appearance of the overaged T7 fracture surface is in marked contrast to the rougher topography of the peak aged specimens; this difference was confirmed by stereofractography for both alloys 7075 and 7050. The flatter T7 fracture surface was generated at $\Delta K = 1.9 \text{ MPa}\sqrt{\text{m}}$ ($1.7 \text{ ksi}\sqrt{\text{in.}}$) while the rougher T6 topography was produced at $\Delta K = 2.2 \text{ MPa}\sqrt{\text{m}}$ ($2 \text{ ksi}\sqrt{\text{in.}}$). This suggests that the flat fracture topography represents a lower-energy fracture mechanism than the rougher crystallographic fracture.

At ΔK of $3.3 \text{ MPa}\sqrt{\text{m}}$ the fracture surfaces of both 7075 tempers (T6 and T7) are predominantly faceted in nature (Figure 19). Figures 17 and 19 show little evidence of large constituent particles and isolated occurrences of smaller particles on the low ΔK fracture surfaces. In contrast, the fracture topography at intermediate ΔK values of 5.5 and $6.6 \text{ MPa}\sqrt{\text{m}}$, Figures 20 and 21 respectively, shows some evidence of local fracture around large second phase particles (denoted as detail P) in addition to predominantly faceted growth and indications of local secondary cracking (detail SC). At $\Delta K = 11 \text{ MPa}\sqrt{\text{m}}$ the fracture mode

is completely dimpled rupture, with many of the voids having been nucleated by second phase particles, as shown in Figure 22. Limited fractography at higher magnification (10,000 X) reveals traditional fatigue striations at ΔK levels greater than about $4 \text{ MPa}\sqrt{\text{m}}$. It is expected that more closely spaced striations would be present at lower ΔK had these fractures been studied at greater magnifications.

Examination of SEM fractographs ($\sim 200 \text{ X}$) of Figures 17 through 22 shows little difference between the topography of 7075-T6 and T7 specimens at comparable ΔK values, other than the difference in fracture surface roughness at low ΔK . This is consistent with the observation that variations in crack growth rates are generally modest at intermediate and high ΔK . The difference in fracture surface roughness at low ΔK is not great, considering the large variation in FCG performance with temper. Unfortunately, at near-threshold ΔK levels, cyclic deformation and fracture processes occur within such small zones that it is doubtful whether other variations in topography with temper could be resolved at the indicated magnifications.

There appears to be a subtle influence of Cu content on the fracture topography of alloy 7075-T7, primarily at low ΔK , even though an effect of Cu content on FCG performance is not noticeable at low growth rates. A comparison between the fractograph in Figure 23(a) and those in Figure 17(a) and (b) indicates that the high Cu 7075-T7 fracture surface at ΔK of $2.2 \text{ MPa}\sqrt{\text{m}}$ contains relatively more flat (non-crystallographic) areas than does the base alloy. The fracture appearance of the base and high Cu 7075 alloys are similar at ΔK of $3.3 \text{ MPa}\sqrt{\text{m}}$, as shown in Figure 23(b) and Figures 19(a) and (b), and at higher ΔK values.

The fracture surface of alloy 7475-T7 at $\Delta K = 2.2 \text{ MPa}\sqrt{\text{m}}$, Figure 24(a), shows a mixture of faceted and flat fracture modes as does its lower purity counterpart alloy 7075-T7 shown in Figure 17(b). The somewhat lower FCG resistance of alloy 7475-T7 relative to that of alloy 7075-T7 at moderately low rates is consistent with the higher percentage of flat fracture in alloy 7475 at ΔK of $2.2 \text{ MPa}\sqrt{\text{m}}$. Whether this characteristic can be attributed to purity differences between alloy 7075 and 7475 remains ambiguous, as little influence of constituent particles on fracture appearance is detectable at low ΔK . Although fracture associated with second phase particles in alloy 7475 also becomes more apparent with increasing ΔK , the development and coalescence of voids is less noticeable, Figure 24(b), than in alloy 7075-T7, Figure 22(b); this corresponds to the greater constituent volume fraction of the base alloy. The suppression of void coalescence with increasing purity results in superior FCG resistance, predominantly at high ΔK approaching the material toughness. At moderate ΔK little or no effect of purity on FCG performance is evident. As in alloy 7075, secondary cracking in alloy 7475-T7 is also apparent at ΔK of $11 \text{ MPa}\sqrt{\text{m}}$, and is denoted as detail SC in Figure 24(b).

7075-Type Alloys

The 7050-type alloy compositions contain Zr-bearing dispersoids instead of a Cr-bearing second phase. In general, the fracture topography of 7050-type alloys are similar to those of the 7075-type alloys at comparable ΔK levels. As shown in Figure 25, both the base and low purity variants of alloy 7050-T7 exhibit mixed faceted and flat fracture modes at ΔK of $2.2 \text{ MPa}\sqrt{\text{m}}$. Like alloy 7075-T7, little or no effect of the larger second phase particles on fracture is evident at low ΔK . Progressive ΔK increases to 5.5 and $11 \text{ MPa}\sqrt{\text{m}}$, Figures 26

and 27 respectively, show a rising level of void formation in proportion to the relative constituent amounts of the high and low purity 7050 alloy counterparts. At high ΔK secondary cracking is also noted in both alloys, detail SC in Figure 27.

Low purity alloy 7010-T7, which is similar in composition to alloy 7050-T7 except for a lower Cu content, likewise is characterized by faceted and flat fracture modes at ΔK of $2.2 \text{ MPa}\sqrt{\text{m}}$, and void coalescence with some secondary cracking at ΔK of $11 \text{ MPa}\sqrt{\text{m}}$, Figure 28. Comparison of fractures from 7075-type alloys containing Cr with 7050-type alloys containing Zr suggests that Zr-bearing alloys suppress microvoid coalescence at ΔK of $11 \text{ MPa}\sqrt{\text{m}}$; compare Figures 22 and 24(b) with Figures 27 and 28(b). However, at ΔK of $2.2 \text{ MPa}\sqrt{\text{m}}$ differences in fracture appearance with dispersoid type cannot be detected at the indicated magnifications.

4.3 Discussion of Phase 1 Results

At near-threshold crack growth rates, alloy temper has a much greater effect on FCG resistance in these 7XXX-type alloys than does purity, Cu content, or dispersoid type. As noted in section 4.1, other investigators also have reported that the near-threshold FCG resistance of 7XXX-type alloys in a T6 temper is greater than in the overaged T7 temper. In one case, Knott and Pickard (21) correlated increased near-threshold FCG resistance with higher cyclic flow stress. They observed that a peak-aged 7XXX-type alloy had a greater threshold ΔK and a higher cyclic flow stress than did the overaged T7 temper alloy. Furthermore, these investigators noted an even higher threshold ΔK for the underaged 7XXX alloy, which also has the highest cyclic flow stress of all three temper conditions.

Figure 1 shows that near-threshold FCG rates correspond to an average increment of crack advance per cycle which is appreciably less than the size of the smallest precipitates. Also, at these near-threshold ΔK levels the crack tip plastic zone size can be on the order of subgrain dimensions or less. When crack tip plastic deformation occurs on such a small scale, the accumulation of cyclic damage which precedes crack extension should be particularly sensitive to dislocation motion within individual grains or subgrains.(25) Furthermore, slip processes are influenced more by the fine precipitate microstructure than by the presence of larger, less frequently-encountered second phase particles (constituents and dispersoids). Thus, fine precipitates are expected to have a greater effect on near-threshold behavior than other second phase particles.

The decrease in precipitate/matrix coherency as aging time increases is believed to contribute to the degradation of low ΔK FCG resistance (20, 21). Coherent precipitates will shear as crack tip deformation occurs, constraining dislocation motion to a few slip systems in the crack tip plastic zone. This strain localization creates preferred paths for crack propagation along the few active slip systems where slip damage has occurred. However, because these slip systems may not be perpendicular to the axis of applied tensile loading, the crack is forced to follow a tortuous path through the microstructure, reducing the macroscopically-determined FCG rate. In contrast, dislocations can loop around incoherent precipitates in overaged alloys, so that the crack tip strain distribution is homogeneous and no preferred paths for crack growth are created. In this case, crack extension occurs without significant deviation from a plane normal to the tensile axis, and macroscopic crack growth rates are higher than in underaged material tested at the same ΔK level. Recall from the discussion

of Figure 18 that, indeed, the fracture surface of 7075-T6 at very low FCG rates is rougher than that of 7075-T7 at similar growth rates.

In addition to changes in precipitate/matrix coherency, precipitate size and spacing increase with progressive aging from an underaged, through T6, to a T7 temper condition. Since these second phase particles represent obstacles to crack propagation, an increase in interparticle spacing should reduce FCG resistance, particularly when crack growth rates are on the order of precipitate dimensions (Figure 1). Thus, both precipitate coherency and spacing arguments suggest that near-threshold FCG resistance improves with decreased aging time; therefore, underaged tempers should have optimum FCG performance at low ΔK . Because of the stress corrosion cracking sensitivity of underaged 7XXX-type aluminum alloys, however, such tempers have little commercial viability.

As crack tip plasticity and incremental crack advance per cycle increase with ΔK , improvements in FCG resistance attributed to reduced precipitate spacing and increased coherency would be expected to vanish. This is consistent with 7XXX alloy data at intermediate and high ΔK which show improved FCG resistance in overaged tempers.

The greatest effect of alloy purity on fatigue performance is at high, not low, FCG rates. High purity alloys with a low volume fraction of insoluble Fe and Si constituents have superior toughness in comparison to low purity alloys containing greater amounts of Fe and Si. At high ΔK , voids form at constituent particles ahead of the crack, and then link up with the main crack front by ductile tearing when the crack tip plastic zone is of the order of mean void

spacing (e.g., Figure 22). The modest improvement in high ΔK FCG resistance with increased purity relates to a reduction in constituent volume fraction, and hence, a reduced number of void origins to link up with the main crack. Recall that this was illustrated in Figure 27. This observation agrees with both the calculated volume (%) of particles in these alloys, Table 5, and with findings in prior work (3-7). However, no effect of purity on FCG resistance is evident at intermediate and low growth rates (Figure 14). Previous results (3-7) also have shown that an effect of Fe and Si-bearing constituent particles on FCG resistance is unlikely at intermediate ΔK . Since the plastic zone size is on the order of constituent dimensions at intermediate and low ΔK levels (Figure 1), crack tip deformation is insufficient to cause frequent secondary particle fracture. Figures 20 and 21 do show that constituent fracture and subsequent void growth occur only occasionally at intermediate FCG rates.

The observation that increased Cu content reduces FCG rates modestly at intermediate ΔK (Figure 15) is consistent with studies reported by Truckner, et al (3) and Lin and Starke (23). In both of these investigations, an increase in Cu content from about 1.0 to 2.3% in 7050-type alloys result in progressive improvements in intermediate ΔK FCG resistance in moist environment. Unpublished Alcoa test data indicate that a further increase in Cu content to 3.2% in an Al-Zn-Mg-Cu-Zr alloy (beyond the 2.6% commercial limit for 7050), continues to improve FCG resistance over the da/dN range of 10^{-9} to 10^{-7} m/cycle when moisture is present.

In contrast, near-threshold FCG performance of these 7XXX-type alloys was insensitive to an increase in Cu content from 1.5% to 2.2% (Figure 15). And yet, other studies have shown that FCG performance in 7050-type alloys is degraded by Cu additions. Starke and co-workers (23, 24) have shown that crack growth rates for 7050-T651 and T7351 type alloys containing a broad Cu range (0.01-2.1%), when tested in distilled water, are lowest for the alloys containing 0.01% Cu. Starke and Sanders (24) have suggested that the kinetics of electrochemical reactions at the crack tip change with Cu content in these alloys, causing a degradation in near-threshold FCG performance with increasing Cu content. Apparently, the variation in Cu content examined in the present study (1.5 to 2.2%) was not sufficient to cause a noticeable change in low ΔK FCG response. In any event, it seems that the effect of Cu content on FCG performance at low growth rates is much less significant than the effect of temper.

The substitution of Zr for Cr also does not appear to influence near-threshold FCG rates in these alloys (Figure 16). However, Filler (26) recently has reported that substituting Zr for Cr in a 7XXX series alloy increased ΔK_{th} from 1.7 MPa \sqrt{m} to 2.1 MPa \sqrt{m} for tests in dry argon at $R = 0.05$. Filler rationalized this observation by noting that Al_3Zr is coherent with the matrix, while $Al_{12}Mg_2Cr$ is incoherent. Since the present work was performed in high humidity air at $R = 0.33$, a comparison between these results and those of Filler is not straightforward. The effect of dispersoid type on FCG resistance requires further investigation.

4.4 Summary of Phase 1 Results

The work presented to this point characterizes the role of 7XXX aluminum alloy microstructure (viz. temper, purity, Cu content and dispersoid type) on constant load amplitude FCG resistance at low to intermediate ΔK in high humidity (> 90% R.H.) room temperature air. Test results have been consolidated with those previously obtained on identical alloys at intermediate and high ΔK to provide a more thorough characterization over a wide range of growth rates. Based on these data and review of relevant literature (3, 11, 21, 23, 24, 26), several conclusions are appropriate for 7075 and 7050-type aluminum aircraft alloys. These conclusions are enumerated below and summarized in Table 6.

(1) Differences in FCG resistance among these aluminum alloys are greatest at near-threshold crack growth rates, which have the greatest impact on fatigue life. This is consistent with observations that the interaction between an extending fatigue crack and a microstructural feature is greatest when characteristic dimensions of the latter are of the same order or greater than the average increment of crack advance per cycle.

(2) For near-threshold FCG behavior established in the presence of moisture, there are two major (and perhaps competing) crack growth mechanisms. One is a predominantly microstructure-dependent process (crystallographic fracture), while the other, characterized by a flat featureless appearance, appears to be dependent upon the interaction of microstructure with environment.

(3) Alloy temper has a major effect on near-threshold fatigue performance, where increased aging time reduces FCG resistance. This change in low ΔK behavior is believed to be linked to changes in cyclic slip processes with increased aging, which occur as a result of (a) increased precipitate spacing, and (b) decreased precipitate/matrix coherency. Also, increased aging may alter environmental interactions at the crack tip for these high humidity tests, further contributing to a change in near-threshold FCG resistance.

(4) At intermediate and high ΔK levels where the ratio of crack tip plasticity to subgrain size becomes large, changes in the slip process within subgrains are less important in influencing FCG performance. Overaging beyond peak strength increases FCG resistance, primarily by reducing the acceleration of crack growth by environmental interactions (intermediate ΔK) and by increasing alloy toughness (high ΔK). For growth rates greater than 2.5×10^{-9} m/cycle (1×10^{-7} in/cycle), overaged T7 temper alloys have greater FCG resistance than T6 temper alloys, which is in direct contrast to the ranking observed at near-threshold rates.

(5) In a moist air environment, FCG resistance at intermediate and high ΔK increases with Cu content. In contrast, the present results do not suggest an influence of Cu content (1.5 to 2.2%) on near-threshold FCG resistance. Since, however, other studies (23, 24) have reported a decrease in near-threshold FCG resistance with increasing Cu content over a greater range (0.01 to 2.1%), further work is necessary to confirm the effect of Cu content on FCG performance at low ΔK .

(6) Purity (Fe, Si content) has little or no main effect on constant amplitude FCG resistance at low and intermediate growth rates within the composition range studied. Rather, this effect of alloy purity is most pronounced when the maximum cyclic stress intensity approaches the material toughness.

(7) Dispersoid type (Cr vs. Zr) did not appear to influence near-threshold FCG rates when these alloys were tested in high humidity air. Other data (26) in the literature, however, have indicated that ΔK_{th} in 7XXX-type alloys is increased when Zr is substituted for Cr for tests in argon. Therefore, additional study is required.

V. RESULTS AND DISCUSSION - PHASE 2

5.1 Simple Overload FCG Tests

The four principal microstructural variants (7075-T6 and T7, 7050-T6 and T7) were examined in this phase of the contract to evaluate overload-induced transient FCG performance of 7XXX aluminum alloys at low crack growth rates. Test results are presented in Figure 29 in the form of total crack length vs. total number of cycles (constant-amplitude plus simple overload) for each alloy and temper. Data for both alloys in the T7 temper represent the average response of duplicate tests, while the data for each alloy in the T6 temper represent the results of single tests.

Two observations are apparent when examining the data in Figure 29. Most striking is the three-fold increase in life for the T6 over the T7 temper for both 7075 and 7050. Less dramatic, but also significant, is the longer life

of 7075 vs. 7050 for equivalent tempers, an increase of approximately 50%. The superior FCG resistance of both alloys in the T6 temper over the T7 temper for an overload (OL) history of $OLR = 1.8$, $OCR = 1:8000$ (see Figure 2) is consistent with constant load amplitude (CA) data for these alloys at near-threshold rates below about 1×10^{-9} m/cycle (4×10^{-8} in/cycle), Figures 11 and 12. Since near-threshold rates are slower for the T6 temper than for T7, longer fatigue lives would be expected for the T6 condition if a significant fraction of the total cyclic life is spent at these very slow crack growth rates. It appears that overload-induced retardation suppressed the effective ΔK , and hence FCG response, into the near-threshold regime where the T6 temper is advantageous over T7.

The superior FCG performance at low growth rates of the T6 temper over T7 is not consistent with alloy rankings, either CA or OL, previously reported for these same materials tested at higher growth rates (5, 7). In these earlier studies, the T7 temper of both alloys had longer FCG lives than T6 for both CA and $OLR = 1.8$, $OCR = 1:8000$ (OL) histories. However, the OL tests described in Refs. 5 and 7 were conducted at applied load levels about 1.9 times greater than those for the present tests. The minimum ΔK for CA testing reported previously was about $6.6 \text{ MPa}\sqrt{\text{m}}$ ($6 \text{ ksi}\sqrt{\text{in.}}$) as compared to about $2.2 \text{ MPa}\sqrt{\text{m}}$ ($2 \text{ ksi}\sqrt{\text{in.}}$) from Phase 1 of the present work. From Figures 11 and 12, it is clear that $\Delta K = 6.6 \text{ MPa}\sqrt{\text{m}}$ is well above the crossover point and into the region where the T7 temper has superior FCG resistance for both 7075 and 7050. This observation implies that the CA and OL FCG test results of this study and of Refs. 5 and 7 are self-consistent. That is, alloy rankings for the $OLR = 1.8$, $OCR = 1:8000$ OL spectrum are identical to those for CA loading at similar

growth rates. However, this may not be true for all OL spectra (e.g., Refs. 5 and 7), particularly when dominant FCG mechanisms change. This point will be clarified in later discussion.

The increase in FCG life for 7075 over 7050 of comparable temper has been noted previously for an identical OLR = 1.8, OCR = 1:8000 OL sequence at higher applied stress levels (5, 7). Conversely, Refs. 5 and 7 show that 7050 exhibits superior FCG resistance in comparison to 7075 at high growth rates when an OLR = 1.4, OCR = 1:4000 spectrum is employed. In this case, FCG lives of these alloys are controlled by intermediate and high ΔK CA behavior for which alloy 7050 is superior. The low ΔK CA data shown in Figure 13 do not suggest that variable load history near-threshold performance of 7075 consistently will be better than that of 7050, regardless of temper. Furthermore, the superior FCG resistance of 7075 over 7050 at low ΔK levels for the OLR = 1.8, OCR = 1:8000 load history does not agree with data in the literature on spectrum FCG, in which 7050 generally is superior to 7075 (13, 27, 28). The referenced studies have used load spectra more complex than a single periodic OL sequence, and often were conducted at significantly higher applied stress than the present work. In one case, the FCG resistance of 7075 was better than 7050 in comparable temper for an aircraft fighter spectrum, while 7050 FCG resistance was superior for CA loading. Thus, it should not be expected that CA and spectrum FCG alloy rankings will be identical, nor will all spectra result in the same performance rankings. This was summarized in a recent paper (7), where ranking of alloy FCG resistance was shown to depend upon two interactive crack growth characteristics: (a) the ability of a given microstructure to resist crack extension under

constant amplitude loading; and (b) the ability of the material to retard FCG following a high tensile load excursion. The relative contributions of these two mechanisms toward determining spectrum FCG resistance will be discussed later.

Analytical Model for FCG Performance

It is not evident from Figure 29 to what extent crack growth was retarded in alloys 7075 and 7050 as a result of the simple OL sequence. To examine this question, a modified version of the computer program EFFGRO was used to separate the linear damage and retardation components of FCG life for the variable load history. The EFFGRO program is based on the Vroman retardation model* (29), and has previously been used to predict experimental lives for these alloys under spectrum loading conditions at higher ΔK levels (5, 7).

For each alloy and temper, the fatigue life of a CCT test specimen was predicted for 3 conditions: (1) the actual OLR = 1.8, OCR = 1.8000 OL spectrum incorporating OL-induced retardation; (2) the identical loading sequence as (1), but assuming no retardation; and (3) the OL history with a constant amplitude sequence consisting solely of the overloads. The second case assumes that crack extension is a linear damage summation of the independent contributions of OL and CA cycles in the spectrum without load interaction effects. Conversely, the third case removes the baseline CA cycles and assumes that crack extension takes

* The Vroman model reflects "state of the art" FCG life prediction methodology, and accounts for retardation through the use of effective stress intensity factor concepts based on crack tip plasticity (e.g., see ASTM STP 687).

place only during the OL cycle in each load block.

Table 7 and Figure 30 show predictions for the growth of a crack from a half-crack length of 8.9 to 27.9 mm (.35 to 1.1 in.) in a 102 mm (4 in.) wide CCT panel. In these predictions, one block represents 8000 CA cycles + 1 OL cycle, as defined in Figure 2. Several observations can be made with regard to the data in Figure 30. The actual experimental lives of these alloys are much longer than predicted by the linear damage assumption (no retardation), with actual FCG lives greater than those predicted by a factor of 5 for 7050-T7 to a factor of 46 for 7075-T6. Clearly, the periodic OL ($OLR = 1.8$, $OCR = 1:8000$) causes a significant retardation of crack growth during baseline CA cycles. In contrast, actual lives of all 4 alloys are orders of magnitude shorter than predicted for FCG during only the OL cycles. This suggests that crack extension occurring during the CA portion of each loading block comprises a significant fraction of total spectrum life.

When retardation was considered, the accuracy of the EFFGRO predictions varied with alloy and temper (see Figure 30). Whereas the predictions for both alloys in the T7 temper were conservative and within 75% of actual lives, the predictions for T6 temper alloys were non-conservative and as much as 700% greater than actual lives. Upon first examination, this inaccuracy seems surprising. As will be discussed in later sections, there are multiple crack growth retardation mechanisms operating during variable amplitude loading. However, one mechanism is expected to dominate spectrum FCG behavior at low stress intensities: overload-induced localized plastic deformation reduces

the effective stress intensity factor (ΔK_{eff}) during subsequent baseline CA cycles. Since this is the retardation mechanism on which EFFGRO is based, it was anticipated that these life predictions would be reasonably accurate. This was not the case for alloys in the T6 temper.

One clue to the inaccuracy of EFFGRO for the T6 temper alloys appears when a detailed examination of the Vroman model calculations is made. The model determines a value of ΔK_{eff} for CA cycles following each overload excursion, and then uses CA FCG data (Figures 11 and 12) to determine a growth rate (and, thus, a crack growth increment) for each cycle. For CA cycles immediately following the first OL, ΔK_{eff} is calculated to be $2.0 \text{ MPa}\sqrt{\text{m}}$ ($1.8 \text{ ksi}\sqrt{\text{in.}}$), whereas the applied stress intensity (ΔK_{app}) is $3.3 \text{ MPa}\sqrt{\text{m}}$. This value for ΔK_{eff} is below the range of near-threshold FCG data for both T6 alloys (Figure 11 and 12), but not outside the measured range for either T7 alloy. Thus, EFFGRO is forced to extrapolate CA FCG data for 7075-T6 and 7050-T6 to make life predictions. The non-conservative life predictions for both alloys in the T6 temper seem to imply that extrapolated growth rates are lower than they actually were. On the other hand, no extrapolation of FCG data was necessary for either T7 temper alloy, so the life estimations are relatively accurate.

To confirm that these inaccuracies are a result of extrapolating FCG data, a second set of life predictions were made, this time using a longer initial half crack length of 12.7 mm (0.5 in.). In this case, the lowest value of ΔK_{eff} calculated by EFFGRO was $2.4 \text{ MPa}\sqrt{\text{m}}$ ($2.2 \text{ ksi}\sqrt{\text{in.}}$), which is within the measured range of FCG data for all 4 alloys (Figures 11 and 12). The results of these life estimations are presented in Table 8 and show that all predictions were

within a factor of 2 of the experimental lives. The improved accuracy of these latter estimations in comparison to those in Table 7 confirms that the extrapolation of CA FCG data is a major contributor to inaccuracy of predicted T6 temper lives starting from the shorter initial crack length.

It has been shown in this section that the growth of a crack subjected to simple overload spectra at low stress intensities can be reasonably simulated by using a plasticity-based retardation model like EFFGRO. However, accurate low ΔK CA data are critical for predicting crack growth life for load spectra in which appreciable retardation is involved (i.e., ΔK_{eff} is very low). For this reason, factors which affect near-threshold FCG behavior (e.g., precracking test procedures, environmental influences, short crack effects, etc.) must be better understood if these life prediction tools are to be used accurately.

Crack Growth Retardation

While the data in Figure 30 indicate the degree to which FCG lives in 7XXX alloys were increased by an OLR = 1.8, OCR = 1:8000 OL spectrum, the actual retardation of crack growth rates relative to CA loading cannot be ascertained from this information. To do so, we must compare da/dN from CA and OL tests for equivalent loading conditions. For each OL test this is accomplished by calculating ΔK corresponding to the baseline CA cycles in the OL spectrum (Figure 2). Figures 31-34 present CA and OL crack growth rate data vs. baseline ΔK for each alloy and temper. From these figures, it is clear that the periodic 1.8 P_{max} OL has caused substantial retardation of crack growth rates in subsequent baseline CA cycles.

The data in Figures 31-34 also suggest that the degree of retardation is not the same for all aluminum alloys and tempers. The amount of retardation can be measured conveniently by using a retardation ratio, RR, which is defined as the ratio of CA da/dN to OL da/dN at equivalent base ΔK levels. Thus, a larger RR indicates greater retardation at comparable applied ΔK . Values of RR at several ΔK levels are presented in Figure 35; they show that the T6 temper alloys exhibit greater retardation than T7, while alloy 7075 has greater retardation capability than 7050 for equivalent temper. It is important to note, though, that high values of RR do not guarantee superior spectrum FCG resistance if, for example, CA FCG performance is extremely poor.

5.2 Fractography

All OL crack growth experiments were conducted by first precracking each CCT specimen under constant amplitude loading using the same load range as for baseline CA cycles of the spectrum. After a well-established fatigue crack was developed, the periodic overload spectrum was applied. The application of this OLR = 1.8, OCR = 1:8000 spectrum caused an immediate and dramatic change in fracture surface topography, as shown in Figures 36 and 37 for 7050-T7 and 7075-T7, respectively. The texture of the CA fracture surfaces in these figures is crystallographic, much like that noted previously for low ΔK constant-amplitude loading (see Figure 19). This is to be expected, since the stress intensity range at the end of CA precracking was approximately $3.3 \text{ MPa}\sqrt{\text{m}}$ ($3 \text{ ksi}\sqrt{\text{in.}}$). However, the distinctly different fracture topography after beginning the OL sequence (Figure 36a and 37a) suggests that crystallographic fracture has been suppressed in favor of some other crack growth mechanism.

This, in turn, suggests that different microstructural features may control crack growth under a simple overload spectrum in comparison to growth under constant amplitude loading. Closer inspection of this initial OL region (Figure 36b) reveals regularly-spaced lines oriented perpendicular to the crack growth direction. Another observation is the presence of fractured second phase particles in the OL region of 7075-T7 (denoted by arrows in Figure 37b) but not in 7050-T7 (Figure 36a). The subject of constituent particle fracture will be discussed later.

Examination of test specimen fatigue surfaces at various crack lengths reveals that these fracture surface lines dominate the topography of both 7075 and 7050 in the T6 and T7 tempers regardless of ΔK levels, and that spacings of these lines increase with ΔK magnitude. For example, Figures 38 and 39 illustrate this fracture mechanism at various ΔK levels for 7075-T6 and 7050-T7, respectively. To confirm the origin of these markings, measurements of line spacings were made at a series of crack lengths (i.e., various ΔK levels) for each alloy and temper. The fact that these measurements are much larger than macroscopic growth rates per cycle for the OL FCG tests confirms that this fracture mechanism is not classical fatigue striation formation. However, when the line spacing measurements are divided by 8001 cycles/block and plotted along with simple OL crack growth rate data (Figure 40a-d), a close correspondence is seen. This confirms that these markings represent the increment of crack advance in each load block. Unfortunately, it is not possible to distinguish the fraction of each block band produced during an OL cycle from that part created by a segment of 8000 CA cycles.

No evidence of classical fatigue striations was found within each block band at any crack length. Indeed, no discernable features within a band could be seen for macroscopic growth rates less than 2.5×10^{-5} m/cycle (1×10^{-7} in/cycle) (see especially Figure 38b). By contrast, the distinctive feathery appearance of crystallographic fatigue fracture was evident where measured OL growth rates exceeded 2.5×10^{-9} m/cycle. This is particularly noticeable in Figures 39c and 39d; however, it is important to point out that this crystallographic fracture has been created at $\Delta K = 8.1 \text{ MPa}\sqrt{\text{m}}$ ($7.4 \text{ ksi}\sqrt{\text{in.}}$). At an equivalent ΔK in CA specimens, crystallographic fracture is already being superseded by void coalescence (Figures 21 and 22). Thus, although crystallographic fatigue fracture is a mechanism common to both CA and OL tests (OLR = 1.8, OCR = 1:8000), it occurs at significantly higher ΔK levels for the OL spectrum than for CA loading.

Another interesting contrast in fracture topographies between CA and OL FCG specimens relates to the appearance of second phase particles on the fracture surfaces. As discussed previously (section 4.2), the presence of second phase particles on CA fracture surfaces is limited to higher ΔK where void coalescence is the dominant fracture mechanism. However, Figures 37b and 38a-d clearly show an abundance of constituent particles on the OLR = 1.8, OCR = 1:8000 OL fractures at applied baseline CA stress intensities for which little or no constituent particle fracture is seen in CA specimens. In fact, most of the constituents appear to be fractured, which certainly must be a result of the periodic OL spikes. This evidence suggests that second phase particles play a different role in the fatigue fracture process during this OLR = 1.8, OCR = 1:8000 OL spectrum than during CA loading.

The density of fractured constituent particles varies among the four alloy/temper combinations. For example, a comparison of Figures 37b and 36a show a greater density of fractured constituent particles on the OL fracture surface of 7075-T7 than 7050-T7. This is not surprising, since 7050 is a higher purity alloy than 7075. Temper also appears to influence constituent particle fracture, since particle density is much higher for 7075-T6 (Figures 38c and d) than for 7075-T7 (Figures 41a and b). These observations will be discussed in the next section.

A final point with regard to constituent particles is that they do not appear to contribute to the fracture process itself for this OLR = 1.8, OCR = 1:8000 spectrum. This statement is based on two observations: 1) The OL fracture surface is relatively flat; thus, the main crack does not seem to be deviating from a straight path through the material in an effort to find previously-fractured particles; 2) As can be seen particularly well in Figure 38b, crack growth in the vicinity of a fractured constituent is not significantly perturbed. Thus, while large second phase particles do influence OL retardation, they do not appear to affect the actual fracture process. This is in marked contrast to CA behavior at moderate to high ΔK , where void coalescence from constituent particles is a major crack growth mechanism.

5.3 Discussion of Phase 2 Results

In previous discussions, it was noted that there are several crack growth retardation mechanisms which may operate concurrently in these alloys. It is now appropriate to examine retardation characteristics of each of the 2 alloys in T6 and T7 tempers in relation to these various mechanisms.

The traditional view of FCG retardation is based on an observation that, following an overload excursion, crack growth rates will be attenuated as long as the crack tip remains within the monotonic OL plastic zone (30-32). Therefore, retardation should be enhanced by a larger plastic zone size, since greater crack extension would have to occur to grow out of the region of OL plasticity. Because plastic zone size is inversely related to yield strength (Figure 1), greater retardation is expected in low strength materials. This is clearly not the case for the data shown in Figure 35, where 7075 and 7050 in the low strength T7 temper exhibited much less retardation than these alloys in the high strength T6 temper.

The key to this apparent inconsistency lies in the fact that, at low stresses such as were used in this study, ΔK_{eff} within the OL plastic zone is suppressed to near-threshold magnitudes. For example, if a 1.8 OL is superimposed on a baseline ΔK_{app} of $3.3 \text{ MPa}\sqrt{\text{m}}$ ($3 \text{ ksi}\sqrt{\text{in.}}$), ΔK_{eff} for the first CA cycle after the OL will be less than $2.2 \text{ MPa}\sqrt{\text{m}}$ ($2 \text{ ksi}\sqrt{\text{in.}}$), according to the Vroman model. At these ΔK_{eff} values, Figures 11 and 12 indicate that growth rates will be much smaller for the T6 temper than for T7. Thus, even though ΔK_{eff} may be slightly lower for a T7 temper than for T6 because of the smaller yield strength in the overaged temper, the much lower crack growth rates for a peak-aged alloy result in greater retardation of crack growth in comparison to the T7 temper when ΔK_{eff} is reduced to near-threshold values.

Fatigue crack growth retardation is also expected when OL excursions cause local fracture of coarse second phase particles within the OL plastic zone (5, 7, 33). These secondary fractures relieve some of the crack tip strain energy,

thereby lowering ΔK_{eff} and reducing crack growth rates. Since the degree to which crack tip strain energy is relieved is related to the number of fractured particles, greater retardation is expected in alloys containing a large amount of coarse second phase particles. This was observed in previous studies (5, 7) in which low purity 7075 exhibited greater retardation than higher purity 7050 for the OLR = 1.8, OCR = 1:8000 OL spectrum at high stress levels. Similarly, greater retardation was observed in 7075 when compared to higher purity 7475 in both aircraft spectra and simple high-low block tests (33).

In the present results, it again is apparent that 7075 exhibits longer FCG lives (Figure 29) and greater retardation (Figure 35) than 7050 in the same temper. If this ranking were due to differences in strength level, then 7075 should have a lower yield strength than 7050 in both T6 and T7 tempers. Table 4 shows that this is not the case for the T7 temper, since the yield strength of 7075 is about 3% higher than that for 7050. This FCG performance ranking could, however, be due to the higher constituent volume fraction in 7075, and is reflected in the higher constituent particle density on the fracture surface of 7075 (Figure 37b) as compared to 7050 (Figure 36a). It is also evident in Figure 35 that the crack growth retardation advantage of 7075 over 7050 is greater in the T6 temper than in the overaged temper. Since the matrix in a higher-strength T6 temper is less able to accommodate hard constituents by plastic flow during crack tip deformation, fracture of these second phase particles is more likely than in the lower-strength T7 temper. Thus, a greater relative attenuation of crack growth rates would be expected for an alloy in the T6 temper than in a T7 condition. This hypothesis also is supported by the observation of greater constituent density on the fracture surface of 7075-T6 (Figures 38c and d) than of 7075-T7 (Figures 41c and d).

Knott and Pickard (21) recently discussed the effect of cyclic yield strength on OL fatigue crack growth retardation in an Al-Zn-Mg alloy. These authors observed that delay periods during which crack growth is retarded following overloads are greatest for the underaged condition and decrease with progressive aging to T6 and T7 conditions. The high cyclic work-hardening characteristics of the underaged temper cause a large elevation of cyclic yield strength during an OL excursion, and this yield strength increase must be relieved by cyclic softening prior to crack advance at lower baseline alternating stresses. The relatively small increase in cyclic yield strength for T6 and T7 tempers is relieved more quickly, so crack growth retardation is less in these tempers than in an underaged alloy. However, their data also indicate that delay periods are slightly greater for the T6 temper than for T7 in this aluminum alloy. In a separate investigation of the fatigue properties of various aluminum alloys (34), it was determined that 7075-T651 cyclically hardens to a small degree, while 7075-T7351 is cyclically stable. According to Knott and Pickard's arguments, this would be expected to result in greater post-OL retardation for the peak-aged alloy relative to an overaged condition.

The influence of cyclic yield strength on FCG retardation contributes to some fraction of the increase in fatigue life for alloys in the T6 temper over T7 in the present investigation. However, we believe that the observed temper effect on simple OL FCG retardation is primarily due to higher ΔK_{th} in the T6 temper. As previously discussed, CA crack growth rates are ten times lower for alloys in the T6 temper than for those in the T7 temper at the stress intensity levels to which ΔK_{eff} is suppressed initially by the 1.8 OL excursions.

Surely this difference in near-threshold CA crack growth rates has a greater effect on simple OL FCG lives than does the modest difference in cyclic tensile properties between T6 and T7 tempers.

5.4 Summary of Phase 2 Results

Periodic single overload tests were employed to evaluate retardation characteristics of slowly propagating (near-threshold) fatigue cracks in alloys 7075 and 7050 for both the T6 and T7-type tempers. Under the applied load spectrum, ranking of alloy performance was not always the same as rankings from constant load amplitude tests at similar applied ΔK levels. Comparison of this work with results on identical alloys tested under a similar load history, but at twice the applied stress (5, 7), indicated that retardation characteristics and fatigue performance rankings are highly dependent on the applied stress intensity factor magnitude. Variations in rankings generally indicate that crack growth retardation and propagation mechanisms change with different combinations of stress magnitude, load history, and flaw size. For this reason, the alloy microstructure which optimizes FCG resistance is application-dependent.

The retardation process involves a reduction of the effective crack tip stress intensity factor (ΔK_{eff}) during low amplitude stress cycles following an overload. These simple overload experiments and a previous study (5, 7) have identified two retardation mechanisms which can reduce ΔK_{eff} . The first is a result of overload plasticity, which increases crack closure forces (35) and promotes clamping forces developed by elastic constraints surrounding the

oversized plastic zone of the overload. This retardation mechanism is yield strength dependent; i.e., lower strength leads to larger overload plasticity and greater retardation. The second mechanism involves local cracking at constituent particles, which occurs during high tensile overloads. FCG retardation during subsequent lower stress cycles occurs because part of the main crack tip ΔK_{eff} is distributed among the local fractures. Since this mechanism is controlled by constituent volume fraction, a greater second phase particle density increases FCG retardation. Of course, if the OL ΔK approaches alloy toughness, crack growth can actually be accelerated by constituent fracture during overloads.

Comparison of results from CA and OL studies indicates that the same alloy microstructural characteristics may not optimize both CA FCG resistance and spectrum retardation behavior. For this reason, it is helpful to consider variable load amplitude crack growth as a two-stage process (Figure 42). In the first stage, a combination of load history and microstructural variables such as yield strength and constituent volume fraction control retardation and define ΔK_{eff} . Crack extension for each load cycle is then specified in stage 2 by the CA da/dN vs. ΔK relationship, where ΔK now equals ΔK_{eff} for each load excursion. Because retardation can reduce ΔK_{eff} to very small values, near-threshold FCG behavior may contribute significantly to spectrum fatigue performance. Therefore, the sensitivity of near-threshold fatigue resistance to alloy microstructure can carry over to FCG under variable amplitude load spectra.

General statements about the variable amplitude FCG resistance of a certain alloy microstructure are difficult to formulate, since metallurgical effects on both retardation and crack growth characteristics must be considered simultaneously. Nevertheless, the understanding of fatigue mechanisms acquired from simple overload history experiments does permit certain generalizations to be made. Such statements describe microstructural characteristics which enhance FCG resistance for classes of simple load sequences typical of many applications. Table 9 summarizes the statements listed below, which are the result of this study and prior work (5, 7) on the Al-Zn-Mg-Cu alloy system.

1. When prior overload cycles force effective ΔK values for numerous baseline cycles to near-threshold levels, longer fatigue crack growth lives may be expected for alloys in the T6 temper than those in a T7 temper. This is due to the greater constant load amplitude FCG resistance of the T6 temper at near-threshold crack growth rates. Load spectra for which a T6 temper should exhibit better FCG performance than T7 includes those histories where intermediate ΔK overloads are imposed at moderate to low frequencies on low to moderately low ΔK base cycles.

2. When frequently-applied overloads or baseline cycles at intermediate ΔK levels are the cycles in the load history during which most crack growth occurs, maximum spectrum fatigue life is achieved through optimizing intermediate ΔK FCG resistance. In this case, a T7 temper is favored over T6 because of the greater resistance to environmental degradation of FCG performance in the overaged condition.

3. One primary mechanism of overload-induced FCG retardation is controlled by the scale of overload plasticity. Crack growth retardation increases with crack tip plastic zone size, which itself varies inversely with yield strength. Therefore, overaging to a lower strength (T7) condition generally provides increased FCG resistance over the T6 temper when retardation is both significant (actual life appreciably greater than predicted by linear damage models) and controlled by crack tip plasticity. This retardation mechanism dominates when overload plastic strains are too small to cause appreciable secondary cracking at constituents (see statement 4 below).

4. When applied ΔK is high (i.e., approaching alloy K_{IC}) secondary cracking at coarse constituents contributes to reduced toughness and lower FCG resistance. Therefore, greater alloy purity (lower Fe, Si content) improves FCG resistance when baseline cycles are at high ΔK or when extremely high overloads cause appreciable crack extension. In contrast, secondary cracking at constituents can reduce ΔK_{eff} by lowering strain energy at the main crack tip. This in turn reduces crack growth rates during baseline load cycles following an overload excursion. As long as no appreciable growth occurs during an overload, the net effect can be to lower overall FCG rates. When this occurs, (e.g., high overloads applied with moderate frequency on low to medium ΔK base cycles), increasing alloy constituent volume fraction can increase fatigue life. This retardation mechanism is more effective in increasing FCG life when matrix yield strength is high, which favors the T6 temper over T7 for greater FCG resistance.

5. The effects of dispersoid type (Cr vs. Zr) and Cu content on simple overload FCG behavior were not examined for a low baseline stress level. However, based on constant load amplitude data (Phase 1) and simple overload results at a higher stress (5, 7), the influence of Cu and dispersoid type on FCG retardation is expected to be much less than the effects of temper and purity. It is presumed that the influence of Cu and dispersoid type on spectrum FCG behavior will be a result of their modest influence on constant load amplitude behavior at intermediate ΔK levels.

VI. CONCLUDING REMARKS AND RECOMMENDED FUTURE WORK

The FCG results for both constant amplitude and variable amplitude loading presented in this report include data for growth rates two orders of magnitude lower than those most often found in the literature and in handbooks (i.e., $da/dN > 10^{-8}$ m/cycle). These results suggest that the effect of alloy microstructure on FCG performance is different for low vs. high ΔK magnitudes, and for constant amplitude vs. spectrum loading. It appears that alloy selection for high fatigue resistance can be improved by considering low ΔK behavior; however, to do this we must look beyond our present means for ranking FCG performance.

The study of near-threshold behavior points out that significant increases in fatigue life may be possible through the use of alloys which can restrict the growth of small flaws during early stages of crack propagation; i.e., when ΔK is small. However, the present low ΔK fracture mechanics tests characterize growth of long, well-established cracks, as has been done in this study. The

link between short and long crack behavior at near-threshold rates has not been established, nor are the mechanisms of microcrack and early macrocrack growth well understood. Therefore, it is not clear that alloy resistance to the growth of small flaws can be optimized with present techniques and knowledge.

In addition, alloy performance targets and their integration with design philosophy should be reconsidered. We cite 7XXX alloy temper as an example: damage tolerant requirements dictate the use of a T7 temper for higher fracture toughness and a concurrent decrease in intermediate FCG rates by a factor of about 2 over the T6 temper. However, this choice may decrease fatigue life by an order of magnitude, compared to the T6 temper, because of substantially poorer near-threshold FCG resistance in the overaged alloy. Damage tolerant philosophy bypasses an appreciable fraction of fatigue life; namely, initiation and early crack growth.

This raises an interesting question - does alloy selection for FCG resistance based on damage tolerance requirements exact too great a penalty, either economic (e.g., excessive maintenance costs) or weight, when performance is projected over the expected service life of an aircraft fleet? Let us suppose that the requirements of damage tolerance (safety) can be guaranteed by design, inspection, and assurance of initial metal quality (e.g., minimum toughness guarantees). If so, then it is likely that alloy selection for fatigue resistance based on initiation and early crack growth will have greater impact on life cycle costs than selection based on damage tolerant characteristics.

Other examples of FCG performance tradeoffs based on load history-microstructure interactions can be cited readily; e.g., the effect of alloy purity on variable amplitude fatigue behavior. Because these interactions, and thus alloy selection for optimum fatigue performance, will be application dependent, it must be verified that laboratory test results can reliably predict alloy behavior in service. To this end, the generalizations in Tables 6 and 9 represent a basic level of understanding regarding effects of microstructure-load history interactions on Al-Zn-Mg-Cu alloy FCG resistance. Such generalizations, in conjunction with the rationale in Figure 42, represent a first step toward knowing which alloy microstructure produces optimum fatigue performance for a given "class" of application. These service classes need to be more clearly delineated through the development and use of standardized load spectra. Better alloy selection also will result if life prediction tools can incorporate understanding of microstructural interactions with variable amplitude load histories.

Acknowledgements

The authors express appreciation to R. E. Sanders, Jr., J. T. Staley, and R. A. Kelsey for their comments and critique of this manuscript. The experimental and analytical support provided by P. D. Emmert, P. H. Jacobus, and D. C. Sargent also is gratefully acknowledged.

REFERENCES

1. Bucci, R. J., "Development of a Proposed Standard Practice for Near-Threshold Fatigue Crack Growth Rate Measurement," ASTM STP 738, American Society for Testing and Materials, 1981, pp. 5-28.
2. Staley, J. T., "Microstructure and Toughness of High Strength Aluminum Alloys," ASTM STP 605, American Society of Testing and Materials, 1976, pp. 71-102.
3. Truckner, W. G., Staley, J. T., Bucci, R. J., and Thakker, A. B., "Effects of Microstructure on Fatigue Crack Growth of High Strength Aluminum Alloys," USAF Technical Report AFML-TR-76-169, 1976 October.
4. Staley, J. T., Truckner, W. G., Bucci, R. J., and Thakker, A. B., "Improving Fatigue Resistance of Aluminum Aircraft Alloys," Aluminum 11, 53, 1977 November, pp. 667-669.
5. Sanders, T. H., Jr., Sawtell, R. R., Staley, J. T., Bucci, R. J., and Thakker, A. B., "Effect of Microstructure on Fatigue Crack Growth of 7XXX Aluminum Alloys Under Constant Amplitude and Spectrum Loading," Final Report Naval Air Development Center, Contract No. N0019-C-0482, 1978 April 14.
6. Sanders, T. H., Jr., and Staley, J. T., "Review of Fatigue and Fracture Research on High-Strength Aluminum Alloys," Fatigue and Microstructure, Metals Park: American Society For Metals, 1979, p. 467.
7. Bucci, R. J., Thakker, A. B., Sanders, T. H., Sawtell, R. R., Staley, J. T., "Ranking 7XXX Aluminum Alloy Fatigue Crack Growth Resistance Under Constant Amplitude and Spectrum Loading," ASTM STP 714, American Society for Testing and Materials, 1980, pp. 41-78.
8. Ritchie, R. O., "Influence of Microstructure on Near-Threshold Fatigue-Crack Propagation in Ultra-High Strength Steels," Metal Science, August/September 1978, p. 368.
9. Yoder, G. R., Cooley, L. A., and Crooker, T. W., "Enhancement of Fatigue Crack Growth and Fracture Resistance in Ti-6Al-4V and Ti-6Al-6V-2Sn Through Microstructural Modifications," Journal of Engineering Materials and Technology, Volume 99, Series H, No. 4, 1977 October, pp. 313-318.
10. Crooker, T. W., "Subcritical Crack Growth in High Strength Alloys," Fracture Mechanics, edited by N. Perrone, et al, University Press of Virginia, 1978, p. 333.

11. Kirby, B. R., and Beevers, C. J., "Slow Fatigue Crack Growth and Threshold Behavior in Air and Vacuum of Commercial Aluminum Alloys," Fatigue of Engineering Materials and Structures, Volume 1, pp. 203-215, 1979.
12. Hertzberg, R. W. and Mills, W. J., "Character of Fatigue Fracture Surface Micromorphology in the Ultra-Low Growth Rate Regime," ASTM STP 600, American Society for Testing and Materials, 1976, pp. 220-234.
13. Bucci, R. J., "Spectrum Loading - A Useful Tool to Screen Effects of Microstructure on Fatigue Crack Growth Resistance," ASTM STP 631, American Society for Testing and Materials, 1977, pp. 388-401.
14. Bucci, R. J., "Selecting Aluminum Alloys to Resist Failure by Fracture Mechanisms," Engineering Fracture Mechanics, Volume 12, 1979, pp. 407-441.
15. Kaufman, J. G., and Holt, M., "Fracture Characteristics of Aluminum Alloys," Alcoa Research Laboratories Technical Paper No. 18, 1965.
16. Hudak, S. J., Saxena, A., Bucci, R. J., and Malcolm, R. C., "Development of Standardized Methods of Testing and Analyzing Fatigue Crack Growth Rate Data," AFML-TR-78-40, 1978 May.
17. Paris, P. C., Bucci, R. J., Wessel, E. T., Clark, W. G., Mager, T. R., "Extensive Study of Low Fatigue Crack Growth Rates in A533 and A508 Steels," ASTM STP 513, American Society for Testing and Materials, 1972, pp. 141-176.
18. Bucci, R. J., Paris, P. C., Hertzberg, R. W., and Anderson, A., "Very Slow Fatigue Crack Growth Rates in Air and Dry Argon for a Titanium-6Al-4V Alloy," ASTM STP 513, American Society for Testing and Materials, 1972, pp. 125-140.
19. Mackay, T., "Fatigue Crack Propagation Rate at Low ΔK of Two Aluminum Sheet Alloys, 2024-T3 and 7075-T6," Engineering Fracture Mechanics, Volume 11, pp. 753-761, 1979.
20. Coyne, E. J., Jr., and Starke, E. A., Jr., "The Effect of Microstructure on Fatigue Crack Growth Behavior of an Al-Zn-Mg-(Zr) Alloy," International Journal of Fracture, Volume 15, No. 5, 1979, pp. 405-417.
21. Knott, J. F., and Pickard, A. C., "Effects of Overloads on Fatigue Crack Propagation: Aluminum Alloys," Metal Science, August/September 1979, pp. 399-404.
22. Selines, R. J., and Pelloux, R. M., "Effect of Cyclic Stress Wave Form on Corrosion Fatigue Crack Propagation in Al-Zn-Mg Alloys," Metallurgical Transactions, March 1972, p. 2525.

23. Lin, Fu-Shiong, and Starke, E. A., Jr., "The Effect of Copper Content and Degree of Recrystallization on the Fatigue Resistance of 7XXX-Type Aluminum Alloys, II: Fatigue Crack Propagation," Materials Science and Engineering, Volume 43, 1980, pp. 65-76.
24. Starke, E. A., Jr., and Sanders, T. H., Jr., "The Effect of Microstructure on the Properties of High Strength Aluminum Alloys," Interim Report, Air Force Office of Scientific Research, AFOSR-78-3471, 1980 February.
25. Grosskreutz, J. C., "Strengthening and Fracture in Fatigue," Metallurgical Transactions, 3, 1972, p. 1255.
26. Filler, L. C., M.S. Thesis, Northwestern University, Evanston, Illinois, 1981.
27. Jones, R. L., and Coyle, T. E., "The Mechanical, Stress-Corrosion, Fracture Mechanics, and Fatigue Properties of 7050, 7475, and Ti-8Mo-8V-2Fe-3Al Plate and Sheet Alloys," General Dynamics, Fort Worth Division, Report FGT-5791, 1976.
28. Schra, L., "Engineering Property Comparisons for Four Al-Zn-Mg-Cu Type Forging Alloys," National Aerospace Laboratory (Netherlands), Report NLR TR 79022U, 1979.
29. Vroman, G., "Analytical Prediction of Crack Growth Retardation Using a Critical Stress Intensity Concept," North American Rockwell, Los Angeles Division, Technical Report TFR 71-701, 1971.
30. Wheeler, O. E., "Crack Growth Under Spectrum Loading," Journal of Basic Engineering Transactions, 1972, pp. 181-186.
31. Trebules, V. W., Roberts, R., and Hertzberg, R. W., in Progress in Flaw Growth and Fracture Toughness Testing, ASTM STP 536, American Society for Testing and Materials, 1973, pp. 115-146.
32. Mills, W. J., and Hertzberg, R. W., "Load Interaction Effects on Fatigue Crack Propagation in 2024-T3 Aluminum Alloy," Engineering Fracture Mechanics, 8 (4), 1976, p. 657.
33. Schulte, K., Trautmann, K. H., and Nowack, H., "Influence of the Microstructure of High Strength Aluminum Alloys on Fatigue Crack Propagation Under Variable Amplitude Loading," presented at International Conference on Analytical and Experimental Fracture Mechanics, Rome, 1980.
34. Sanders, T. H., Jr., Staley, J. T., and Mauney, D. A., "Strain Control Fatigue as a Tool to Interpret Fatigue Initiation of Aluminum Alloys," presented at 10th Annual International Symposium on Materials Science, Seattle, 1975.
35. Elber, W., "The Significance of Fatigue Crack Closure," ASTM STP 486, 1971, p. 236.

TABLE 1. REMELT CHEMICAL ANALYSES OF LAB FABRICATED ALLOYS

S. No.	Alloy Type	Composition (weight per cent)							
		Si	Fe	Cu	Zr	Cr	Mg	Zn	Ti
454542	7010 Low-purity 7010	0.06	0.10	1.56	0.12	0.00	2.19	6.20	0.02
454547		0.19	0.27	1.55	0.12	0.00	2.22	5.96	0.03
454545	7475 7075	0.06	0.11	1.46	0.00	0.21	2.09	5.90	0.02
454549		0.23	0.28	1.51	0.00	0.23	2.26	6.34	0.02
454543	7050 Low-purity 7050	0.07	0.11	2.10	0.13	0.00	2.16	6.16	0.02
454548		0.19	0.28	2.16	0.11	0.01	2.18	5.83	0.02
454546	High-Cu 7475 High-Cu 7075	0.06	0.11	2.27	0.00	0.21	2.08	5.90	0.02
454551		0.23	0.28	2.29	0.00	0.20	2.23	6.13	0.02

TABLE 2. HEAT TREATMENTS

S. No.	Alloy Type	Temper Type	Aging Practice
454542	7010	T7	24 hr 121°C+37 hr 163°C
454547	Low-purity 7010	T7	24 hr 121°C+24 hr 163°C
454545	7475	T7	24 hr 121°C+21 hr 163°C
454549	7075	T7	24 hr 121°C+12 hr 163°C
454543	7050	T7	24 hr 121°C+40 hr 163°C
454548	Low-purity 7050	T7	24 hr 121°C+32 hr 160°C
454546	High-Cu 7475	T7	24 hr 121°C+18 hr 163°C
454551	High-Cu 7075	T7	24 hr 121°C+24 hr 163°C
454550	7075	T6	24 hr 121°C
454544	7050	T6	100 hr 121°C

Solution heat treat - 2 hr 488°C, quench in water at room temperature,
stretch 1-1/2%.

TABLE 3. CONSTITUENT AND DISPERSOID PHASES IDENTIFIED BY GUINIER-deWOLFF
X-RAY DIFFRACTION

S. No.	Alloy Type	Mg ₂ Si	Al ₇ Cu ₂ Fe β (Al-Cu-Fe)	Al ₁₂ Mg ₂ Cr	Al ₂ CuMg	(Fe,Cu)Al ₆ α (Al-Cu-Fe)
454542 454547	7010 Low-purity 7010	sml med	sml med	-- --	-- --	-- --
454545 454549	7475 7075	sml med	sml med	med med	poss.trace poss.trace	poss.trace trace
454543 454548	7050 Low-purity 7050	sml med	sml med	-- --	-- poss.trace	-- --
454546 454551	High-Cu 7475 High-Cu 7075	sml med	sml med	med med	-- poss.trace	-- --

TABLE 4. LONGITUDINAL MECHANICAL PROPERTIES OF 6.35 mm (0.25 in.) THICKNESS 7XXX ALUMINUM PLATE

Alloy Type and Temper	S. No.	Tensile Strength, (a)		Yield Strength, (a)		Elongation, (a)		(b)		Unit Propagation (b), Energy in. lb/in. ²
		MPa	ksi	MPa	ksi	%		Tensile Str. Yield Str.	KJ/M ²	
7010-T7 Low-purity 7010-T7	454542	517	75.0	454	65.9	13		1.45	595	105
	454547	490	71.1	435	63.1	11.5		1.28	380	66.5
7475-T7 7075-T7	454545	505	73.2	441	64.0	13		1.38	510	89.5
	454549	505	73.2	454	65.8	11		1.16	280	49.0
7050-T7 Low-purity 7050-T7	454543	511	74.1	440	63.8	14		1.46	645	115
	454548	496	71.9	435	63.1	12		1.29	385	67.5
High-Cu 7475-T7 High-Cu 7075-T7	454546	532	77.1	470	68.1	12		1.32	450	79.0
	454551	505	73.3	446	64.7	11.5		1.19	270	47.5
7075-T6 7050-T6	454550	558	81.0	530	76.9	9.5		1.02	200	35.0
	454544	612	88.7	570	82.7	12		1.19	545	95.5

- (a) Established using full thickness, 51 mm (2 in.) gauge length specimens per ASTM-E8.
(b) An index of fracture toughness, established from average of triplicate 6.4 mm (0.25 in.) thick Kahn-type tear specimens (experimental procedures detailed in Refs. 14 and 15).

TABLE 5. CALCULATED VOLUME % OF CONSTITUENTS AND DISPERSOIDS

S. No.	Alloy Type	(Al ₃ Zr, Al ₁₂ Mg ₂ Cr) Dispersoids	(Al ₇ Cu ₂ Fe, Mg ₂ Si) Constituents
454542	7010	0.15	0.64
454547	Low-purity 7010	0.15	1.84
454545	7475	1.24	0.68
454549	7075	1.40	2.02
454543	7050	0.16	0.72
454548	Low-purity 7050	0.14	1.88
454546	High-Cu 7475	1.22	0.68
454551	High-Cu 7075	1.17	2.02

TABLE 6

EFFECT OF MICROSTRUCTURAL VARIANTS ON CONSTANT AMPLITUDE FCG RESISTANCE OF 7075
AND 7050 TYPE HIGH STRENGTH ALUMINUM ALLOYS TESTED IN THE PRESENCE OF MOISTURE AT $R = 1/3$

Microstructure Variants	Near Threshold ΔK $\Delta K \leq 3.3 \text{ MPa}\sqrt{\text{m}} \text{ (3 ksi}\sqrt{\text{in.}})$	Intermediate ΔK $3.3 < \Delta K < 13.2 \text{ MPa}\sqrt{\text{m}}$	High ΔK $\Delta K \geq 13.2 \text{ MPa}\sqrt{\text{m}} \text{ (12 ksi}\sqrt{\text{in.}})$	Comments
Purity (Fe, Si content)	Little effect noted in these experiments.	Small increase in FCG resistance with purity increase, particularly at high ΔK within this regime. (3-7)	High purity alloys show superior FCG resistance (3-7)	Lower purity implies higher volume fraction constituent from which microvoids initiate and coalesce under high tensile strains.
Cu content (1.0 to 2.3%)	Little or no effect apparent in this work. However, other studies covering wider Cu range (0.01-2.1%) indicate that FCG resistance degraded by Cu additions. (23, 24)	FCG resistance increases with Cu increase by reducing degradation by moisture. The benefit of Cu addition diminishes when either moisture effects are removed or ΔK is decreased. (3, 23, 24)	Effect of Cu addition on FCG performance vanishes as K values approach material toughness.	The effect of Cu at low ΔK needs further verification. Nevertheless, this study suggests that any influence of Cu will be less than that of temper (see below).
Dispersoid type (Zr vs. Cr)	Little or no effect apparent in this work. Work by Filler (20) indicates that substitution of Zr improves FCG resistance in dry argon.	Increasing dispersoid volume fraction reduces FCG resistance at higher ΔK values in low toughness alloys, while little or no effect is detectable at lower ΔK values in this regime. (5, 7)	FCG resistance decreases with increase in dispersoid volume fraction, but reduction is on smaller scale than that attributed to purity (Fe, Si) differences. (2, 5, 7)	The effect of dispersoid type on low ΔK FCG resistance is not clear. Any effect expected to be less than that of temper (see below).
Temper	FCG resistance decreases with increase in degree of aging (i.e., with decreasing precipitate coherency).	Overaging increases FCG resistance by reducing degradation by environment. (3-7)	FCG resistance increases with toughness increase in overaged tempers. (3,4,14)	Temper has greatest effect on low ΔK fatigue performance.

TABLE 7

COMPARISON OF EXPERIMENTAL AND PREDICTED FCG LIVES
FOR AN OLR = 1.8, OCR = 1:8000 SIMPLE OVERLOAD
FROM AN INITIAL CRACK LENGTH OF 8.9 mm

Initial Half Crack Length = 8.9 mm (0.35 in.)
Final Half Crack Length = 27.9 mm (1.1 in.)
1 Block = 8000 CA + 1 OL Cycles
Specimen Geometry - 102 X 6.4 mm (4 X 0.25 in.) CCT Panel

	7075		7050	
	T6	T7	T6	T7
Experimental Life* (Fig. 29)	5,684	1,810	3,928	1,254
Predicted Life* Actual Spectrum	11,500	1,309	28,212	1,135
Predicted Life* No Retardation	124	236	223	266
Predicted Life* Complete Retardation	46,500	120,500	89,000	129,600

* Life = Number of loading blocks

TABLE 8

COMPARISON OF EXPERIMENTAL AND PREDICTED FCG LIVES
FOR AN OLR = 1.8, OCR = 1:8000 SIMPLE OVERLOAD
SPECTRUM FROM AN INITIAL CRACK LENGTH OF 12.7 mm

Initial Half Crack Length = 12.7 mm (0.5 in.)
Final Half Crack Length = 27.9 mm (1.1 in.)
1 Block = 8000 CA + 1 OL Cycles
Specimen Geometry 102 X 6.4 mm (4 X 0.25 in.) CCT Panel

	7075		7050	
	T6	T7	T6	T7
Experimental Life*	2,982	902	2,013	544
Predicted Life*	1,535	557	2,475	674

* Life = Number of loading blocks

TABLE 9

INFLUENCE OF MICROSTRUCTURAL VARIABLES ON SIMPLE OVERLOAD SPECTRUM FCG IN 7XXX ALUMINUM ALLOYS

Microstructural Variable Affecting FCG	Rationale for Observed Influence	Load Histories on Which Microstructure Enhances FCG Resistance
Temper:		
T6 favored over T7	<p>a) If ΔK_{eff} for significant number of load cycles is suppressed to near-threshold values, superior low ΔK FCG resistance of T6 will result in longer FCG life than for T7.</p> <p>b) Second phase particle fracture in OI plastic zone can reduce ΔK_{eff} and reduce FCG rates. High matrix strength promotes constituent fracture.</p>	<p>Constant or variable amplitude spectra when applied ΔK is low.</p> <p>Overloads at intermediate ΔK levels imposed with moderate to low frequency on low to intermediate ΔK base cycles.</p> <p>High overloads imposed with moderate frequency on low to intermediate ΔK base cycles.</p>
T7 favored over T6	<p>a) Overaging increases alloy toughness and reduced moisture-assisted degradation of FCG resistance at intermediate growth rates.</p> <p>b) If FCG retardation is significant and controlled by overload plasticity, then overaging to reduce strength increases fatigue life.</p>	<p>Constant amplitude or low level overload spectra at moderate to high ΔK base.</p> <p>Spectra in which intermediate to high ΔK overloads are applied frequently.</p> <p>Intermediate ΔK overloads imposed on moderate to low ΔK base cycles.</p>
Purity:		
High purity (low Fe, Si)	When particle fracture accelerates crack growth, a low constituent volume fraction is desirable.	<p>High ΔK constant amplitude loading.</p> <p>Overloads at extremely high ΔK approaching alloy toughness.</p>
Low purity (high Fe, Si)	When local particle fracture reduces ΔK_{eff} and does not contribute to FCG, a high constituent volume fraction enhances retardation.	Spectra for which the ratio of tensile overload to base cycles is high and the base ΔK is moderate.

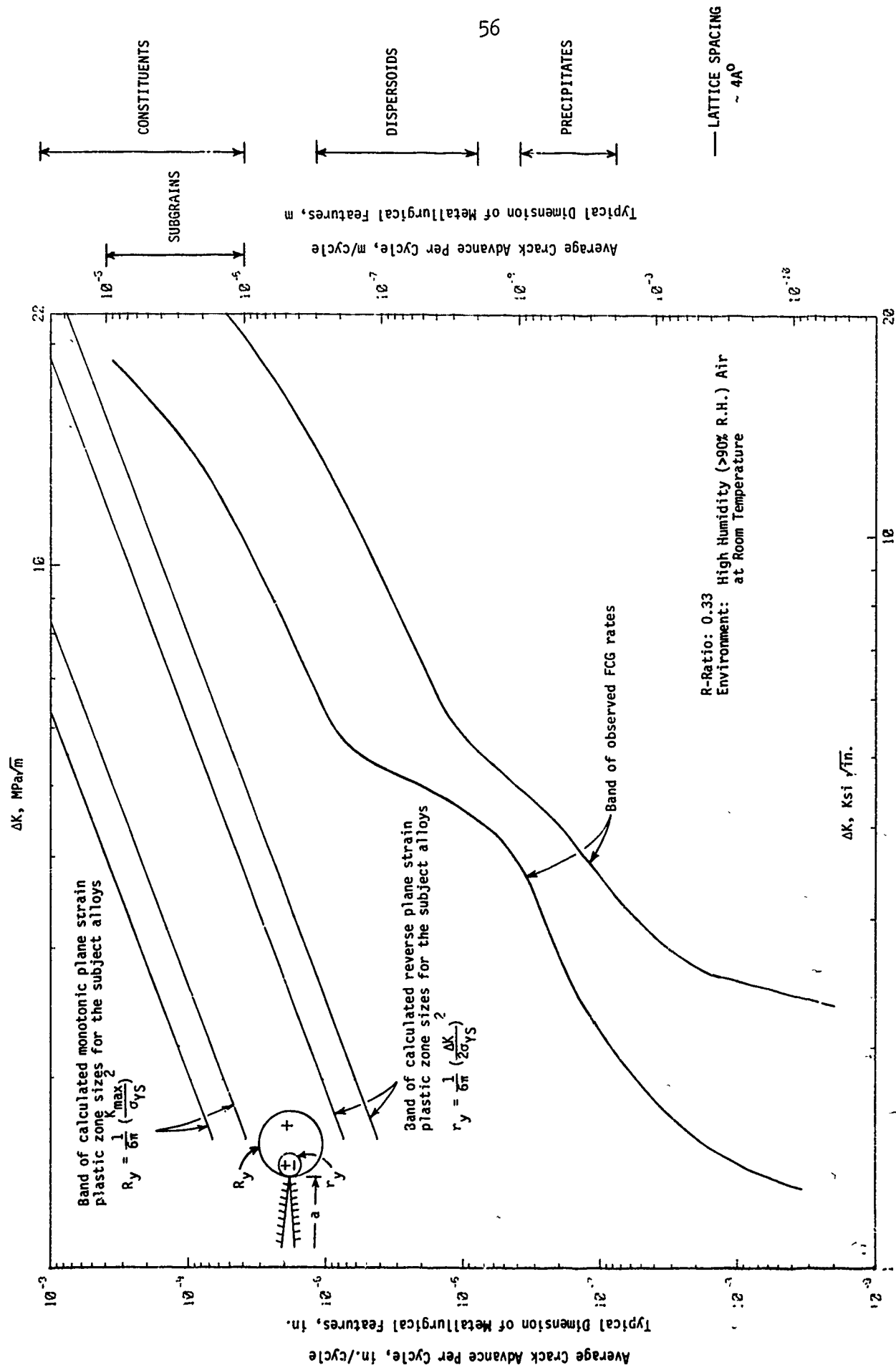
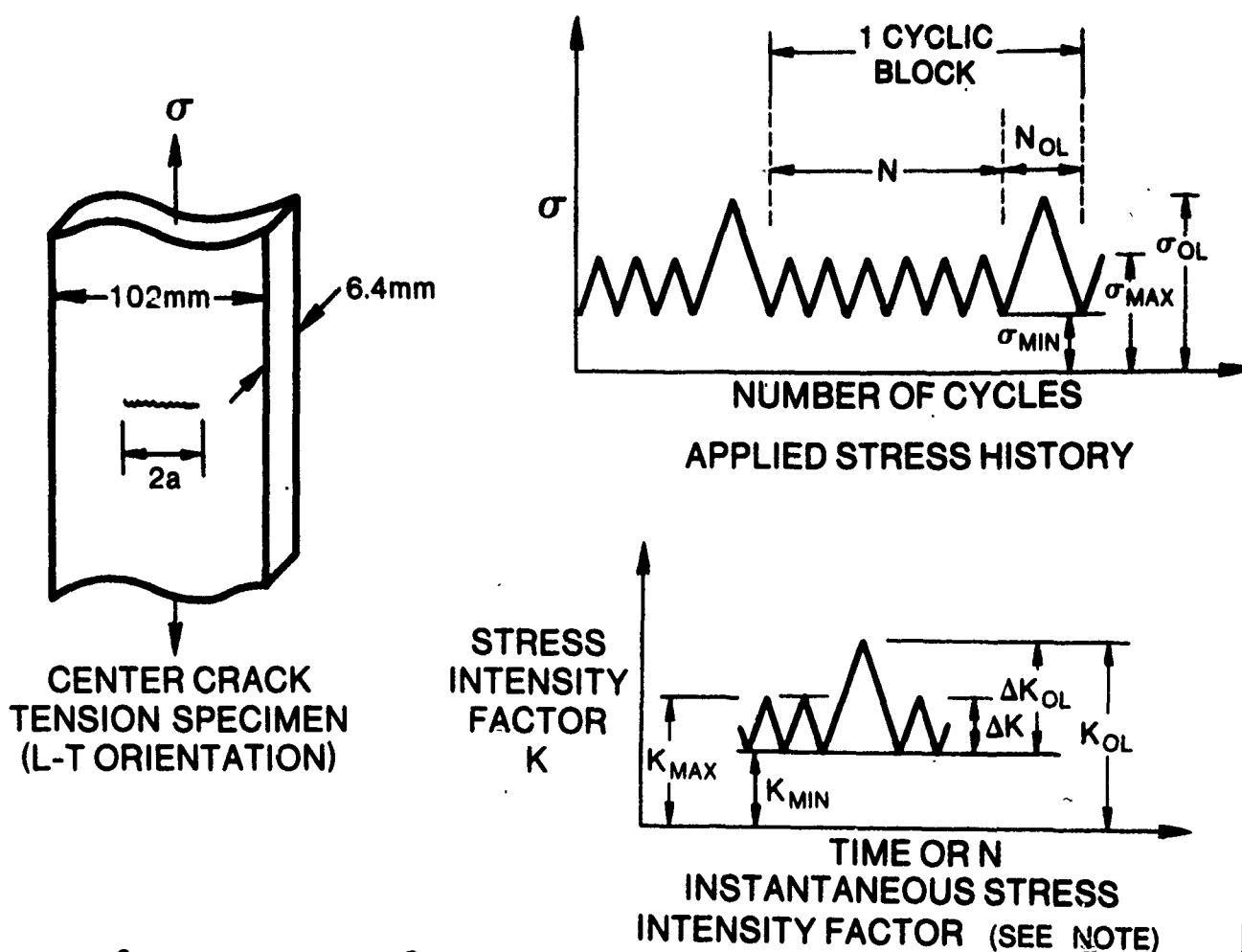


FIG. 1 RELATIONSHIP OF INCREMENTAL CRACK ADVANCE PER CYCLE TO SIZE OF MICROSTRUCTURAL FEATURES AND ESTIMATED PLASTIC ZONE SIZE(S) AHEAD OF CRACK TIP IN SUBJECT LABORATORY FABRICATED 7XXX ALUMINUM ALLOYS



$$\sigma_{MAX} = \begin{cases} 28.6 \text{ MPa} \\ 55.2 \text{ MPa} \end{cases}, \quad \sigma_{MIN} = \begin{cases} 9.5 \text{ MPa} \\ 18.3 \text{ MPa} \end{cases}$$

SUBJECT INVESTIGATION
PREVIOUS INVESTIGATION, REF. 5

$$R = \text{CONSTANT AMPLITUDE STRESS RATIO} = \sigma_{MIN}/\sigma_{MAX} = K_{MIN}/K_{MAX} = 1/3$$

$$OLR = \text{OVERLOAD RATIO} = \sigma_{OL}/\sigma_{MAX} = K_{OL}/K_{MAX}$$

$$N = \text{NUMBER OF CONSTANT AMPLITUDE CYCLES}$$

$$N_{OL} = \text{NUMBER OF OVERLOAD CYCLES (=1)}$$

$$OCR = \text{OCCURRENCE RATIO} = N_{OL}/N$$

NOTE: APPLIED STRESS HISTORY CONSTANT FOR DURATION OF TEST. NOMINAL K VALUES, THEREFORE, INCREASE WITH CRACK EXTENSION

FIG. 2 DESCRIPTION OF PERIODIC SINGLE SPIKE OVERLOAD TESTS

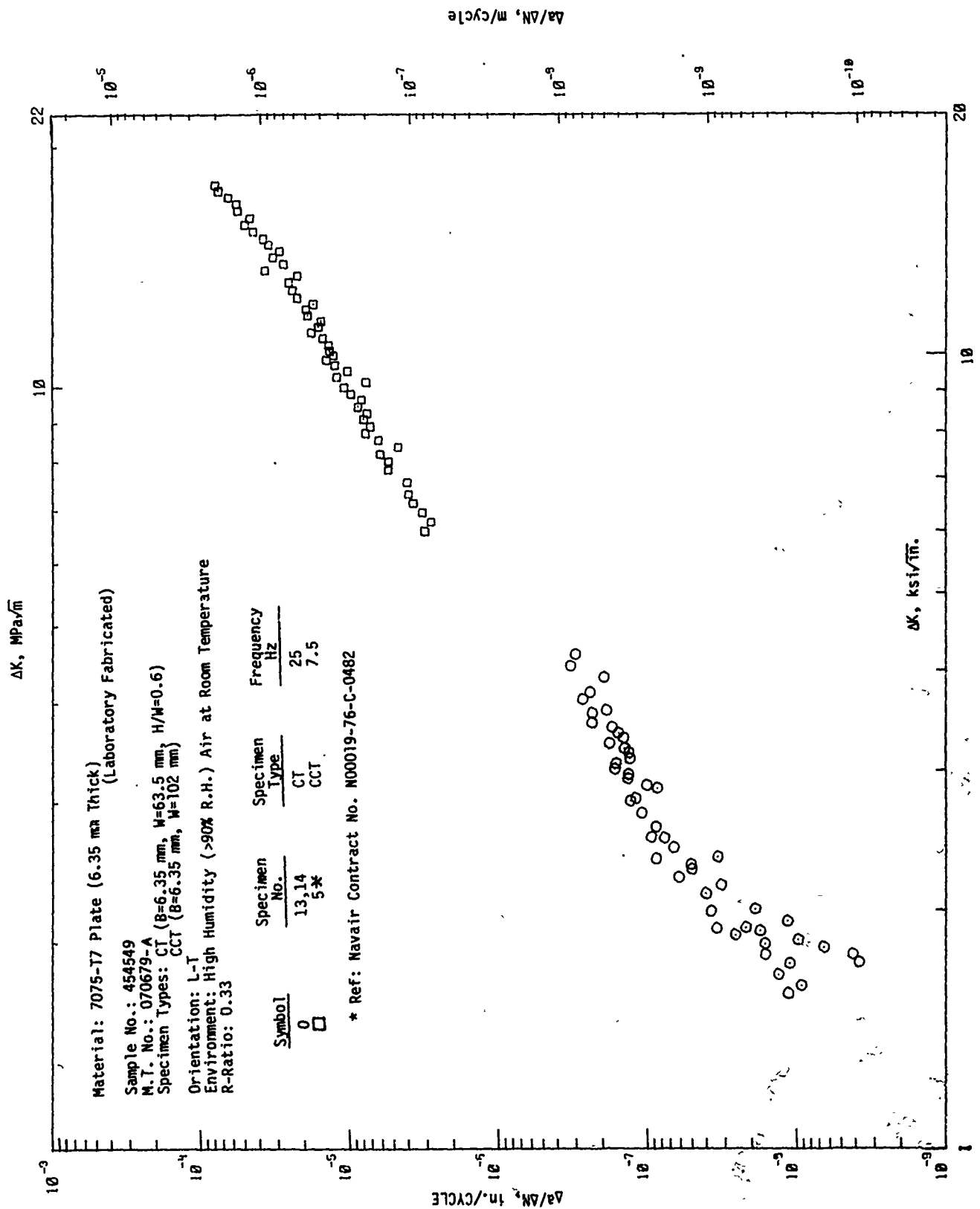


FIG. 3 IC STRESS INTENSITY RANGE, ΔK , VERSUS CYCLIC FATIGUE CRACK GROWTH RATE, da/dN , OF 7075-T7 PLATE (6.35 mm THICK)

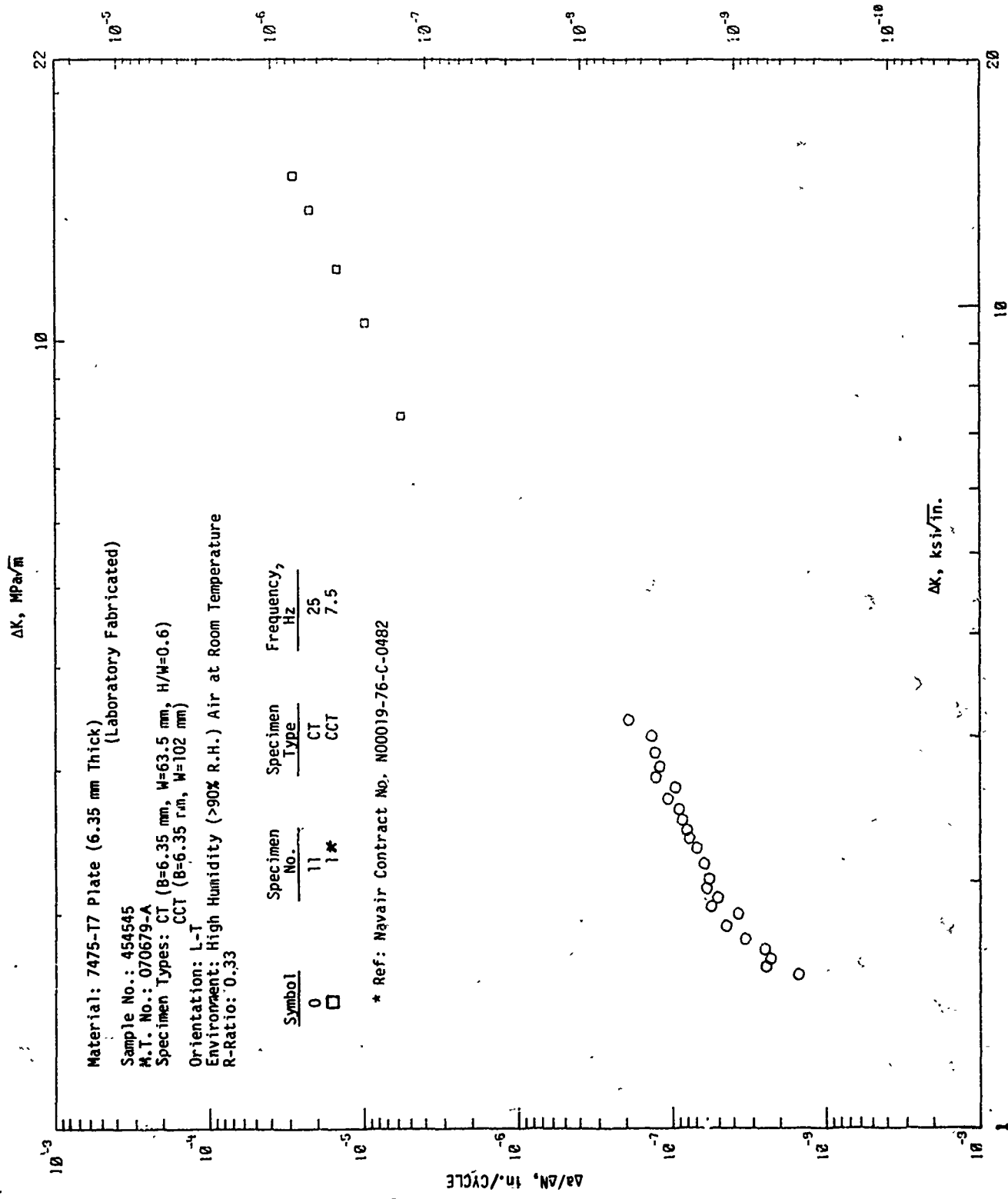


FIG. 4 CYCLIC STRESS INTENSITY RANGE, ΔK , VERSUS CYCLIC FATIGUE CRACK GROWTH RATE, da/dN , OF 7475-T7 PLATE (6.35 mm THICK)

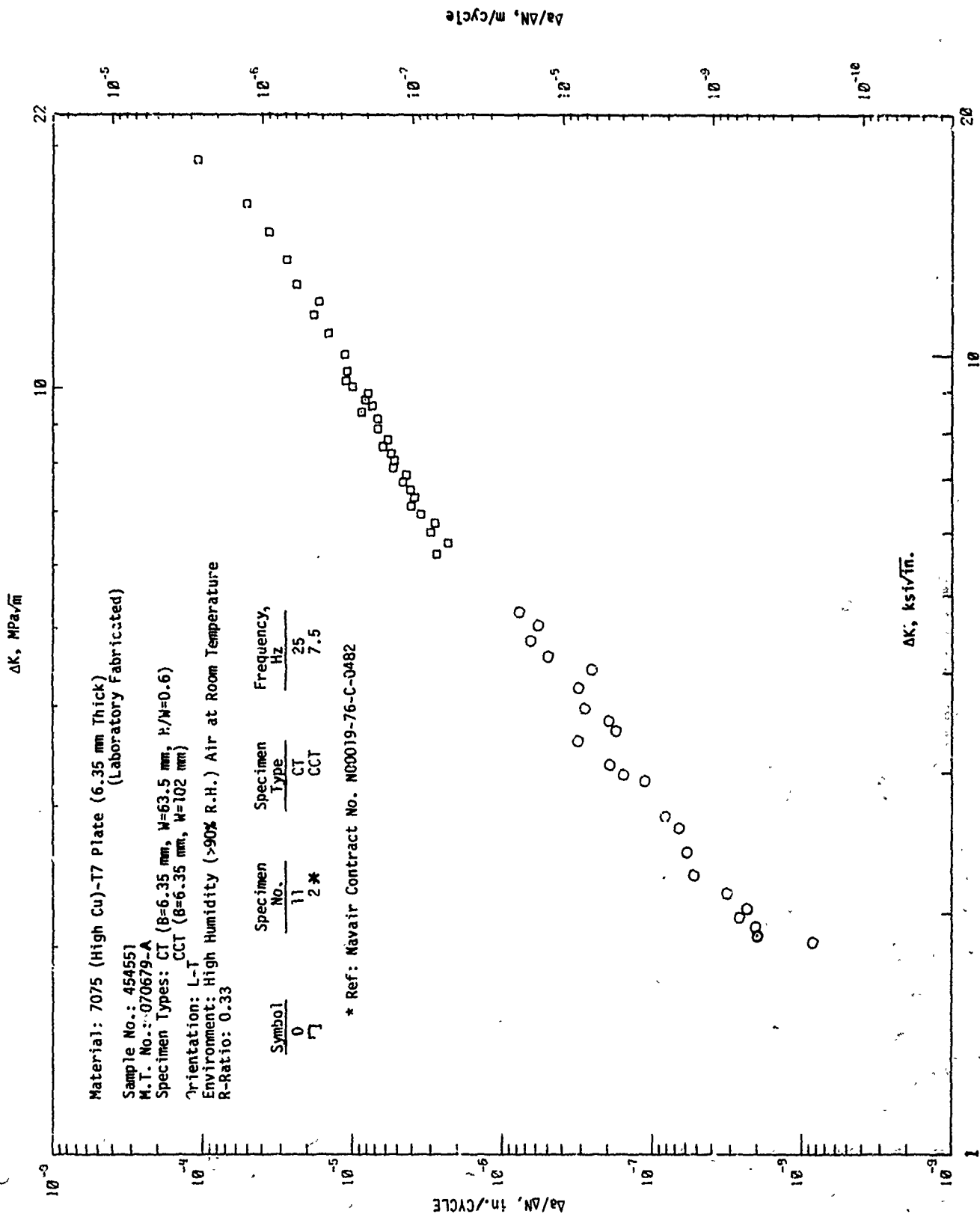


FIG. 5 CYCLIC STRESS INTENSITY RANGE, ΔK , VERSUS CYCLIC FATIGUE CRACK GROWTH RATE, $\Delta a/\Delta N$, OF 7075 (HIGH CU)-T7 PLATE (6.35 mm THICK)

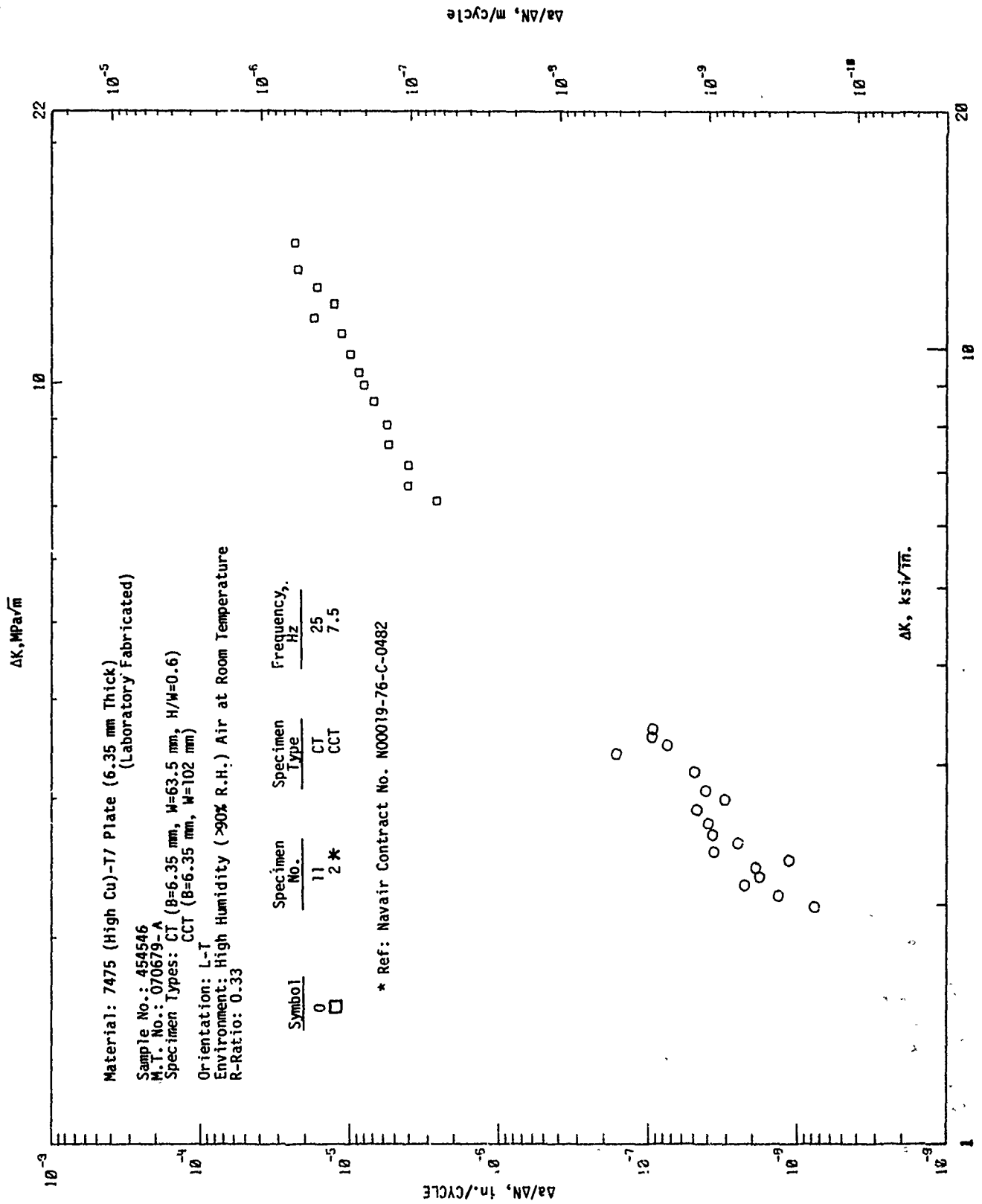


FIG. 6 CYCLIC STRESS INTENSITY RANGE, ΔK , VERSUS CYCLIC FATIGUE CRACK GROWTH RATE, $\Delta a/\Delta N$, OF 7475 (High Cu)-T7 PLATE (6.35 mm THICK)

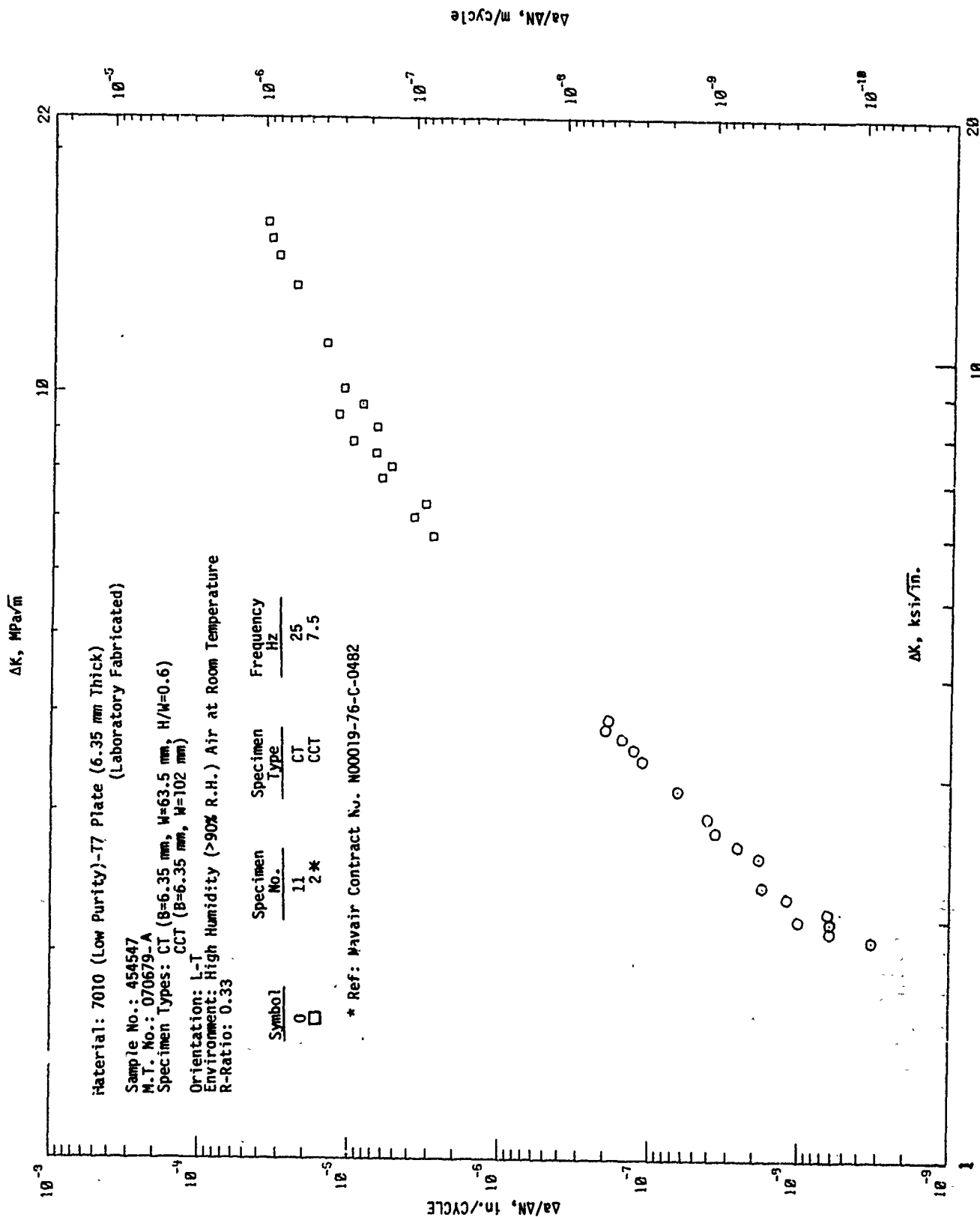


FIG. 7 CYCLIC STRESS INTENSITY RANGE, ΔK , VERSUS CYCLIC FATIGUE CRACK GROWTH RATE $\Delta a/\Delta N$ OF 7010 (LOW PURITY)-T7 PLATE (6.35 mm THICK).

$\Delta K, \text{MPa}\sqrt{\text{m}}$

Material: 7050 (Low Purity)-T7 Plate (6.35 mm Thick)
(Laboratory Fabricated)

Sample No.: 454548

M. T. No.: 070679-A

Specimen Types: CT (B=6.35 mm, W=63.5 mm, H/W=0.6)
CCT (B=6.35 mm, W=102 mm)

Orientation: L-T
Environment: High Humidity (>90% R.H.) Air at Room Temperature
R-Ratio: 0.33

Symbol	Specimen No.	Specimen Type	Frequency, Hz
○	11	CT	25
□	2*	CCT	7.5

* Ref: Navair Contract No. N00019-76-C-0482

$\Delta a/\Delta N, \text{in./cycle}$

$\Delta a/\Delta N, \text{m/cycle}$

$\Delta K, \text{ksi}/\sqrt{\text{in.}}$

FIG. 9 CYCLIC STRESS INTENSITY RANGE, ΔK , VERSUS CYCLIC FATIGUE CRACK GROWTH RATE, $\Delta a/\Delta N$, OF 7050 (Low Purity)-T7 PLATE (6.35 mm THICK)

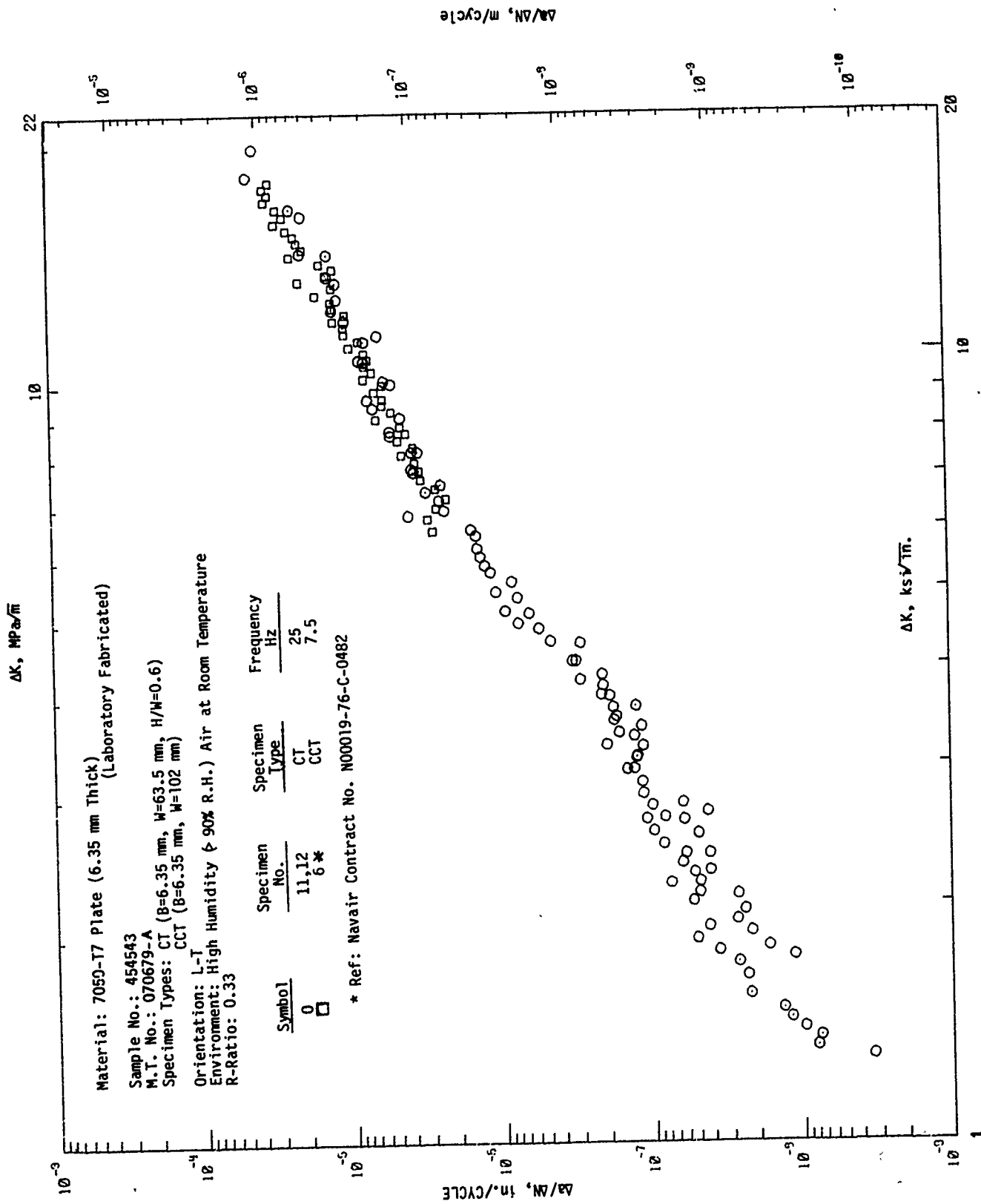


FIG. 10 CYCLIC STRESS INTENSITY RANGE, ΔK , VERSUS CYCLIC FATIGUE CRACK GROWTH RATE, $\Delta a/\Delta N$, OF 7050-T7 PLATE (6.35 mm THICK)

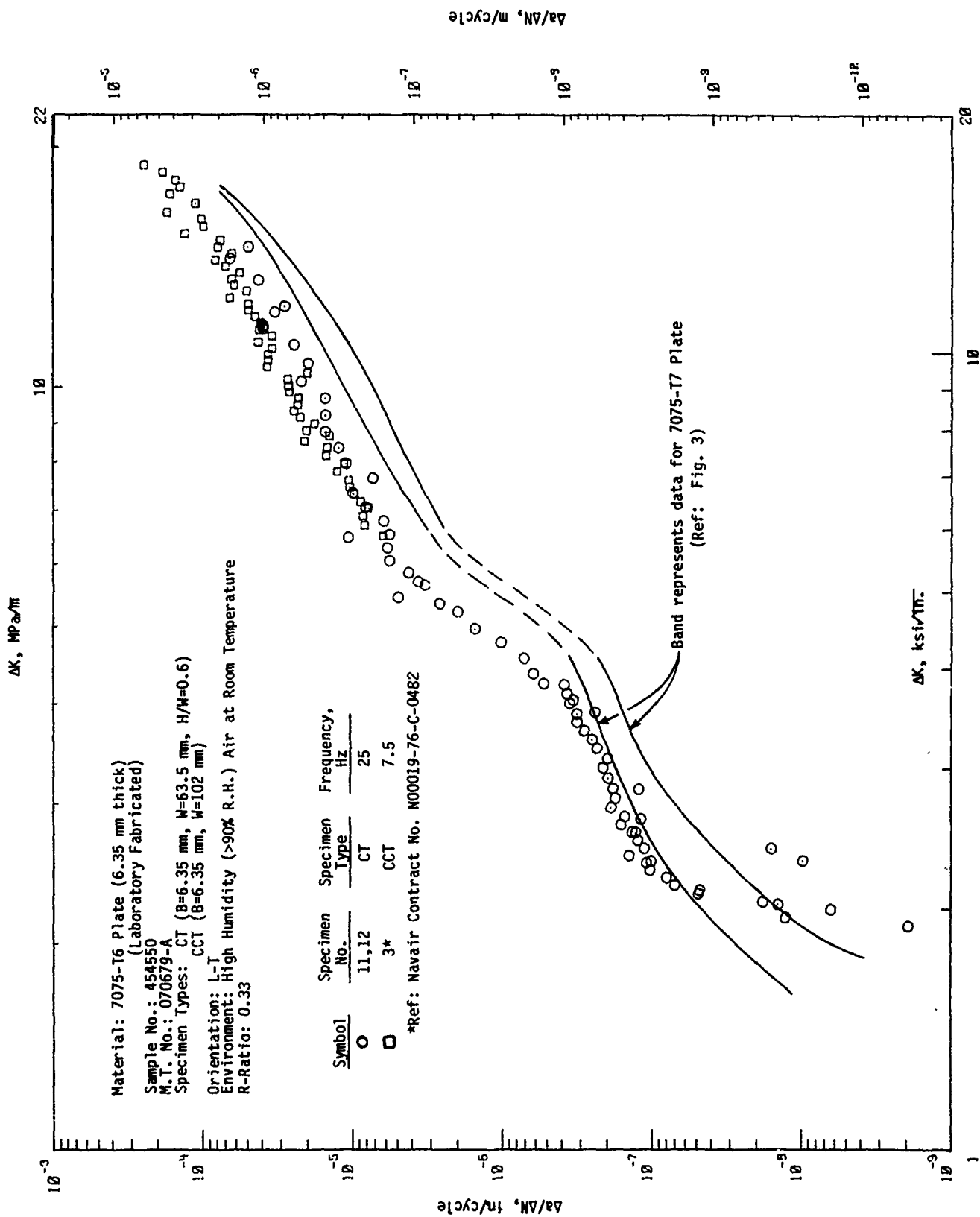


FIG. 11 CYCLIC STRESS INTENSITY RANGE, ΔK , VERSUS CYCLIC FATIGUE CRACK GROWTH RATE, $\Delta a/\Delta N$, OF 7075-T6 PLATE (6.35 mm THICK)

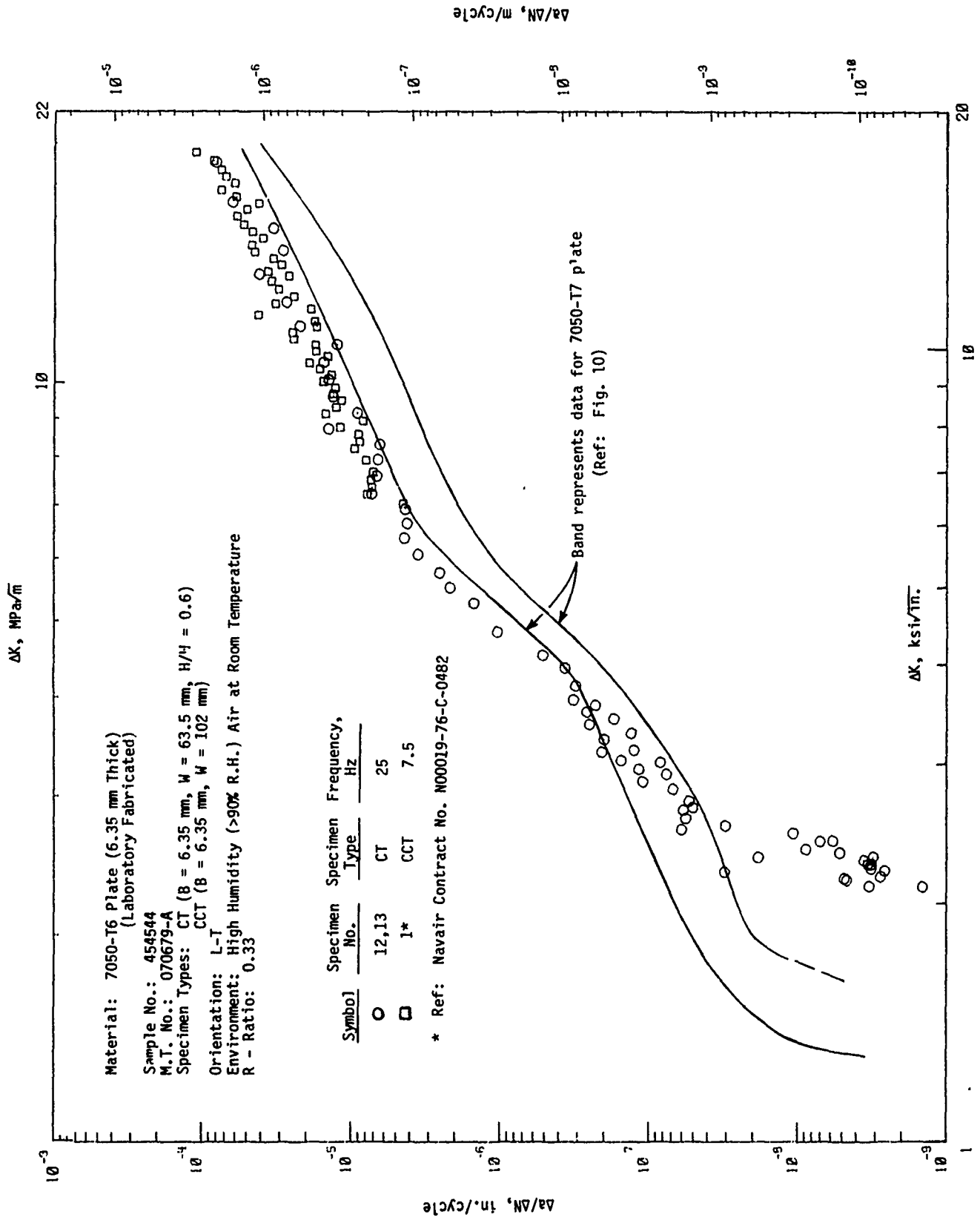


FIG. 12 CYCLIC STRESS INTENSITY RANGE, ΔK , VERSUS CYCLIC FATIGUE CRACK GROWTH RATE, $\Delta a/\Delta N$, OF 7050-T6 PLATE (6.35 mm THICK).

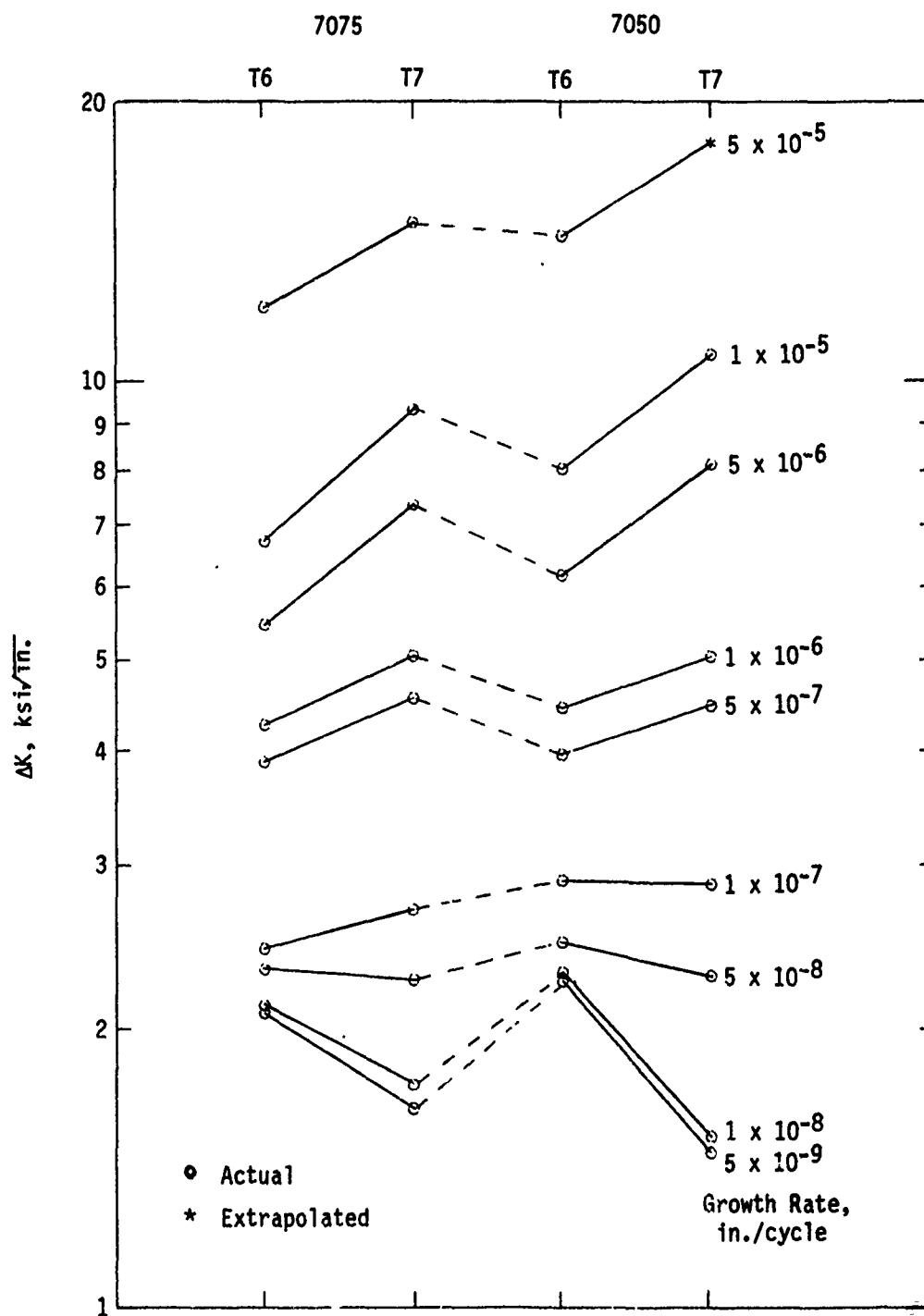


FIG. 13 EFFECT OF TEMPER ON CONSTANT-AMPLITUDE FATIGUE CRACK GROWTH RESISTANCE OF ALUMINUM ALLOYS 7050 AND 7075 IN HIGH HUMIDITY (75% R.H.) AIR AT ROOM TEMPERATURE AT AN R-RATIO OF 0.33

Metric (SI) conversion factors:

1 in. = 0.0254 m

1 $\text{ksi}\sqrt{\text{in.}}$ = 1.1 $\text{MPa}\sqrt{\text{m}}$

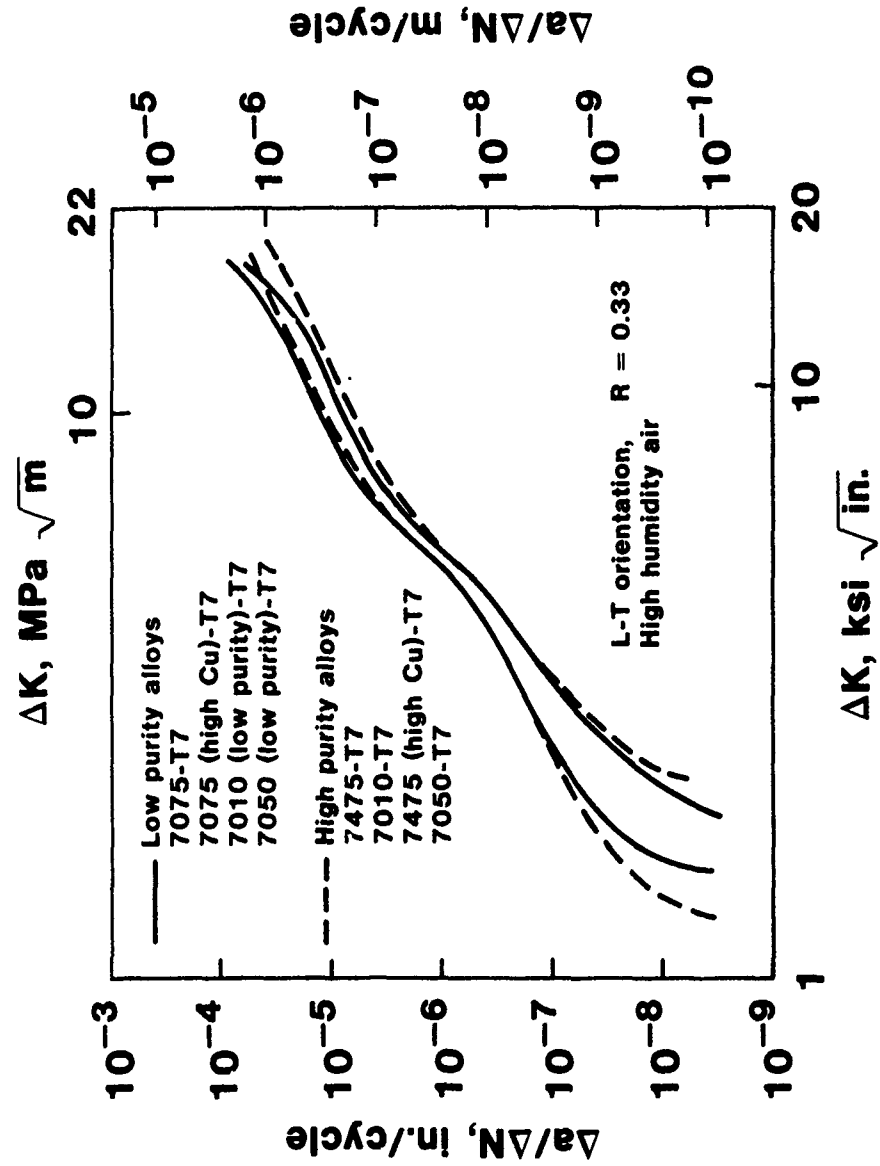


Figure 14. Effect of Purity on Constant Amplitude Fatigue Crack Growth Resistance of 7XXX-T7 Aluminum Alloys in High Humidity (> 90% R.H.) Air at Room Temperature at an R-Ratio of 0.33.

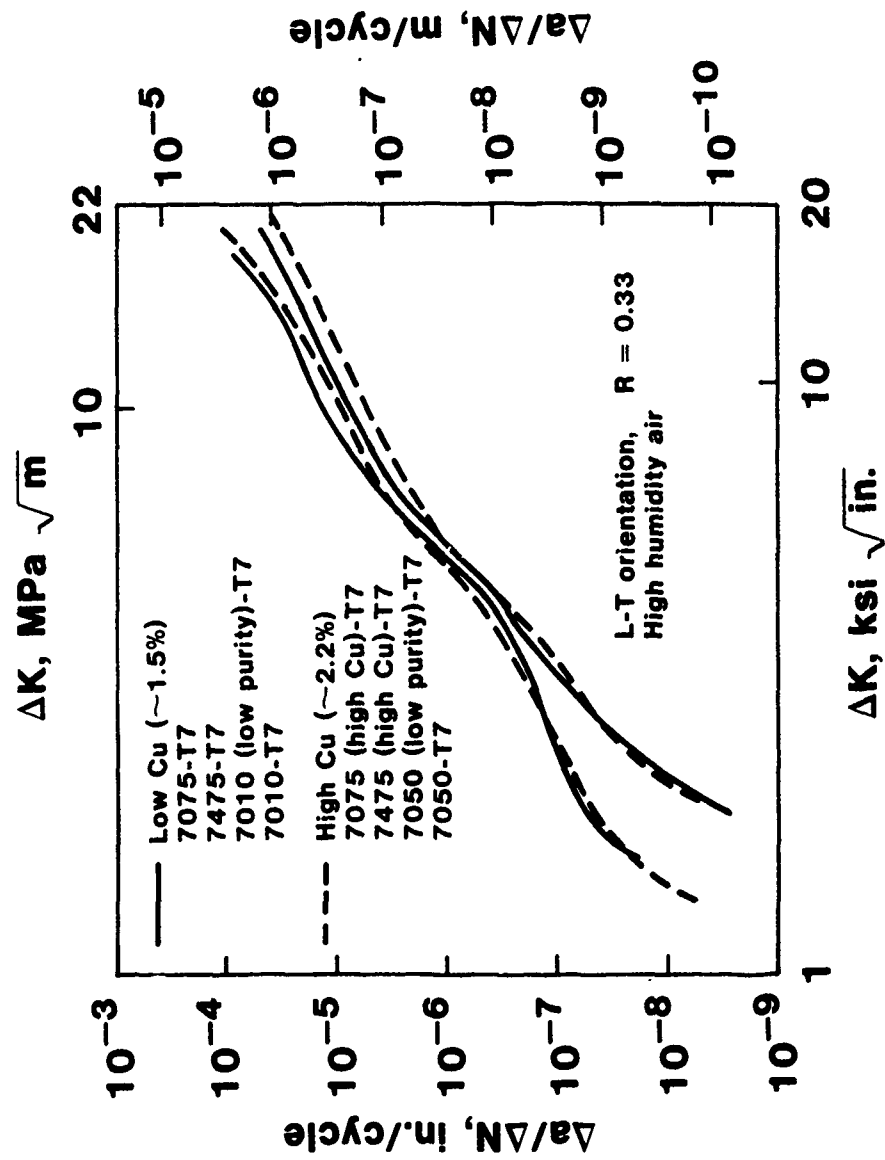


Figure 15. Effect of Copper Content on Constant Amplitude Fatigue Crack Growth Resistance of 7XXX-T7 Aluminum Alloys in High Humidity (> 90% R.H.) Air at Room Temperature at an R-Ratio of 0.33.

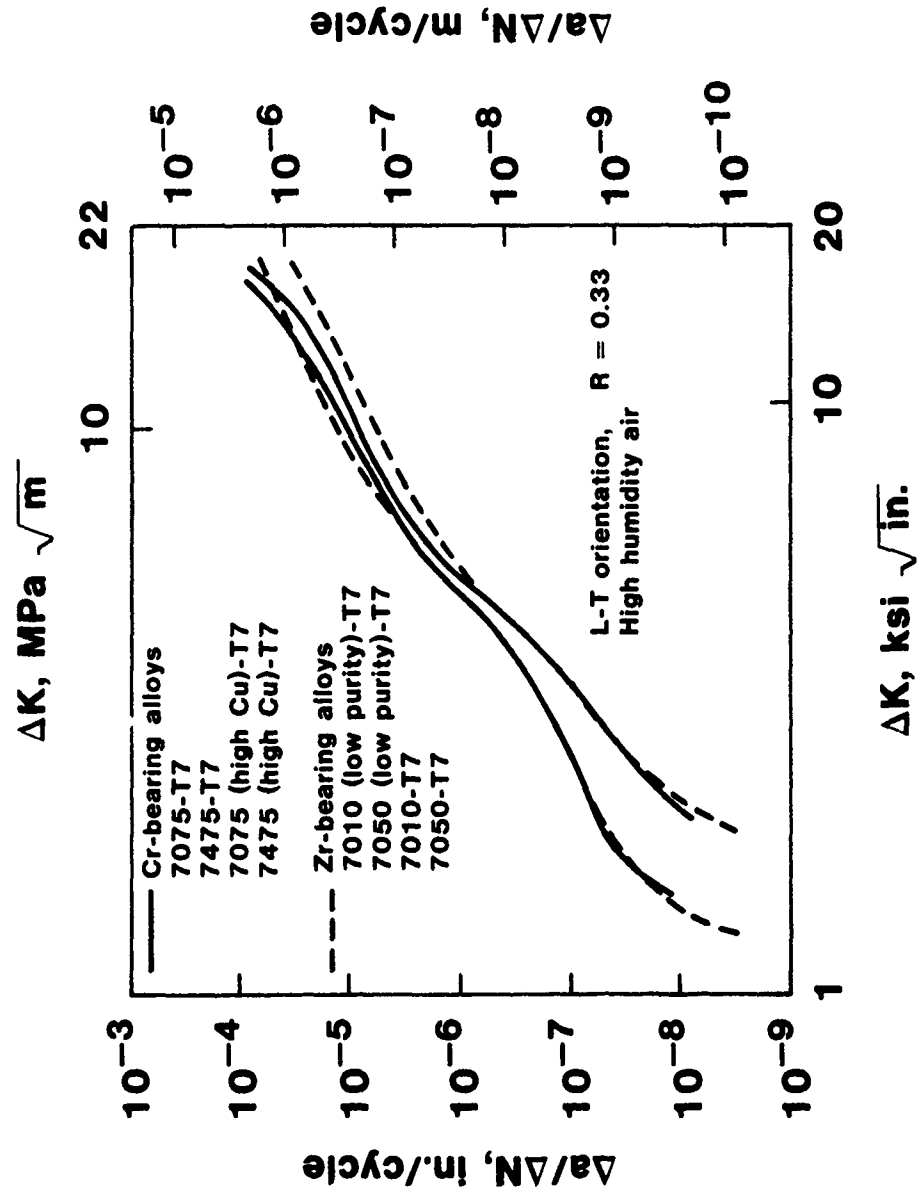


Figure 16. Effect of Chromium (Cr) and Zirconium (Zr) Dispersoids on Constant Amplitude Fatigue Crack Growth of 7XXX-T7 Aluminum Alloys in High Humidity (> 90% R.H.) Air at Room Temperature at an R-Ratio of 0.33.

(a)
7075-T6
 $da/dN = 3.5 \times 10^{-10}$ m/cycle
 $(1.4 \times 10^{-8}$ in./cycle)



←
 Propagation direction

— 50 μm

(b)
7075-T7
 $da/dN = 6.4 \times 10^{-10}$ m/cycle
 $(2.5 \times 10^{-8}$ in./cycle)



**Typical fracture surface appearance of alloys
 7075-T6 and 7075-T7 at $\Delta K = 2.2 \text{ MPa } \sqrt{\text{m}}$
 $(2 \text{ ksi } \sqrt{\text{in.}})$.
 Figure 17.**

GA 12629

$$\Delta K = 1.9 \text{ MPa} \sqrt{\text{m}}$$

(1.7 ksi $\sqrt{\text{in.}}$)

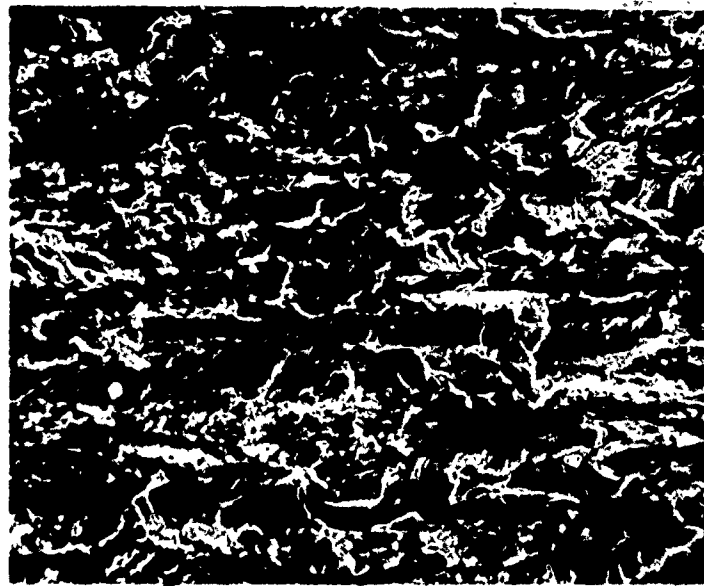


←
Propagation direction

— 28 μm

Typical fracture surface appearance of alloy
7075-T7 at a growth rate of
 3.5×10^{-10} m/cycle (1.4×10^{-8} in./cycle).
Figure 18.

(a)
7075-T6



←
Propagation direction

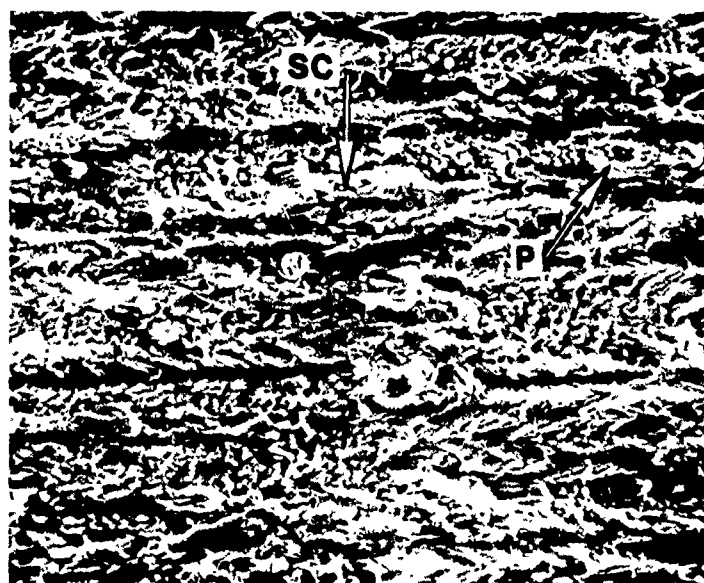
50 μm

(b)
7075-T7



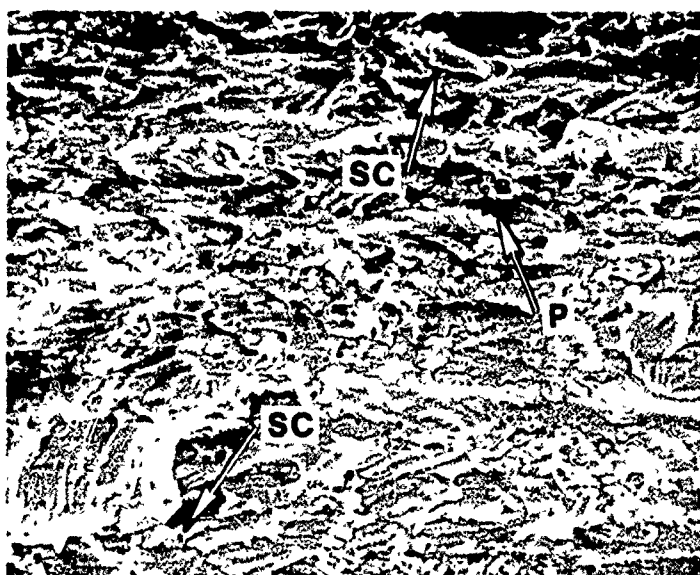
Typical fracture surface appearance of alloys
7075-T6 and 7075-T7 at $\Delta K = 3.3 \text{ MPa } \sqrt{\text{m}}$
(3 ksi $\sqrt{\text{in.}}$).
Figure 19.

(a)
7075-T6



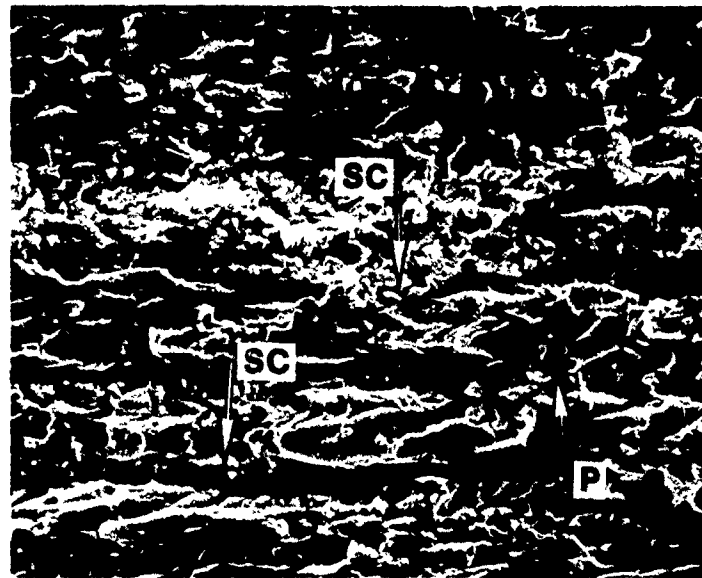
←
Propagation direction

(b)
7075-T7



Typical fracture surface appearance of alloys
7075-T6 and 7075-T7 at $\Delta K = 5.5 \text{ MPa } \sqrt{\text{m}}$
(5 ksi $\sqrt{\text{in.}}$).
Figure 20.

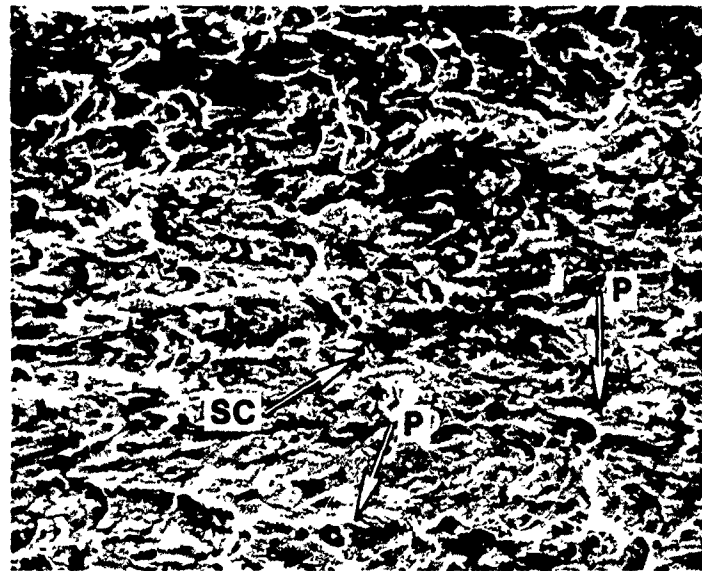
(a)
7075-T6



50 μm

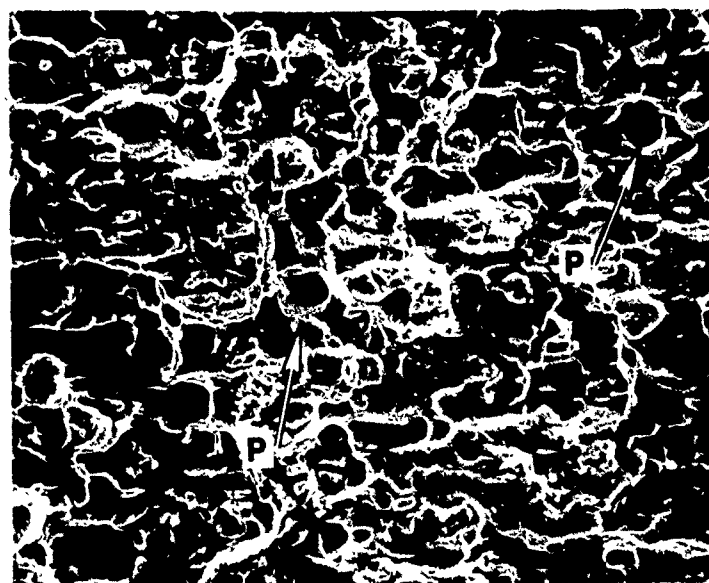
←
Propagation direction

(b)
7075-T7



Typical fracture surface appearance of alloys
7075-T6 and 7075-T7 at $\Delta K = 6.6 \text{ MPa } \sqrt{\text{m}}$
(6 ksi $\sqrt{\text{in.}}$).
Figure 21.

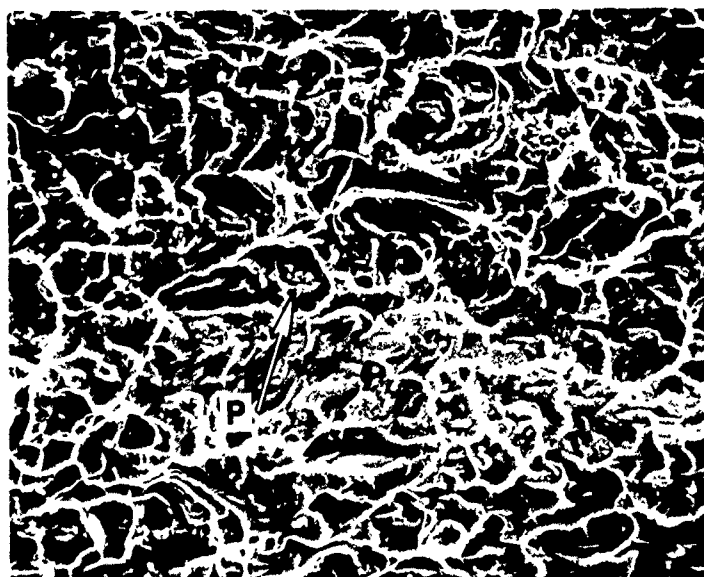
(a)
7075-T6



←
Propagation direction

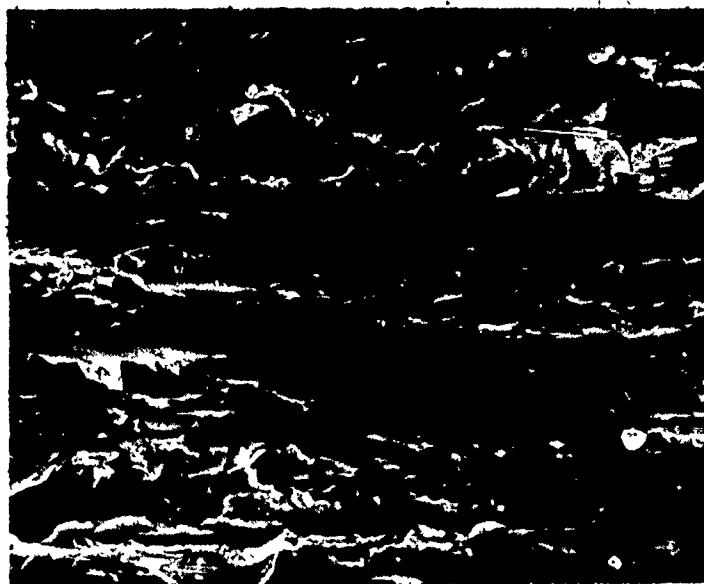
50 μm

(b)
7075-T7



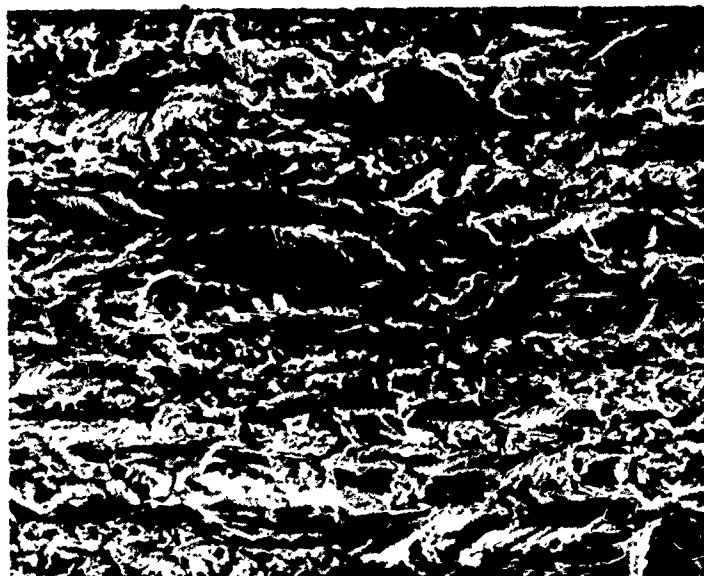
Typical fracture surface appearance of alloys
7075-T6 and 7075-T7 at $\Delta K = 11 \text{ MPa } \sqrt{\text{m}}$
(10 ksi $\sqrt{\text{in.}}$).
Figure 22.

(a)
 $\Delta K = 2.2 \text{ MPa } \sqrt{\text{m}}$
(2 ksi $\sqrt{\text{in.}}$)



←
Propagation direction

(b)
 $\Delta K = 3.3 \text{ MPa } \sqrt{\text{m}}$
(3 ksi $\sqrt{\text{in.}}$)



Typical fracture surface appearance of High Cu
7075-T7 alloy at $\Delta K = 2.2$ and $3.3 \text{ MPa } \sqrt{\text{m}}$
(2 and 3 ksi $\sqrt{\text{in.}}$).

Figure 23.

GA 12629

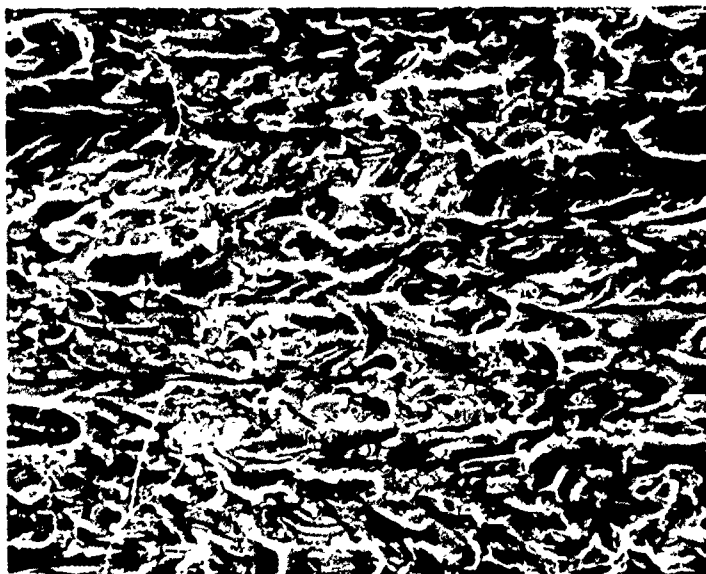
(a)
 $\Delta K = 2.2 \text{ MPa } \sqrt{\text{m}}$
(2 ksi $\sqrt{\text{in.}}$)



←
Propagation direction

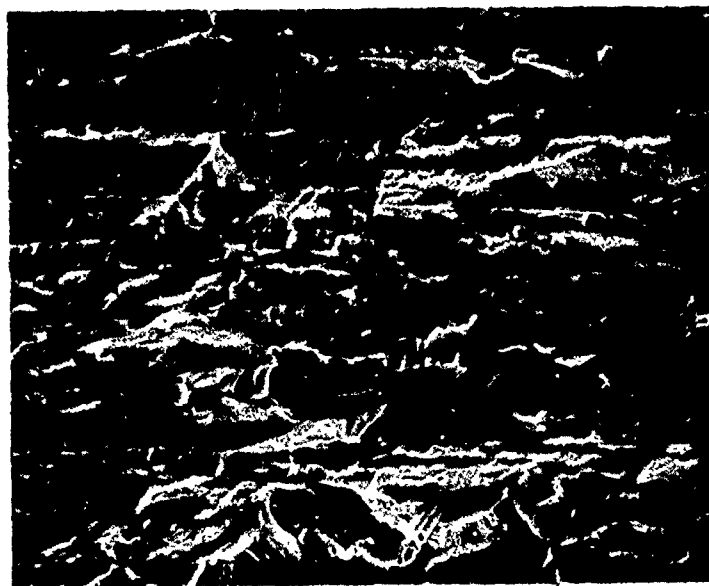
50 μm

(b)
 $\Delta K = 11 \text{ MPa } \sqrt{\text{m}}$
(10 ksi $\sqrt{\text{in.}}$)



Typical fracture surface appearance of alloy
7475-T7 at $\Delta K = 2.2$ and $11 \text{ MPa } \sqrt{\text{m}}$
(2 and 10 ksi $\sqrt{\text{in.}}$).
Figure 24.

(a)
7050-T7



←
Propagation direction

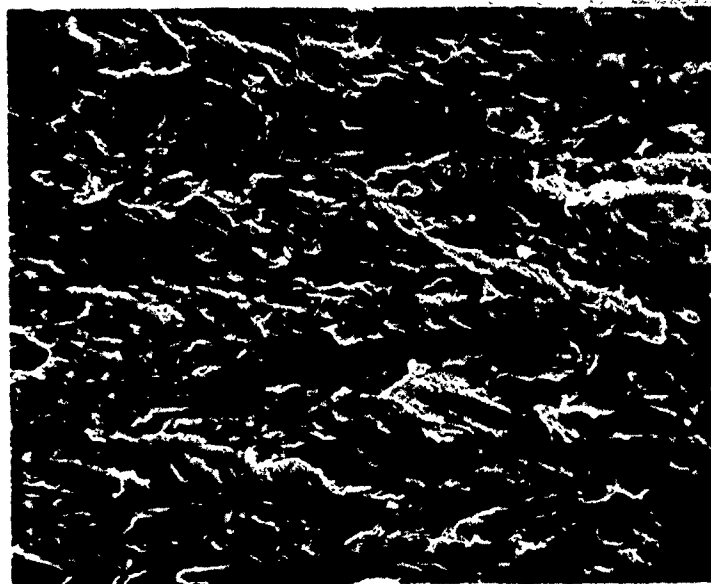
— 50 μm

(b)
Low Purity
7050-T7



Typical fracture surface appearance of alloy
7050-T7 and Low Purity 7050-T7 at
 $\Delta K = 2.2 \text{ MPa } \sqrt{\text{m}}$ (2 ksi $\sqrt{\text{in.}}$).
Figure 25.

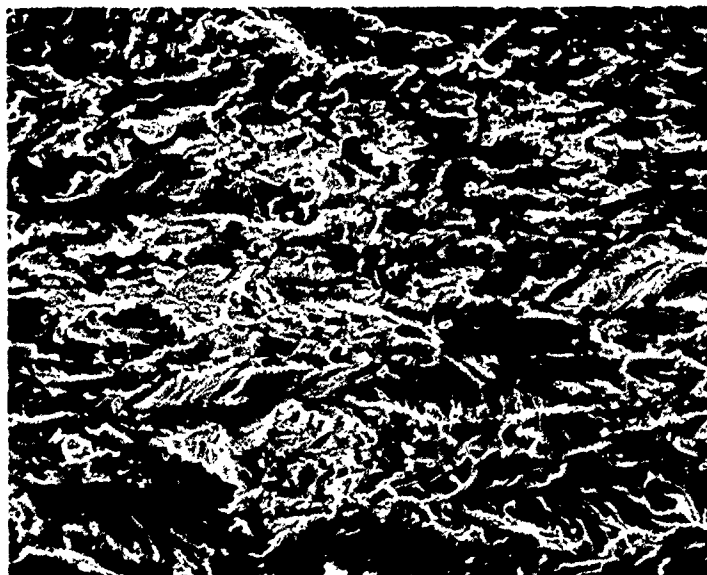
(a)
7050-T7



←
Propagation direction

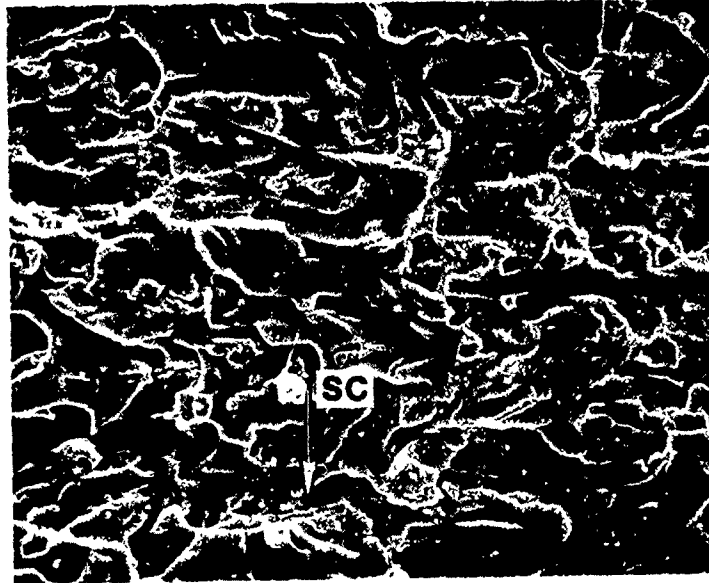
50 μm

(b)
Low Purity
7050-T7



Typical fracture surface appearance of alloys
7050-T7 and Low Purity 7050-T7 at
 $\Delta K = 5.5 \text{ MPa } \sqrt{\text{m}}$ (5 ksi $\sqrt{\text{in.}}$).
Figure 26.

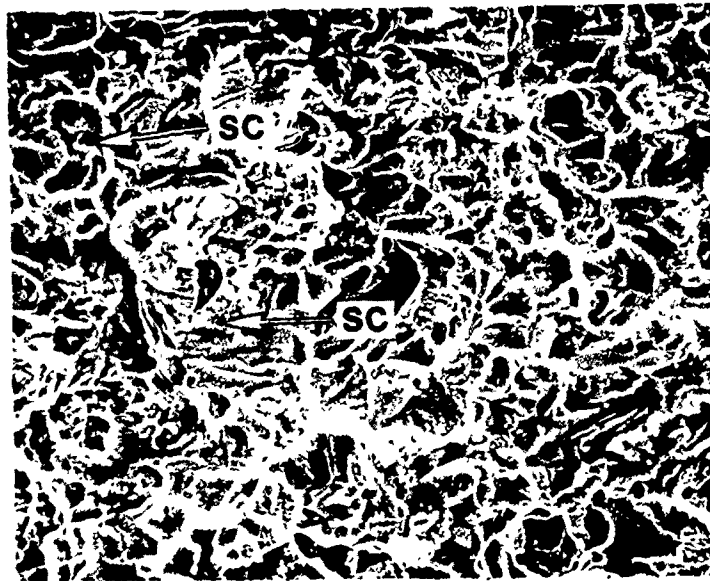
(a)
7050-T7



←
Propagation Direction

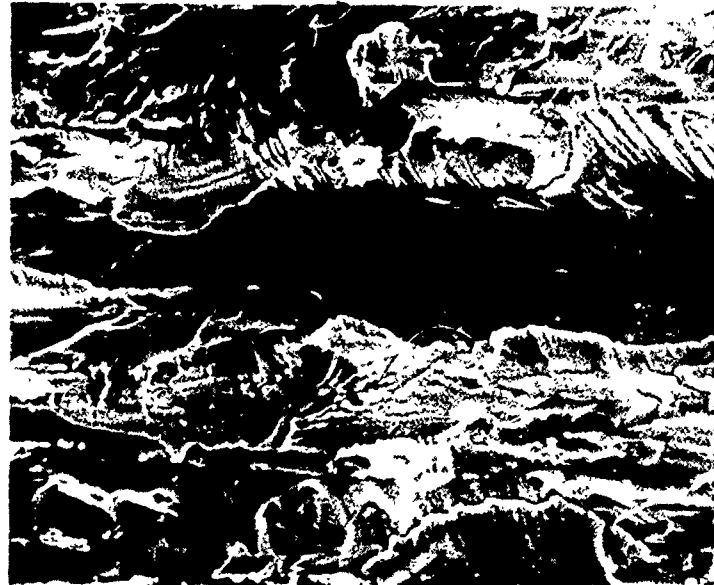
50 μm

(b)
Low Purity
7050-T7



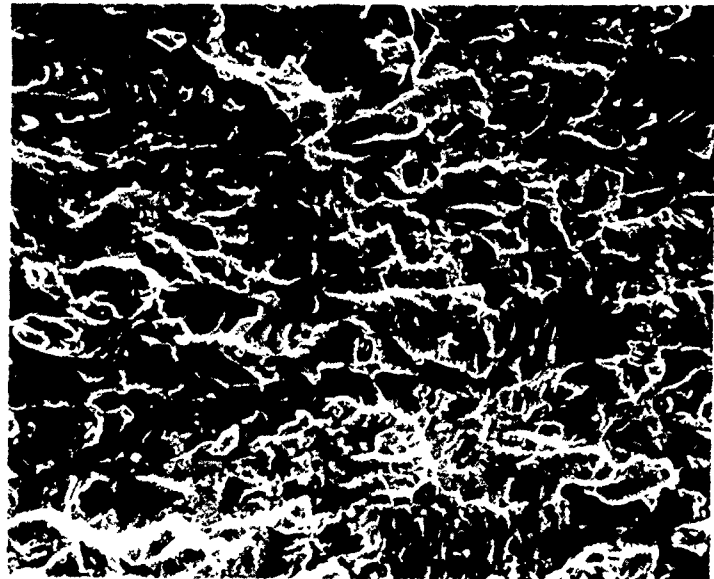
Typical fracture surface appearance of alloys
7050-T7 and Low Purity 7050-T7 at
 $\Delta K = 11 \text{ MPa } \sqrt{\text{m}}$ ($10 \text{ ksi } \sqrt{\text{in.}}$).
Figure 27.

(a)
 $\Delta K = 2.2 \text{ MPa } \sqrt{\text{m}}$
(2 ksi $\sqrt{\text{in.}}$)



←
Propagation direction

(b)
 $\Delta K = 11 \text{ MPa } \sqrt{\text{m}}$
(10 ksi $\sqrt{\text{in.}}$)



Typical fracture surface appearance of Low Purity
7010-T7 alloy at $\Delta K = 2.2$ and $11 \text{ MPa } \sqrt{\text{m}}$
(2 and 10 ksi $\sqrt{\text{in.}}$).

Figure 28.

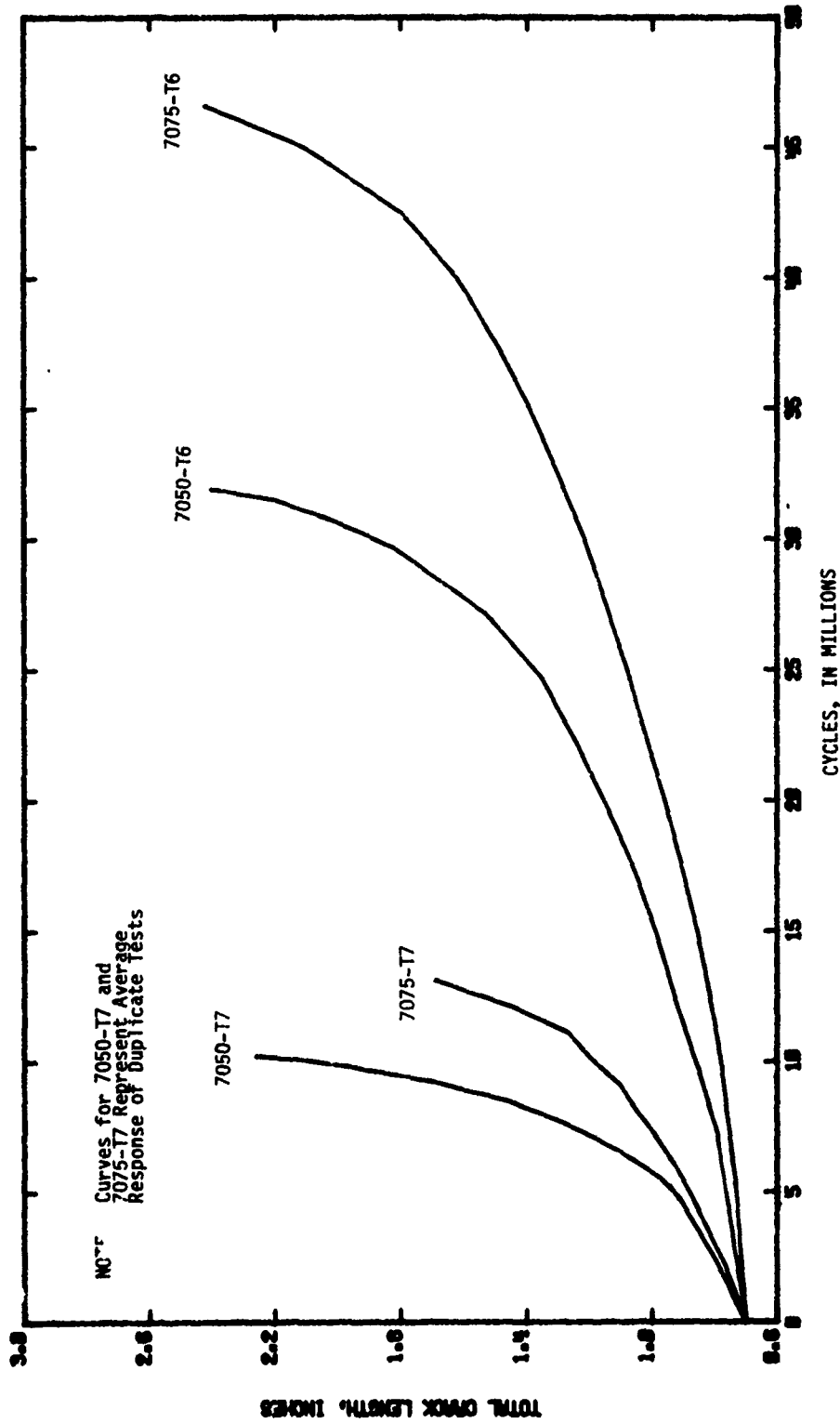


FIGURE 29. CRACK LENGTH VERSUS NUMBER OF CYCLES FOR FOUR 7XXX ALUMINUM ALLOYS, USING AN OLR = 1.8, OCR = 1:8000 SIMPLE OVERLOAD SPECTRUM

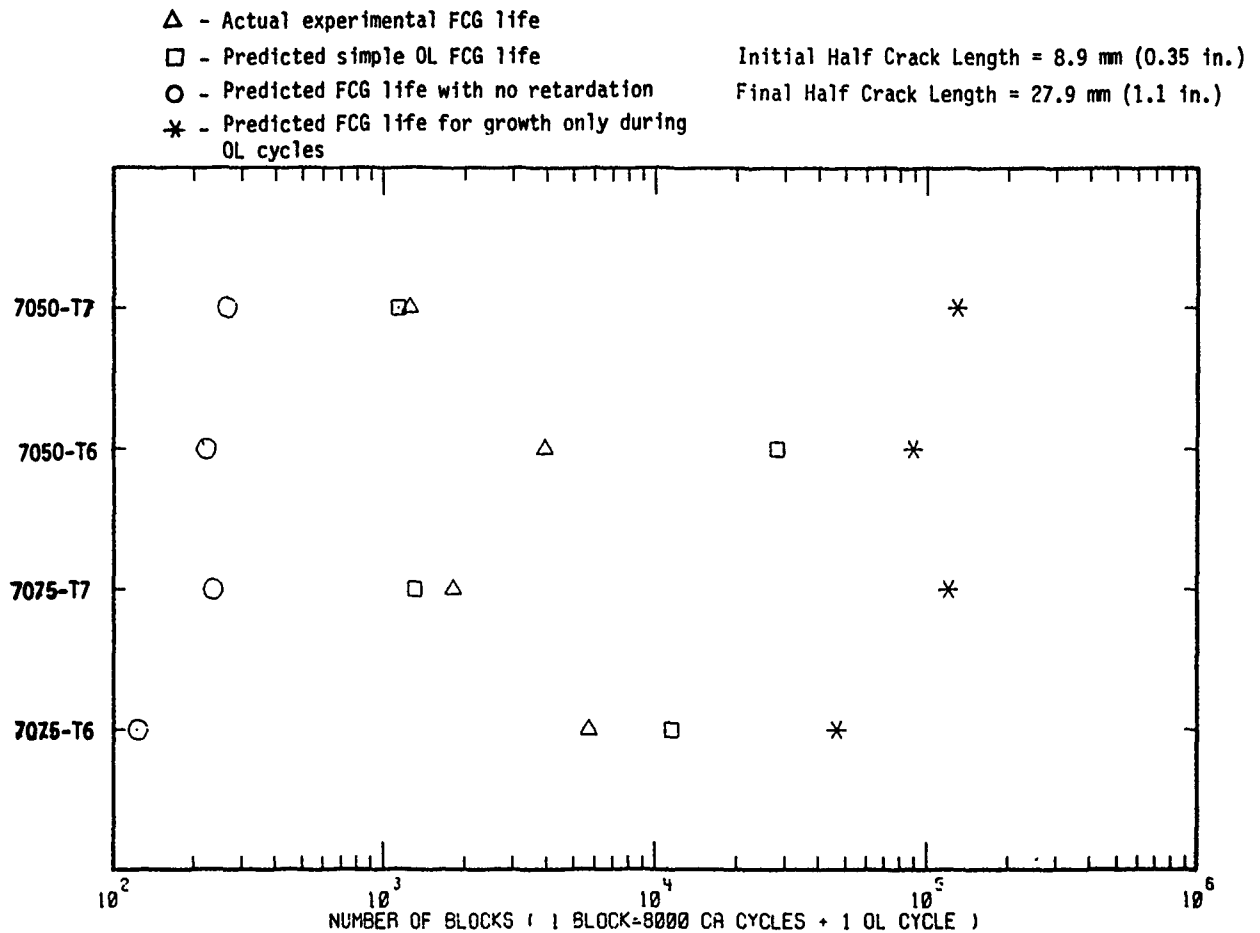


FIGURE 30. COMPARISON OF PREDICTED AND EXPERIMENTAL
 FCG LIVES FOR AN OLR = 1.8, OCR = 1:8000
 SIMPLE OVERLOAD SPECTRUM

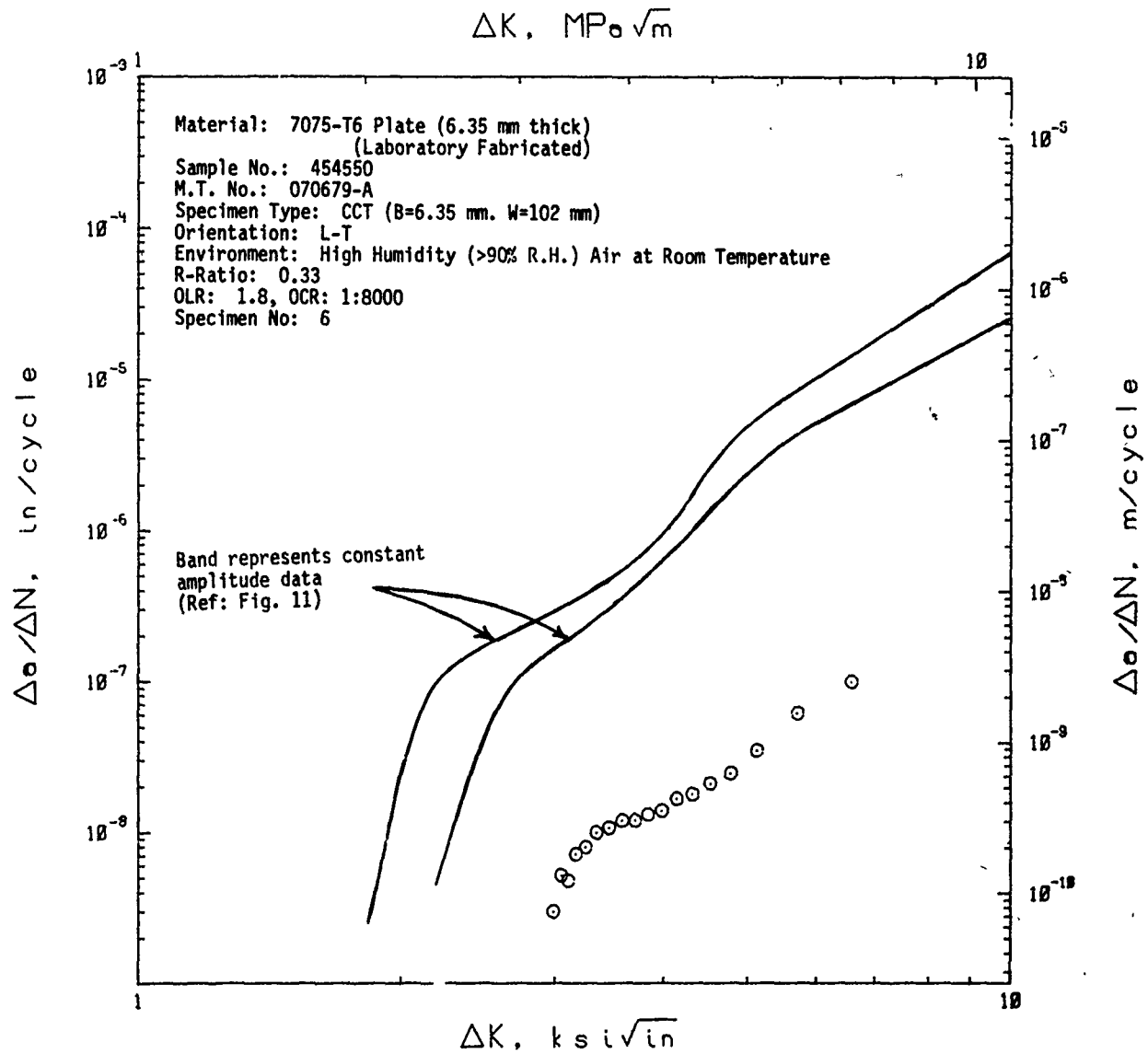


FIGURE 31. CYCLIC STRESS INTENSITY RANGE, ΔK , VERSUS CYCLIC FATIGUE CRACK GROWTH RATE, $\Delta a/\Delta N$, OF 7075-T6 PLATE FOR AN OLR = 1.8, OCR = 1:8000 OVERLOAD SPECTRUM

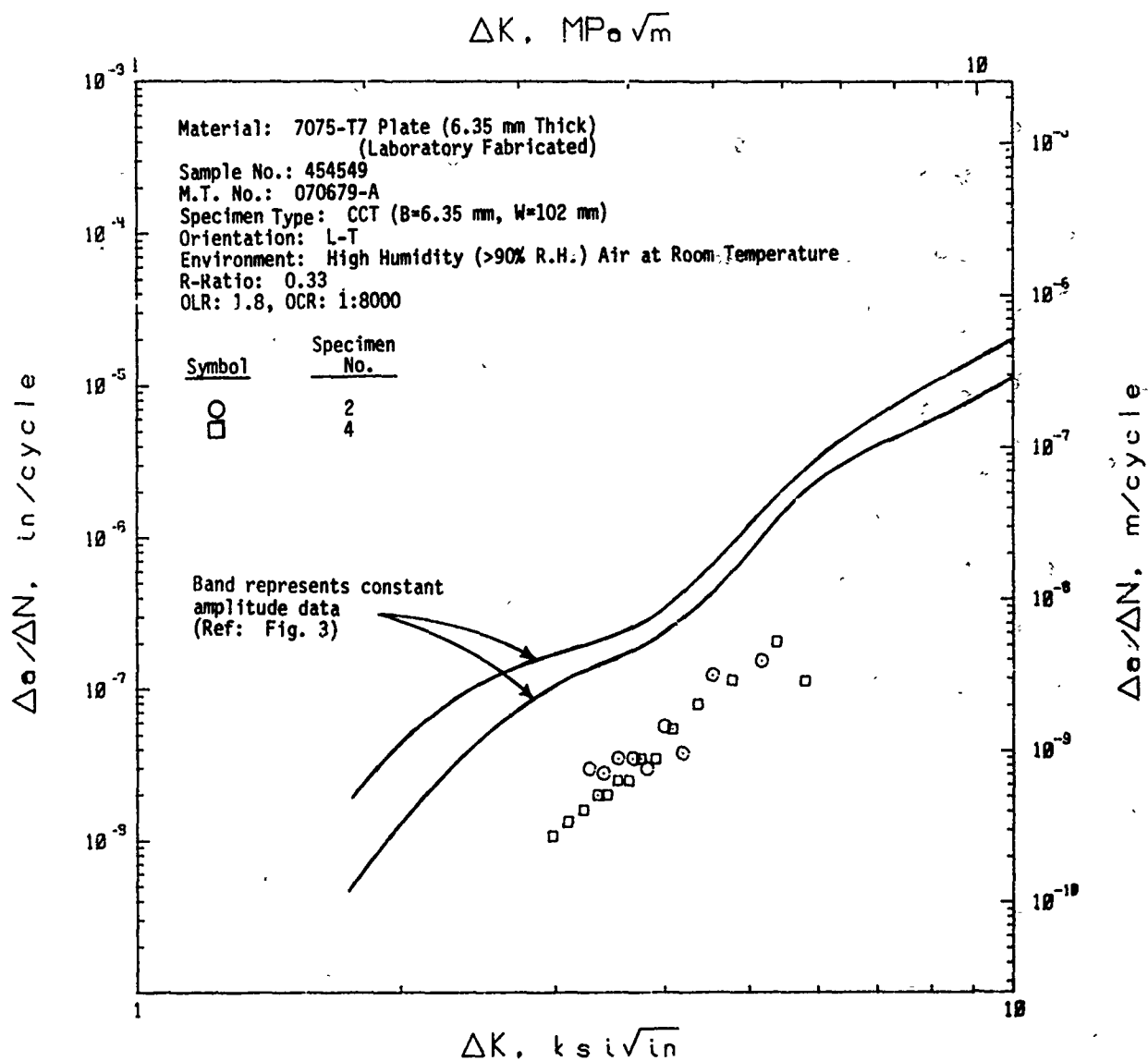


FIGURE 32. CYCLIC STRESS INTENSITY RANGE, ΔK , VERSUS CYCLIC FATIGUE CRACK GROWTH RATE, da/dN , OF 7075-T7 PLATE FOR AN OLR = 1.8, OCR = 1:8000 OVERLOAD SPECTRUM

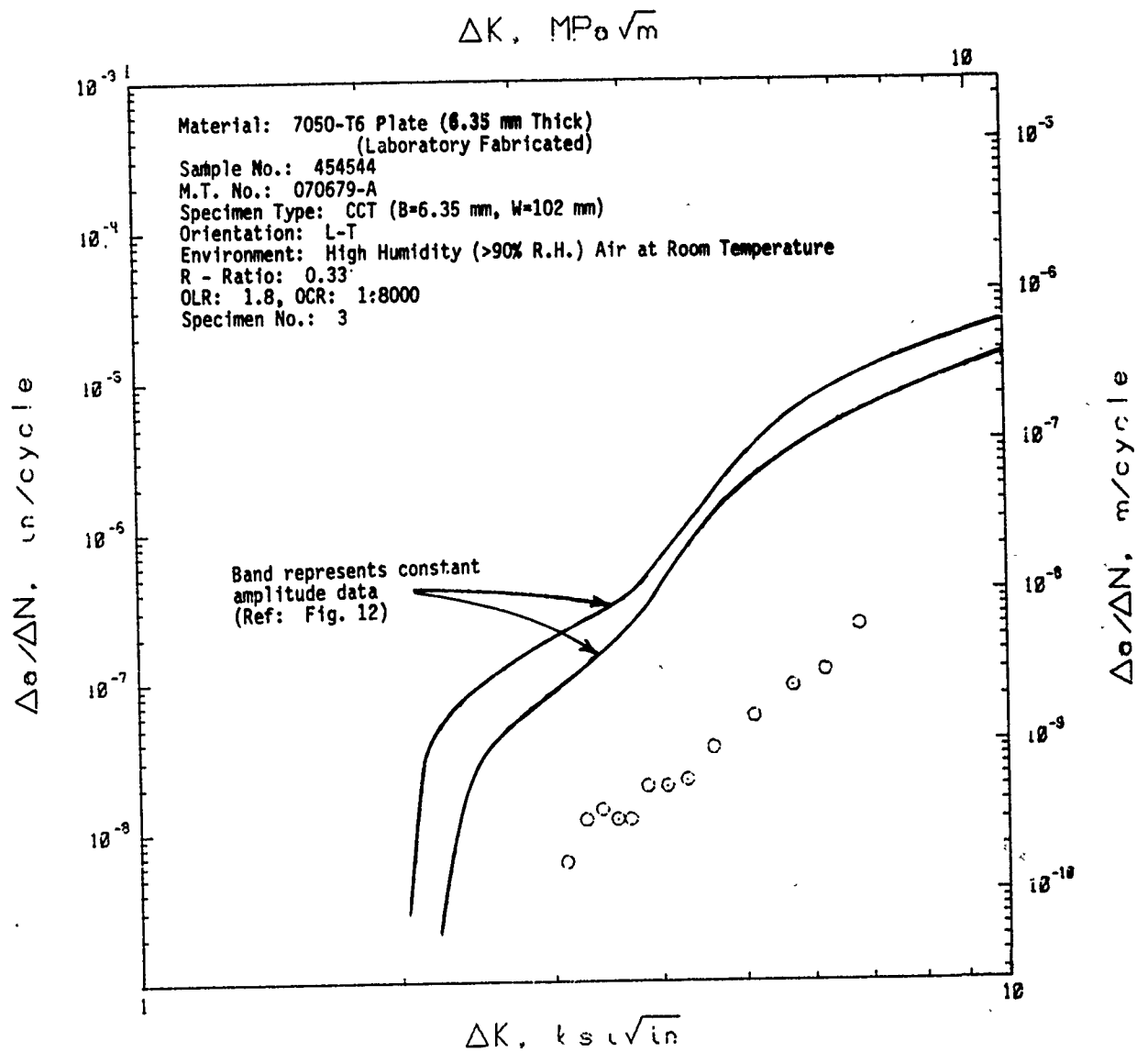


FIGURE 33. CYCLIC STRESS INTENSITY RANGE, ΔK , VERSUS CYCLIC FATIGUE CRACK GROWTH RATE, $\Delta a/\Delta N$, OF 7050-T6 PLATE FOR AN OLR = 1.8, OCR = 1:8000 OVERLOAD SPECTRUM

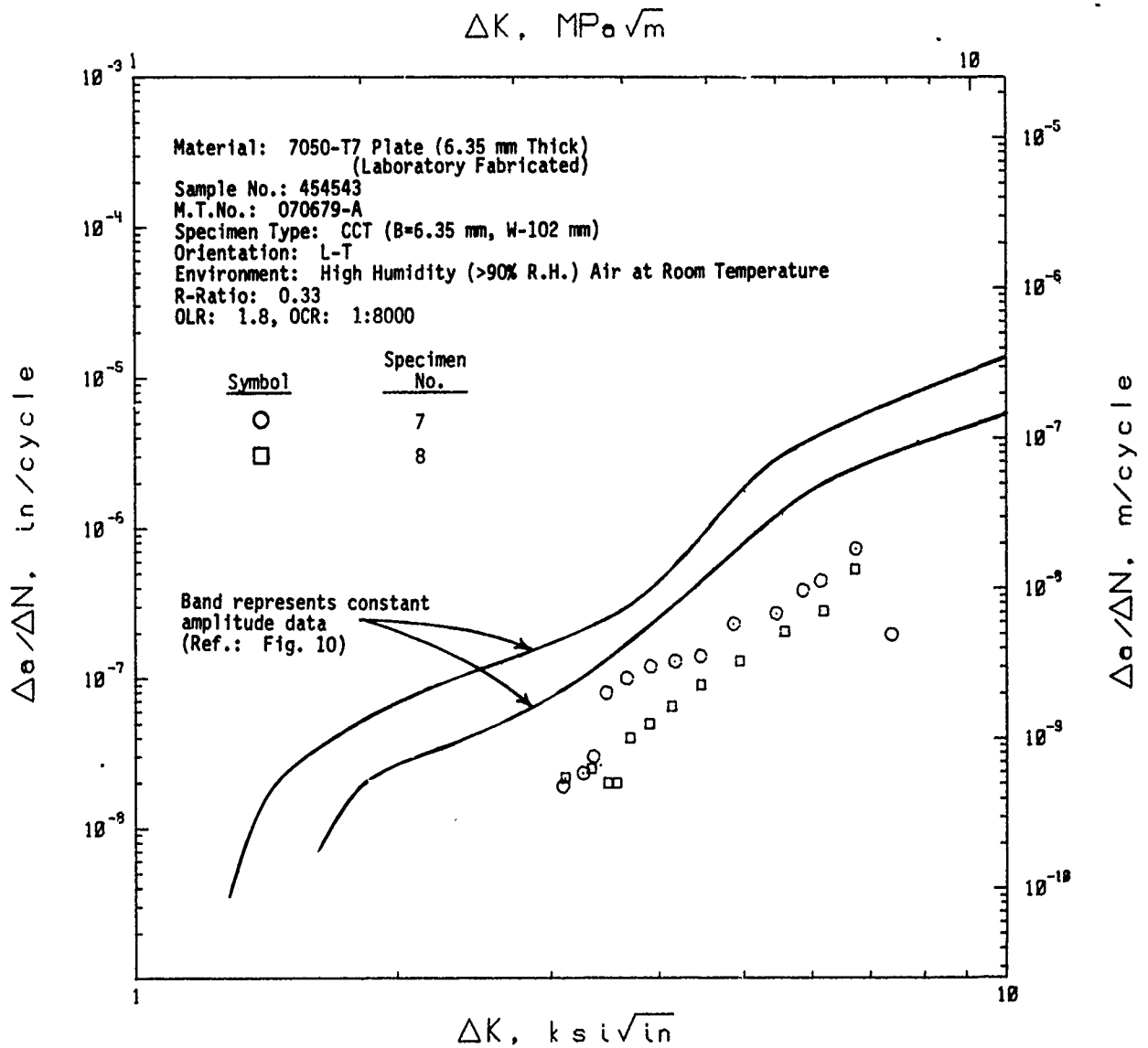


FIGURE 34. CYCLIC STRESS INTENSITY RANGE, ΔK , VERSUS CYCLIC FATIGUE CRACK GROWTH RATE, $\Delta a/\Delta N$, OF 7050-T7 FOR AN OLR = 1.8, OCR = 1:8000 OVERLOAD SPECTRUM

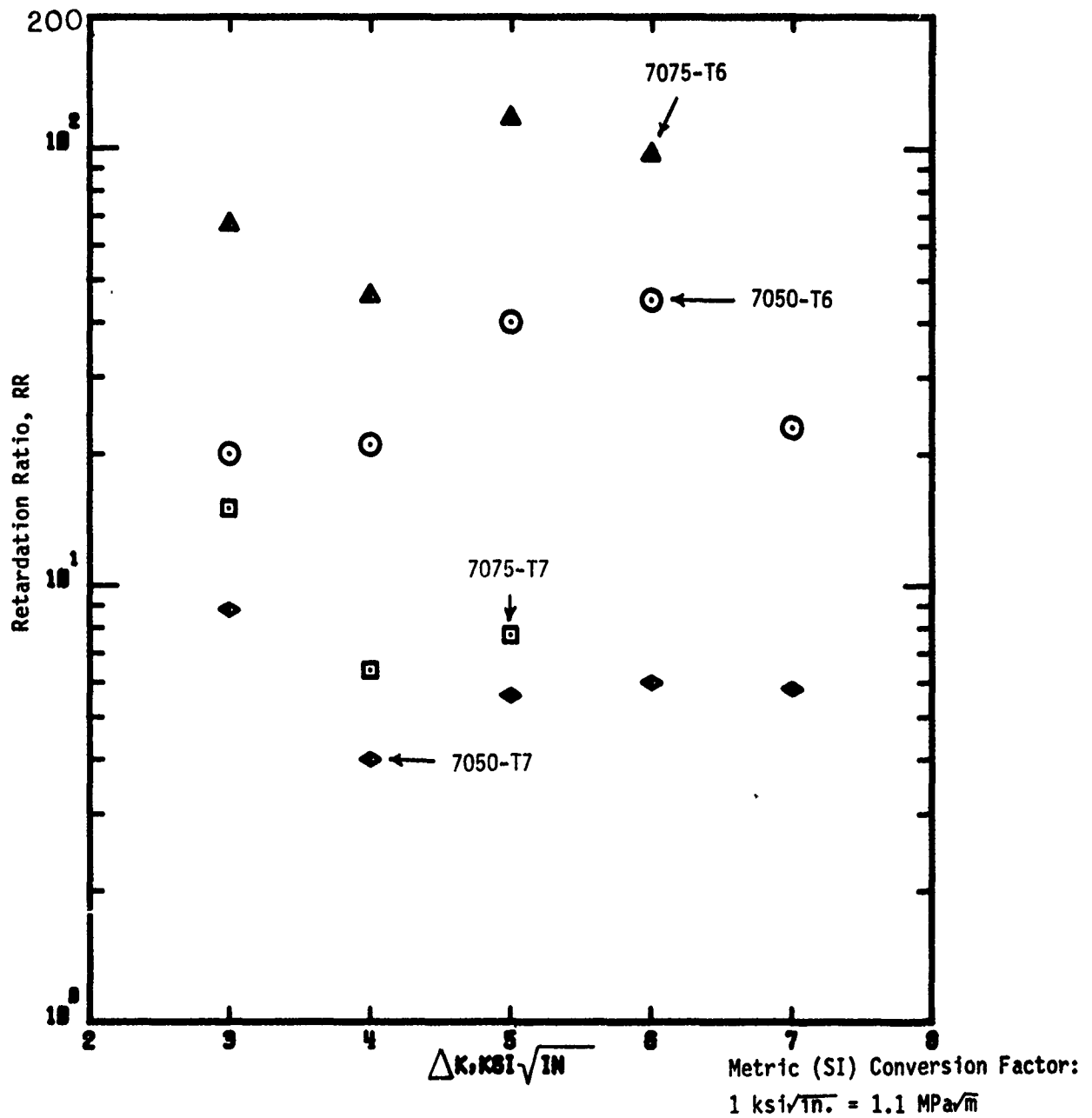
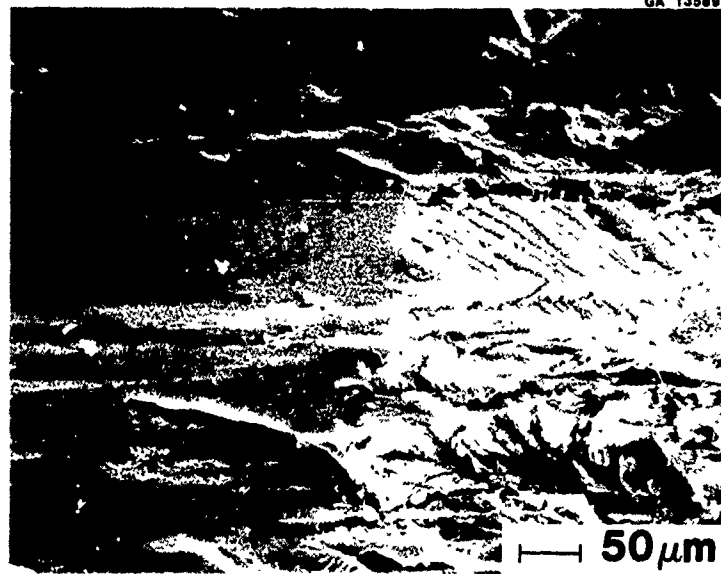


FIGURE 35. RETARDATION RATIO RR, VERSUS CYCLIC STRESS INTENSITY FACTOR, ΔK , FOR FOUR 7XXX ALUMINUM ALLOYS

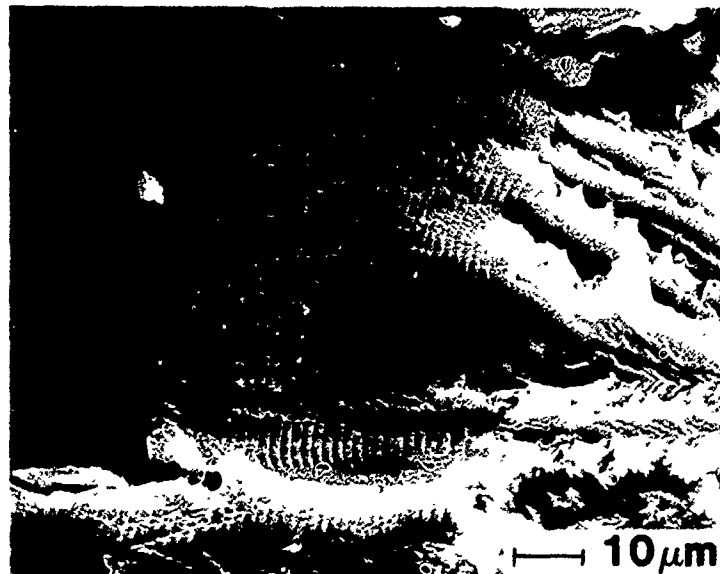
(a)



overload / constant
amplitude

←
Propagation direction /

(b)

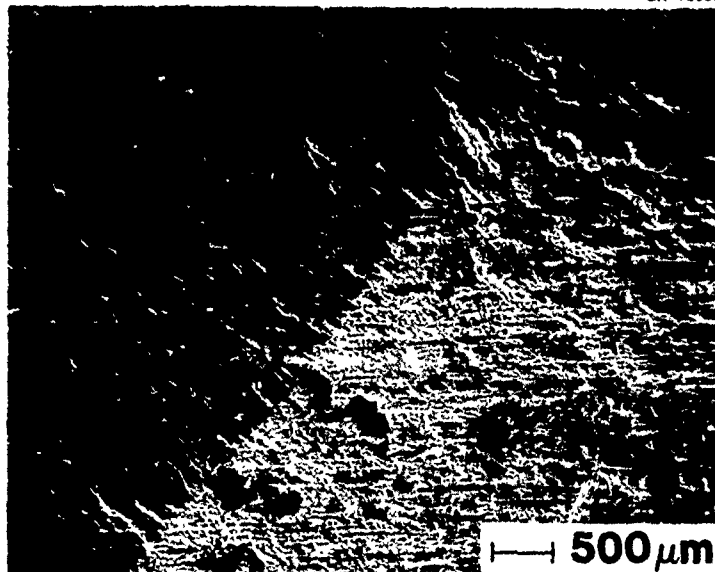


overload/constant amplitude

**Fracture surface appearance of 7050-T7 in
the transition region from CA to a simple
OL spectrum**

Figure 36

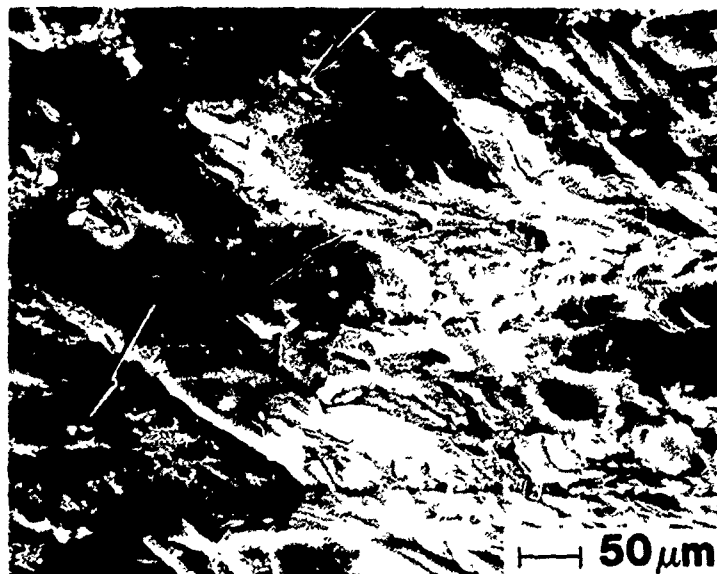
(a)



overload / constant amplitude

←
Propagation direction /

(b)

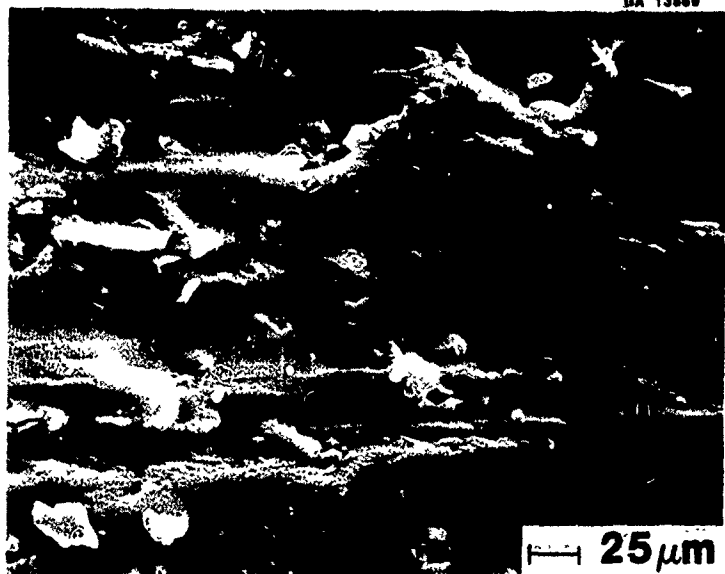


overload / constant amplitude

**Fracture surface appearance of 7075-T/7
in the transition region from CA to a simple
OL spectrum.**

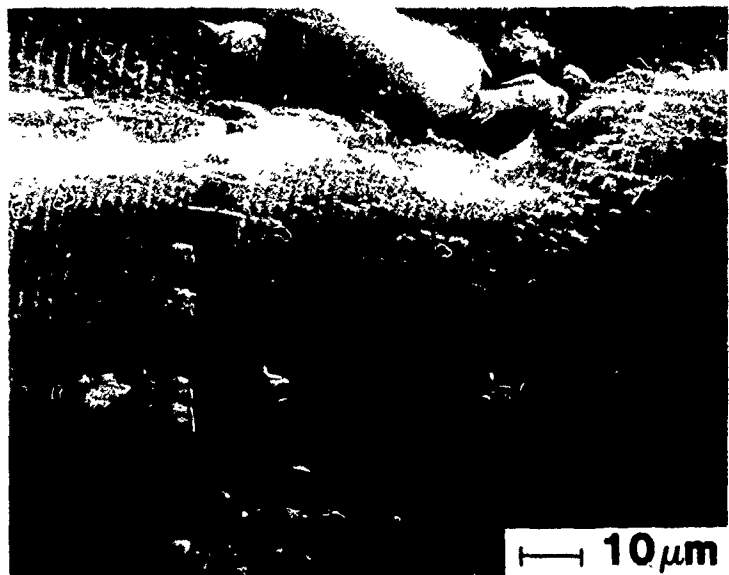
Figure 37

(a)
 1.3×10^{-10} m/cycle
(5×10^{-9} in/cycle)



←
Propagation direction

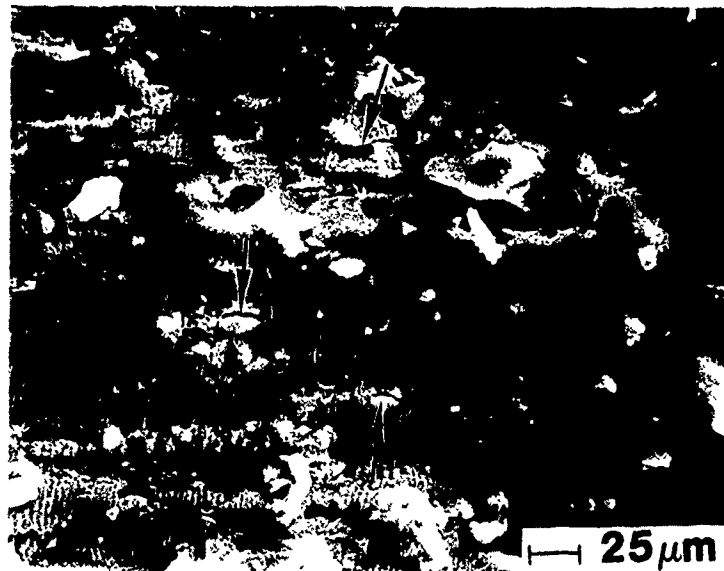
(b)
 1.3×10^{-10} m/cycle
(5×10^{-9} in/cycle)



**Variation in simple OL fracture surface
lineage spacing with crack growth rate in
7075-T6**

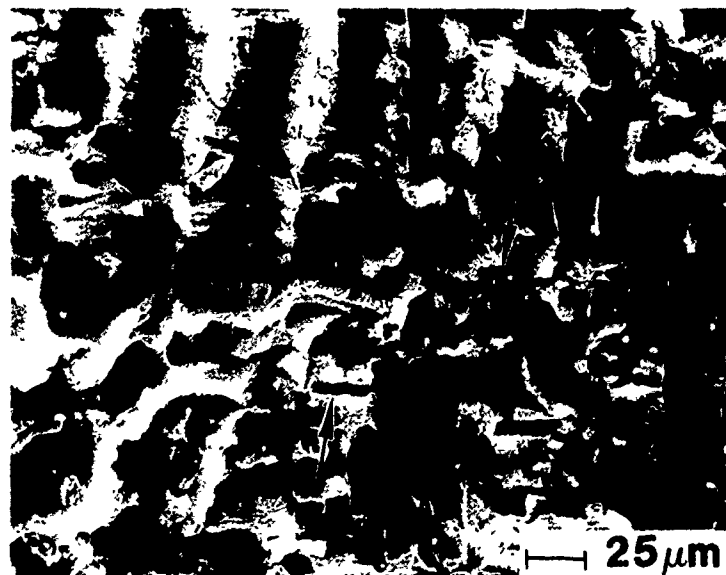
Figure 38

(c)
 2.5×10^{-10} m/cycle
(1×10^{-8} in/cycle)



←
Propagation direction

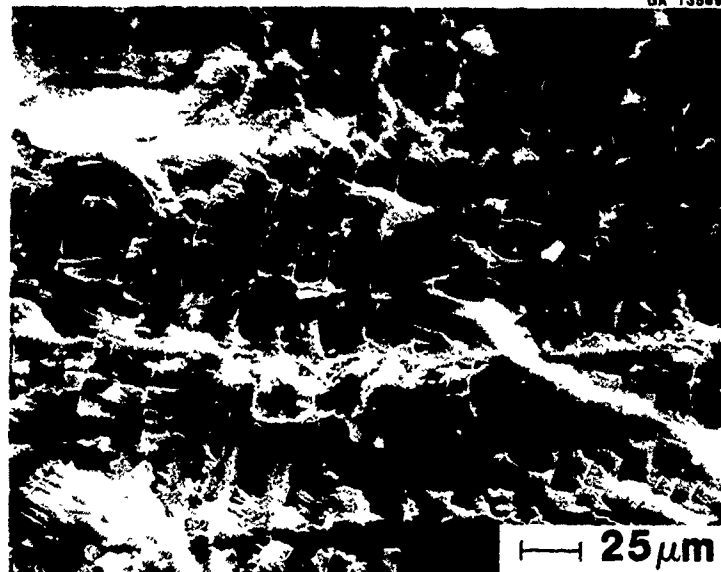
(d)
 2.5×10^{-9} m/cycle
(1×10^{-7} in/cycle)



**Variation in simple OL fracture surface
lineage spacing with crack growth rate in
7075-T6 (continued)**

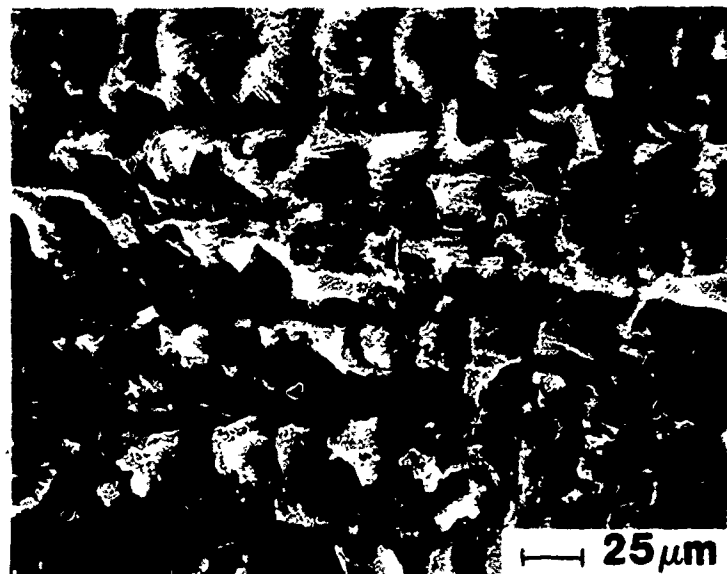
Figure 38

(a)
 2.5×10^{-10} m/cycle
(1×10^{-8} in/cycle)



←
Propagation direction

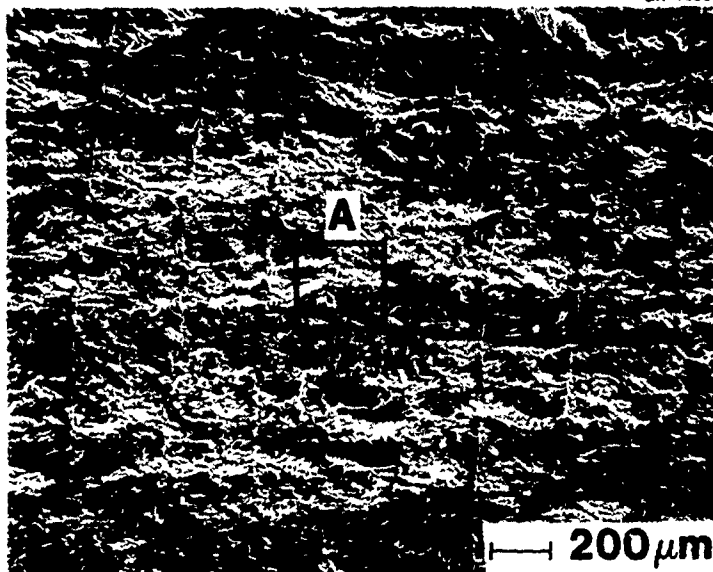
(b)
 2.5×10^{-9} m/cycle
(1×10^{-7} in/cycle)



**Variation in simple OL fracture surface
lineage spacing with crack growth rate in
7050-T7**

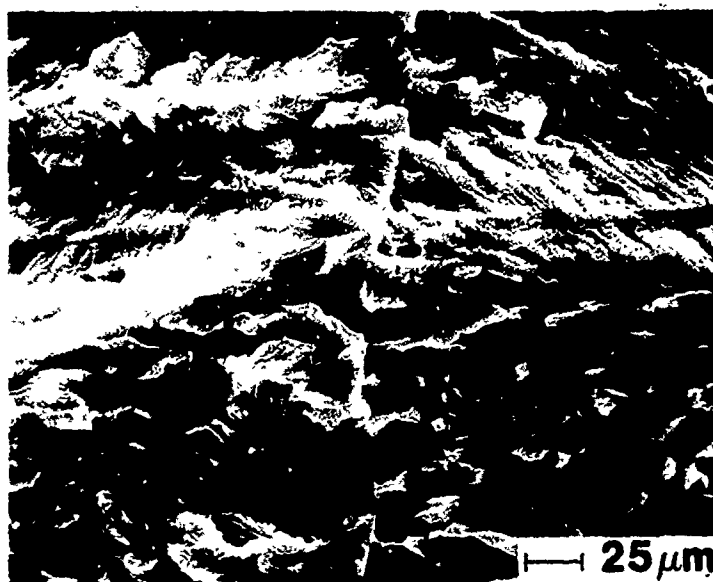
Figure 39

(c)
 2.5×10^{-8} m/cycle
(1×10^{-6} in/cycle)



←
Propagation direction

(d)
Magnified area A
from above figure.



**Variation in simple OL fracture surface
lineage spacing with crack growth rate in
7050-T7 (continued)**

Figure 39

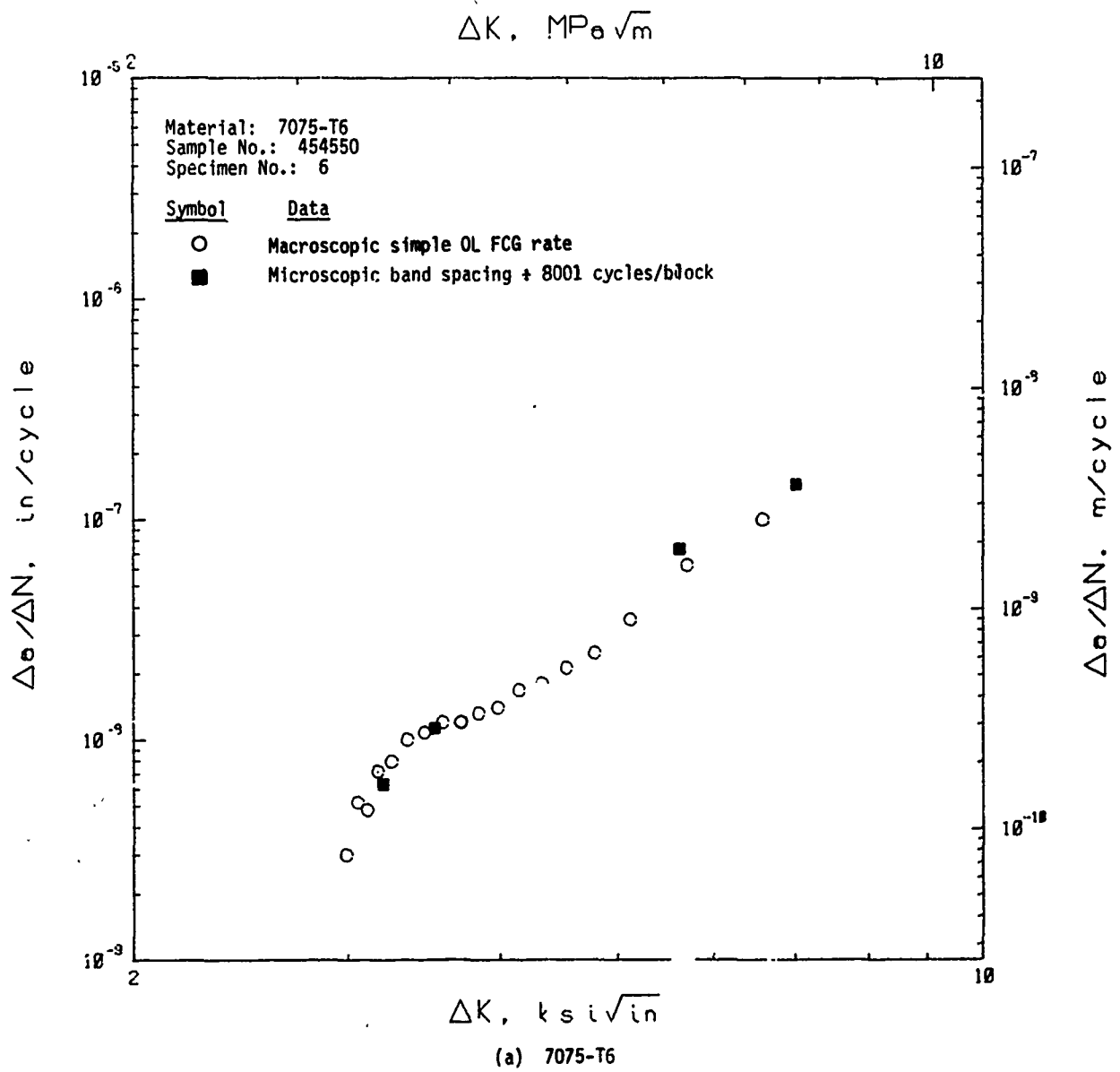


FIGURE 40. CORRELATION BETWEEN MACROSCOPIC AND MICROSCOPIC FATIGUE CRACK GROWTH RATES FOR 7XXX ALUMINUM ALLOYS

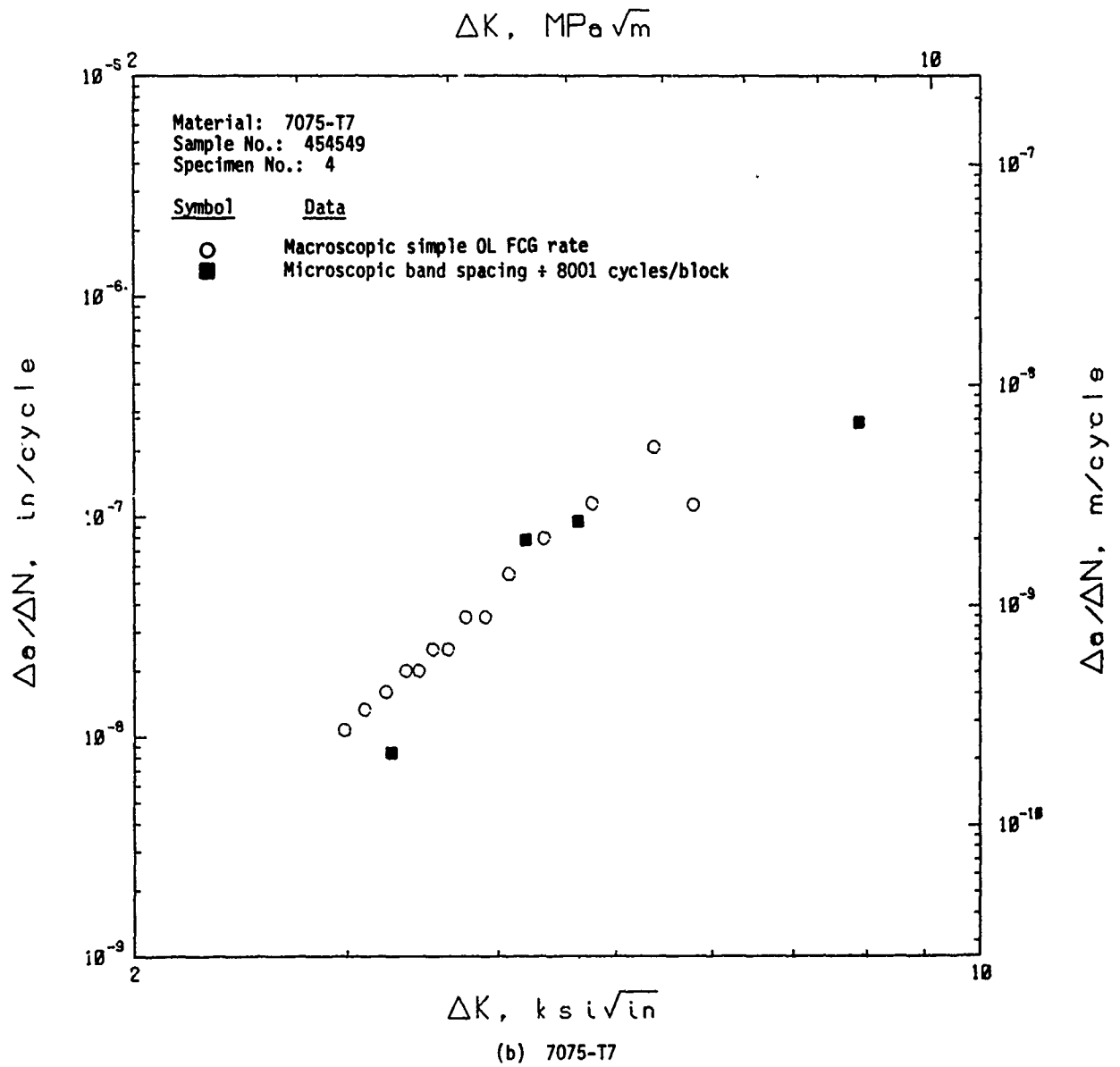


FIGURE 40. (CONTINUED)

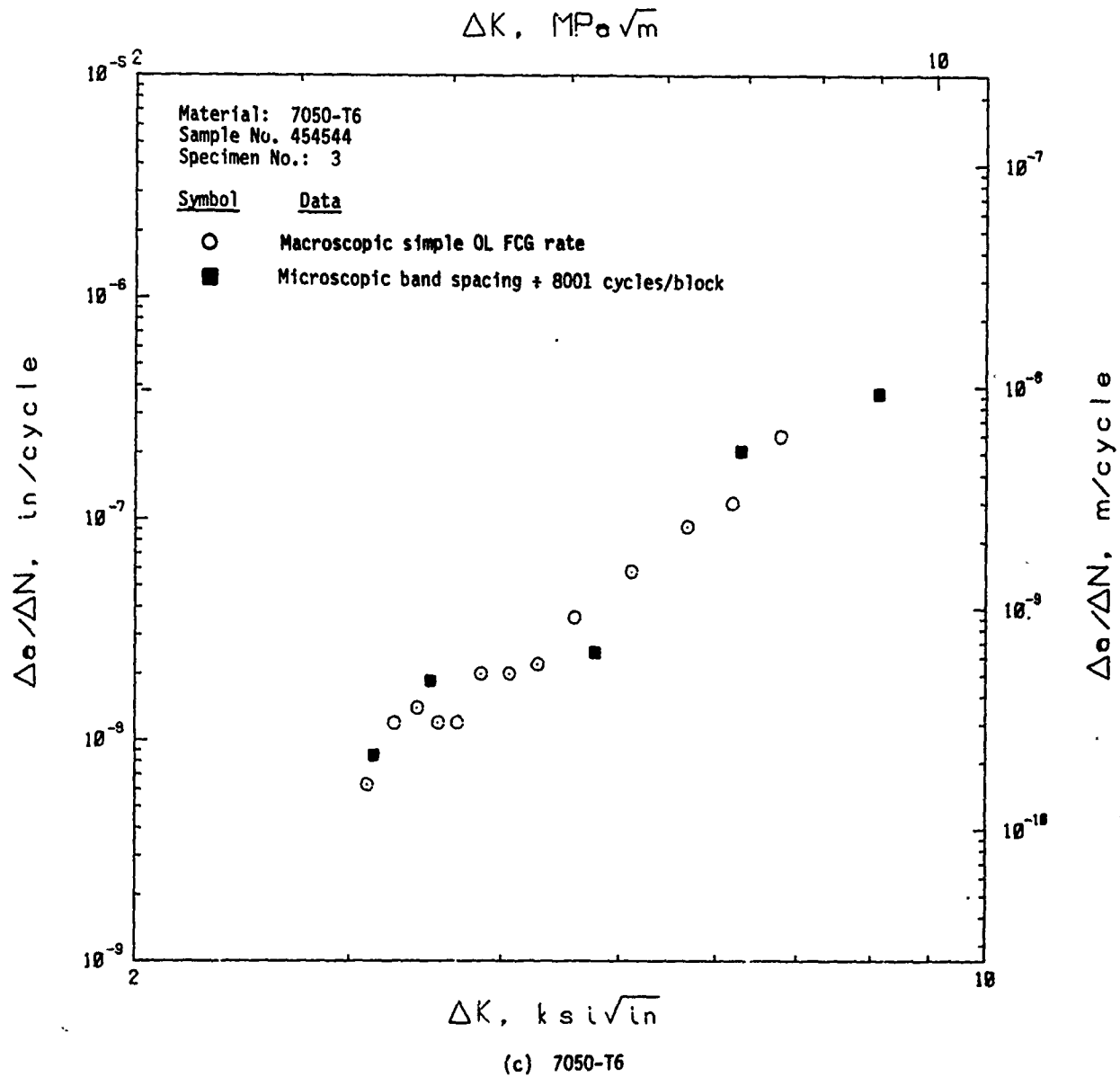
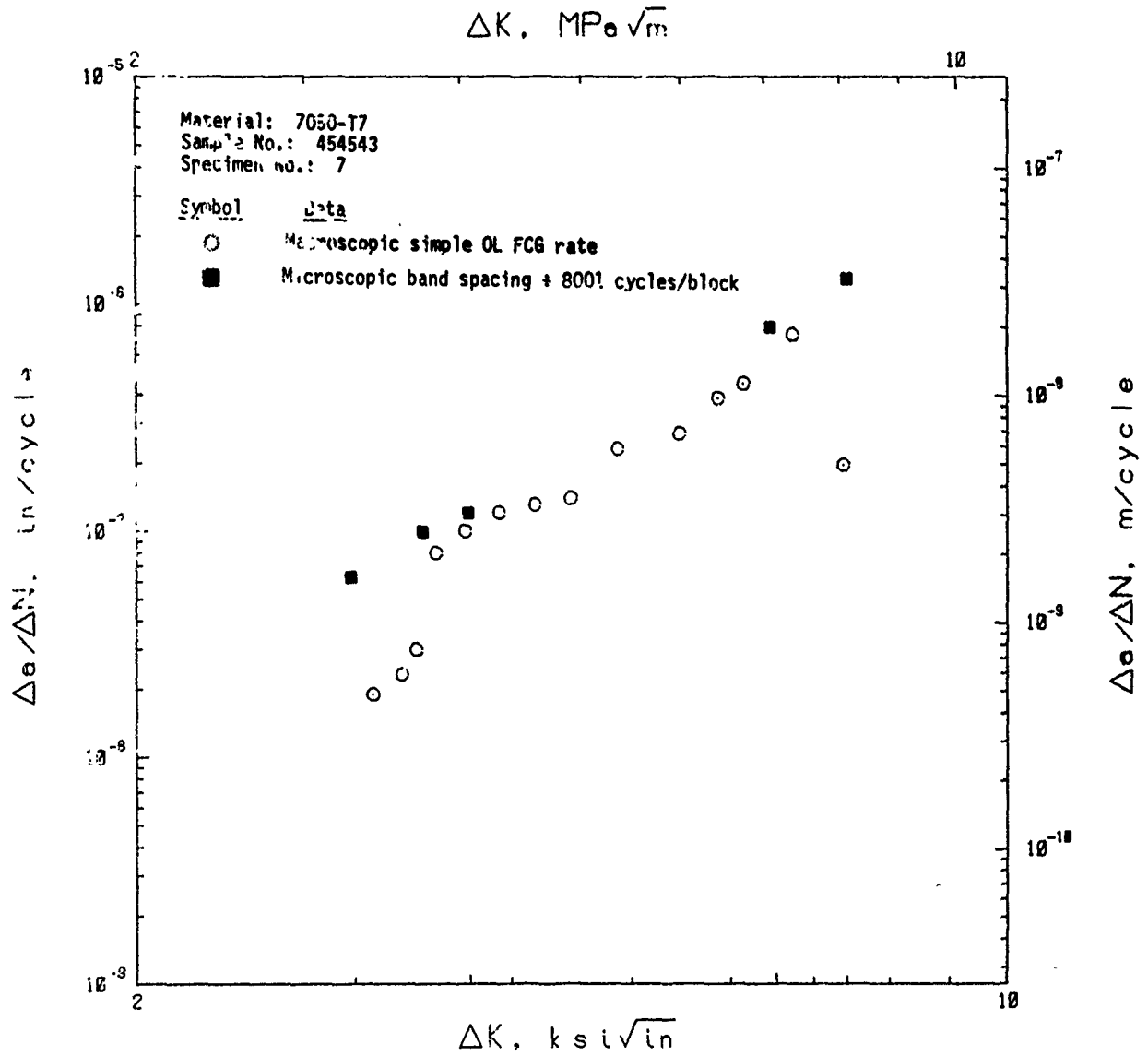


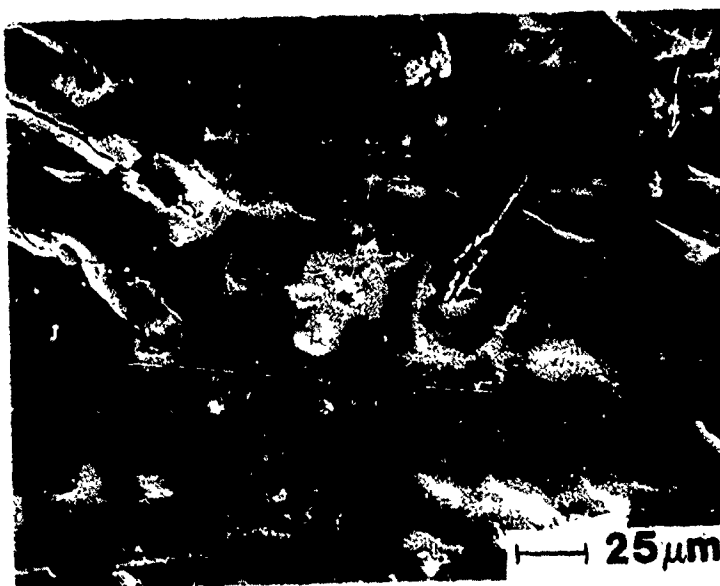
FIGURE 40. (CONTINUED)



(d) 7050-T7

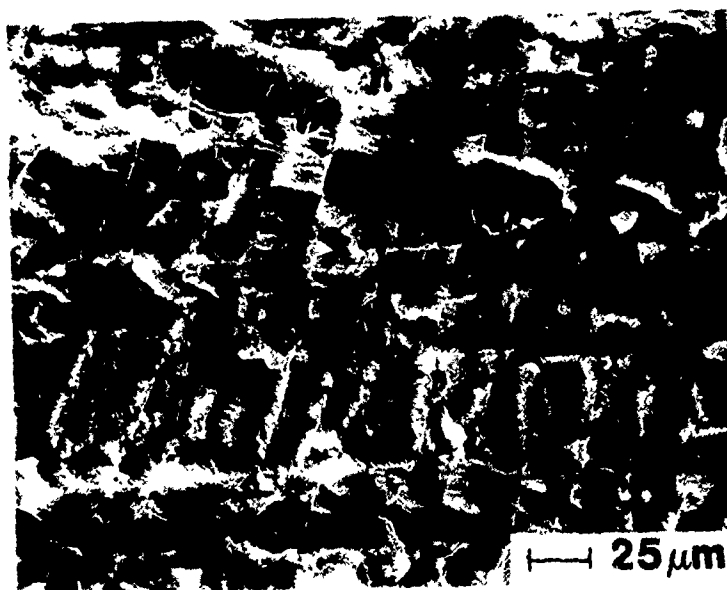
FIGURE 40. (CONTINUED)

(a)
 2.5×10^{-10} m/cycle
(1×10^{-8} in/cycle)



←
Propagation direction

(b)
 2.5×10^{-9} m/cycle
(1×10^{-7} in/cycle)



**Fracture surface appearance of 7075-T7
for a simple OL spectrum**

Figure 41

Two Stage Process of Variable-Load Amplitude Fatigue Crack Growth Resistance of 7XXX-Type Aluminum Alloys

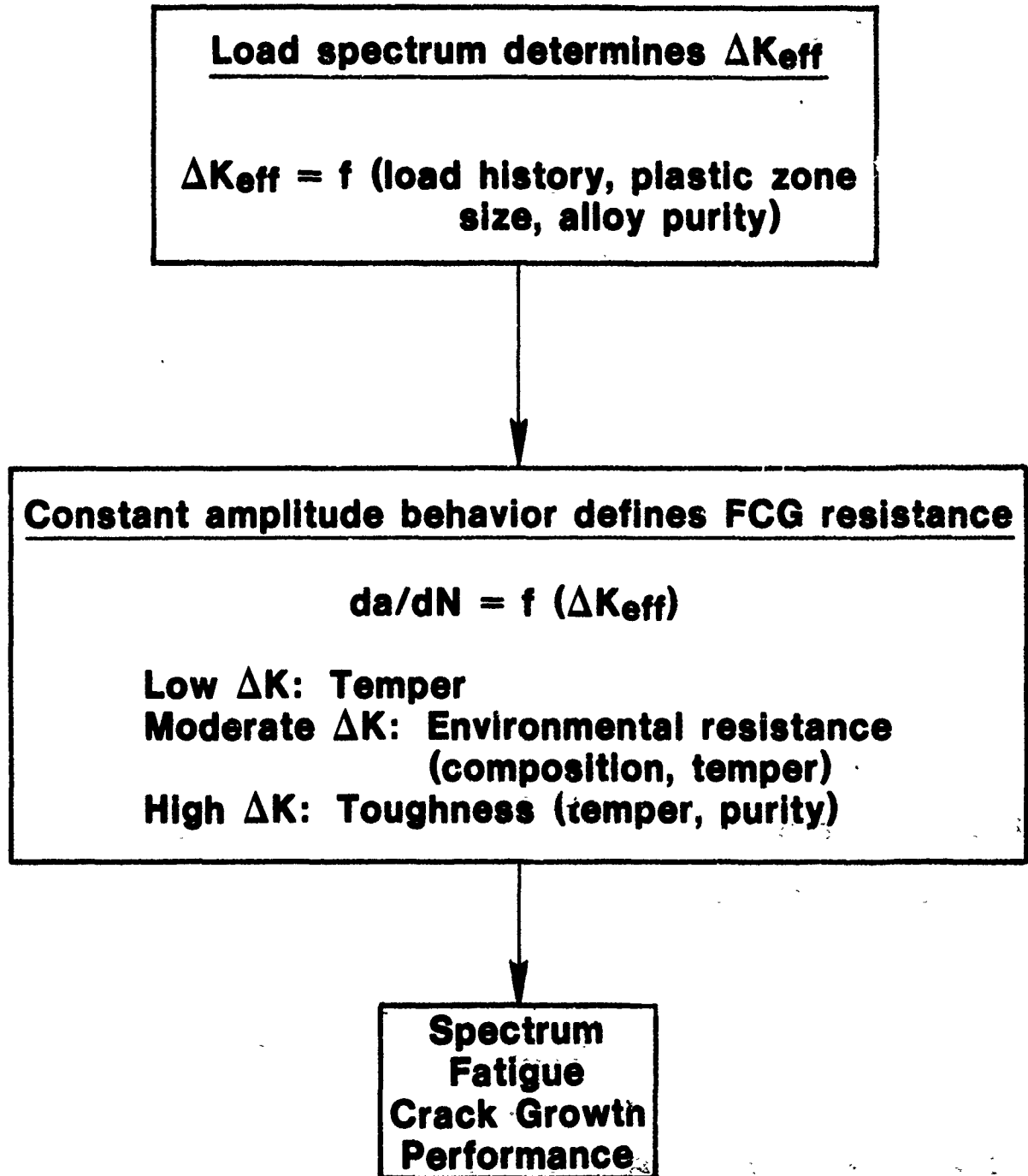


FIGURE 42. SCHEMATIC DIAGRAM SHOWING THE INFLUENCE OF METALLURGICAL VARIANTS ON BOTH RETARDATION AND FATIGUE CRACK GROWTH DURING SPECTRUM FATIGUE LOADING

ATTACHMENT (1)
DISTRIBUTION LIST

Page 1

Department of the Navy
Naval Air Systems Command
Washington, D.C. 20361
Attn: Mr. Michael D. Valentine
AIR-5163C4 (10 copies)
Mr. R. Schmidt
AIR- 320A

Department of the Navy
Sea Systems Command
Washington, D.C. 20361
Attn: Code 03423

Chief of Naval Research
Department of the Navy
Washington, D.C. 20361
Attn: ONR 423, 471, (2 copies)

Commander
U.S. Naval Research Laboratory
Washington, D.C. 20390
Attn: Dr. Ray Hettche
Dr. B.B. Rath
Dr. George Yoder

Commanding Officer
Naval Air Development Center,
Johnsville
Aero Materials Laboratory
Warminster, Pennsylvania 18974
Attn: Mr. F.S. Williams

Naval Material Industrial Resources
Office
Philadelphia, PA 19112

Air Force Materials Laboratory
Wright-Patterson Air Force Base
Dayton, Ohio 45433
Attn: Mr. A. M. Adair (LLM);
Dr. H. Lipsett (LLS);
Dr. F. H. Froes

Army Research Office
Box CM, Duke Station
Durham, North Carolina 27706
Attn: Metallurgy and Ceramics Division

United Aircraft Corporation
Sikorsky Aircraft Division
Stratford, CT 06497

Bell Helicopter Company
P. O. Box 482
Fort Worth, TX 76101

National Academy of Sciences
National Materials Advisory Board
2101 Constitution Avenue
Washington, D.C. 20418
Attn: Dr. J.C. Lane

National Aeronautic and Space
Administration
600 Independence Avenue
Washington, D.C. 20546

U.S. Army Materials & Mechanics
Research Center
Watertown Arsenal
Watertown, Massachusetts 02172
Attn: Dr. Saul Isserow

Titanium Metals Corp of America
Attn: Mr. Larry Mayer
400 Rouser Road
P. O. Box 2824
Pittsburgh, PA 15230

Battelle Memorial Institute
Defense Metals Information Center
505 King Avenue
Columbus, Ohio 43201
Attn: Mr. Richard Wood

Avco Space Systems Division
Lowell Industrial Park
Lowell, Massachusetts 01851

Brush Wellman, Inc.
17876 St. Clair Avenue
Cleveland, Ohio 44110

NASA/Langley
Attn: Mr. Tom Bales
Manufacturing Technology Section
Hampton, VA 23365

The Boeing Company
Aerospace Division
P.O. Box 3707, M/S 73-43
Seattle, Washington 98124
Attn: Mr. Rod Boyer

McDonnell Douglas Research Labs.
Attn: Dr. D.P. Ames
Dr. Charles Whitsett
St. Louis, Missouri 63166

Defense Documentation Center
Cameron Station Bldg. 5
Alexandria, Virginia 22314
Attn: TCA (14 copies)
Via: Naval Air Systems Command
Code AIR-954
Washington, D.C. 20361

The Franklin Institute Research
Laboratories
Twentieth & Parkway
Philadelphia, Pennsylvania 19103
Attn: Technical Director

Dr. John A. Schey
Department of Mechanical Engr.
University of Waterloo
Waterloo, Ontario
Canada N2L 3G1

Convair Division
General Dynamics
San Diego, California 92112
Attn: Mr. W. Sheck

Dr. Charles Gilmore
School of Engineering and
Applied Science
George Washington University
Washington, D.C. 2006

Army Aviation Systems Command
Attn: Mr. R. V. Vollmer (AMSAV-ERE)
P. O. Box 209
St. Louis, MO 63166

AIResearch Co.
Mat's Applications Group
93-361-503-4V
ATTN: Mr. R. G. Berryman
402 S. 36th St.
Phoenix, AZ 85010

ITT Research Institute
10 West 35th Street
Chicago, Illinois 60616
Attn: Dr. N. Parikh

Kawecki Berylco Industries
P.O. Box 1462
Reading, Pennsylvania 19603
Attn: Dr. J.P. Denny

Ladish Company
Packard Avenue
Cudahy, Wisconsin 53110
Attn: Mr. Robert Daykin

Linde Company
Division of Union Carbide
P.O. Box 44
Tonawanda, New York 14152

Lockheed Aircraft Corporation
Lockheed Missile Systems Division
P.O. Box 501 - Orgn. 80-72, Bldg. 18
Sunnyvale, California 91088
Attn: Dr. M.I. Jacobson
Dr. Frank Crossley

Lycoming Division
Avco Corporation
550 South Main Street
Stratford, Connecticut 06497
Attn: Division Library

Midwest Research Institute
425 Volker Boulevard
Kansas City, Missouri 64110

Northrop Corporation
3901 West Broadway
Hawthorne, California 90250
Attn: Mr. Allen Freedman
Dr. Govind Chanani

Solar Division
International Harvester Company
2200 Pacific Highway
San Diego, California 92112
Attn: Dr. A.G. Metcalfe

Wyman Gordon Co.
Attn: Mr. Charles Gura
Worcester Street
North Grafton, MA 05163

United Aircraft Research Laboratory
East Hartford, Connecticut 06108
Attn: Mr. Roy Fanti

Vought Aeronautics Division
LTV Aerospace Corporation
P.O. Box 5907
Dallas, Texas 75222
Attn: Mr. M. McLaren

Dr. Paul Lowenstein
Nuclear Metals, Inc.
2229 Main Street
Concord, Massachusetts 01742

General Electric
Missile & Space Division
Materials Science Section
P.O. Box 8555
Philadelphia, Pennsylvania 19101
Attn: Technical Library

Reynolds Metals Company
Reynold Metals Building
Richmond, Virginia 23218
Attn: Technical Library

Artech Corporation
2816 Fallfax Drive
Falls Church, Virginia 22042
Attn: Mr. Henry Hahn

General Electric Research Laboratory
Schenectady, New York 12301
Attn: Dr. Don Wood

Mr. A. E. Hohman, Jr.
Supervisor, Engineering Materials
Vought Systems Division
LTV Aerospace Corp
P. O. Box 5907
Dallas, TX 75222

Dr. D. H. Peterson
Senior Scientist
Advanced Technology Center, Inc.
P. O. Box 6144
Dallas, TX 75222

Dr. Gary Geschwind
Plant 26 (Research Dept.)
Grumman Aerospace Corporation
Bethpage, NY 11714

Mr. Carl Micillo
Grumman Aerospace Company
Adv. Mat. & Proc. Division
Bethpage, NY 11714

Aluminum Company of America
1200 Ring Bldg.
Washington, D.C. 20036
Attn: Mr. G.B. Barthold

Pratt & Whitney Aircraft Corp.
400 Main Street
East Hartford, Connecticut 06108
ATTN: Mr. George Rogers
Dr. Alan Lawley
Department of Metallurgical
Engineering
Drexel University
32nd & Chestnut Streets
Philadelphia, Pennsylvania 19104

Dr. Howard Bomberger
Reactive Metals, Inc.
Niles, Ohio 44446

Massachusetts Institute of Technology
Department of Metallurgy and Material
Science
Cambridge, Massachusetts 02139
Attn: Dr. N.J. Grant

Mr. Gary Keller
D/115-000, SB04
Rockwell International
Los Angeles International Airport
Los Angeles, CA 90009

Lockheed Aircraft
Attn: Mr. Rod Siemenz
Dept. 74-50, Bldg 85
Burbank, CA 91520

Douglas Aircraft Company
3855 Lakewood Boulevard
Long Beach, CA 90846

Defense Advanced Research Project
Agency
1400 Wilson Boulevard
Arlington, Virginia 22209
Attn: Dr. E.C. VanReuth

Dr. Neil Paton
Rockwell International Corp.
Science Center
P.O. Box 1085
1049 Camino Dos Rios
Thousand Oaks, CA 91360.

Pratt & Whitney Aircraft
Division of United Aircraft Corp.
Florida Research & Development Center
P.O. Box 2691
West Palm Beach, FL 33402
Attn: Mr. John Miller

McDonnell Aircraft Co.
St. Louis, Missouri 63166
Attn: Mr. H.C. Turner

Dr. J.C. Williams
Department of Metallurgy and
Materials Science
Carnegie-Mellon University
Pittsburgh, Pennsylvania 15213

Westinghouse Electric Corporation
Central Research Laboratories
Attn: Dr. Alan T. Male
Manager, Material Processing Research
Beulah Road, Churchill Borough
Pittsburgh, PA 15235

Crucible Materials Research Center
P. O. Box 88
Parkway West and Route 60
Pittsburgh, PA 15230
- ATTN: Mr. E. J. Dulis

Lockheed Missiles & Space Company,
Inc.
Palo Alto Research Laboratory
3251 Hanover Street
Palo Alto, California 94304
Attn: Dr. Thomas E. Tietz
52-31/204

Titanium Metals Corporation of
America
Henderson, Nevada 89015
Attn: Mr. James Hall

Grumman Aerospace Corporation
Bethpage, L.I., New York 11714
Attn: Mr. R. Heitzmann (2 copies)

Mr. George Hsu
Manager of Industry Standards
Reynolds Metals Corp.
6601 W. Broad Street
Richmond, Virginia 23261

Dr. John K. Tien
Henry Krumb School of Mines
Columbia University
New York, New York 10027

Boeing Vertol Company
Boeing Center
P.O. Box 16858
Philadelphia, Pennsylvania 19142